



HAL
open science

Aerodynamic design of long endurance convertible UAV

Yuchen Leng

► **To cite this version:**

Yuchen Leng. Aerodynamic design of long endurance convertible UAV. Fluid Dynamics [physics.flu-dyn]. Institut Supérieur de l'Aéronautique et de l'Espace (ISAE), 2020. English. NNT: . tel-04669716

HAL Id: tel-04669716

<https://enac.hal.science/tel-04669716v1>

Submitted on 9 Aug 2024

HAL is a multi-disciplinary open access archive for the deposit and dissemination of scientific research documents, whether they are published or not. The documents may come from teaching and research institutions in France or abroad, or from public or private research centers.

L'archive ouverte pluridisciplinaire **HAL**, est destinée au dépôt et à la diffusion de documents scientifiques de niveau recherche, publiés ou non, émanant des établissements d'enseignement et de recherche français ou étrangers, des laboratoires publics ou privés.



THÈSE

En vue de l'obtention du

DOCTORAT DE L'UNIVERSITÉ DE TOULOUSE

Délivré par :

Institut Supérieur de l'Aéronautique et de l'Espace

Présentée et soutenue par :

Yuchen LENG

le jeudi 17 décembre 2020

Titre :

Aerodynamic design of long endurance convertible UAV
Conception aérodynamique de drones convertibles de longue endurance

École doctorale et discipline ou spécialité :

ED MEGeP : Dynamique des fluides

Unité de recherche :

Équipe d'accueil ISAE-ONERA EDyF

Directeur(s) de Thèse :

Jean-Marc MOSCHETTA (directeur de thèse)

Murat BRONZ (co-directeur de thèse)

Jury :

M. Thomas LEWEKE Professeur Université Aix Marseille - Président

M. George BARAKOS Professeur Université de Glasgow - Rapporteur

M. Murat BRONZ Professeur ENAC - Co-directeur de thèse

Mme Okşan ÇETİNER YILDIRIM Professeure Université Technique d'Istanbul ITU- Examinatrice

M. Thierry JARDIN Ingénieur de recherche ISAE-SUPAERO – Examineur

M. Jean-Marc MOSCHETTA Professeur ISAE-SUPAERO - Directeur de thèse

Acknowledgements

The work of this PhD thesis would not be possible without help and support from some of the most wonderful people I had the honor to work with. I would like to firstly thank my advisors, Prof. Jean-Marc Moschetta, Murat Bronz and Thierry Jardin. It is thanks to you that I started this journey, and the questions and contributions from your expertise have guided me constantly through the past three years.

I would also thank the development team at Delair, for financing this research, and for letting me into the professional development environment. I thank particularly Stéphane Terrenoire, Alexandre Lapadu, Clément Pffifer and Christophe Chanudet, for many discussions about our project development that make their way into the results in this work.

I'm also indebted to my two hosting laboratories : ISAE-DAEP and ENAC Paparazzi team. Specifically to Rémy Chanton, Henri Dedieu, Sylvain Belliot, Michel Gorraz, Xavier Paris for their efforts in assisting me completing three highly fruitful windtunnel campaign ; to Laurent Joly for his constant encouragement for a young researcher ; to Yannick Jestin for his management of Paparazzi team and most serious greetings ; and to my colleagues who has brought different aspects of life into the three-year journey.

To the students that I have worked with, either through student projects or through brief meeting in class. The collaboration with Karim Favez on convertible aircraft optimisation has been an indispensable part of this project.

Finally, I cannot forget my friends and family, near or far, their kindness and support that allow me to achieve what would otherwise be impossible.

Contents

Abbreviations	xiii
Resume des Chapitres	1
1 Introduction	7
1.1 Background	7
1.2 Objectives	8
1.3 Structure	9
2 Long Endurance Convertible UAV	11
2.1 Introduction	11
2.2 Unmanned Aerial Vehicle	11
2.3 Vertical Take Off and Landing (VTOL) aircraft	13
2.4 Long endurance VTOL flight	16
3 Propeller Aerodynamics in Transition Flight	19
3.1 Introduction	20
3.2 Theoretical Analysis and Analytic Model Derivations	23
3.3 Experimental Studies	38
3.4 Results and discussions	46
3.5 Conclusions	51
4 Experimental Study on Propeller-Wing Aerodynamic Interactions	53
4.1 Introduction	54
4.2 Propeller wake development	55
4.3 Aerodynamic augmentation of closely-coupled propeller	74

4.4	Experiment Set-Up	76
4.5	Decomposition of Thrust-Augmented Aerodynamic Loads	81
4.6	Results and Discussions	86
4.7	Conclusion	93
5	Propeller-Wing Aerodynamic Interaction Model	97
5.1	Numerical Formulation	97
5.2	Comparison with experimental results	102
5.3	Conclusion	105
6	Mission-based Long Endurance Convertible UAV Design	107
6.1	Introduction	107
6.2	Development of Optimization Tool and Disciplines	112
6.3	Optimization Problem	120
7	Conclusion and perspectives	133
7.1	Main achievements	133
7.2	Future work	134
A	Static Mass Error	137
B	NACA Propeller Geometry	139
C	NACA Proprotor Test Data	141
D	Wake Surveys with Flap	143
E	Relation between Propeller and Slipstream Parameters	147
F	Useful Integrations	149
F.1	$\int_{z_1}^{z_2} \frac{ds}{s(\sqrt{1+s^2}-s)}$	149

F.2	$\int_{z_1}^{z_2} \frac{\sqrt{1+s^2}-s}{a\sqrt{1+s^2}-(a-1)s} ds$	150
F.3	$\int_{z_1}^{z_2} \frac{ds}{s[a\sqrt{1+s^2}-(a-1)s]}$	151
G	Optimal Aircraft Designs	153
G.1	Hybrid Airplane	153
G.2	Quadcopter	162
	Bibliography	171

List of Figures

2.1	DJI Phantom 4 quadcopter	12
2.2	Military Applications of UAVs	12
2.3	Bell 206 Helicopter	13
2.4	Tilt-Rotor Aircraft	14
2.5	Tilt-Wing Aircraft	14
2.6	Convair XFY-1	15
2.7	Tail-Sitter UAVs	16
2.8	Illustration of Long Range VTOL Operation	17
3.1	Definition of aerodynamic angles in rotor and aircraft reference frames	21
3.2	Aerodynamic loads on a propeller at incidence	21
3.3	Blade section in axial flow	24
3.4	Flow directions of advancing and retreating blade sections	25
3.5	Comparison between a blade element solution of thrust variation and cosine approximation	28
3.6	3D Printed NACA propellers	35
3.7	C_N of a small-scale rotor versus α_p from theory in [Phi04] and from current theory	35
3.8	C_n of a small-scale rotor versus α_p from theory in [Phi04] and from current theory	36
3.9	Thrust and normal force coefficients of small-scale propeller for various μ	37
3.10	ISAE SaBRe Wind Tunnel	39
3.11	ISAE SaBRe Wind Tunnel Section Plan	40
3.12	Propeller Test-Bench inside the ISAE SaBRe Wind Tunnel	40
3.13	Balance and propeller coordinates	41

3.14	C_T comparison with [The+17]	44
3.15	C_Q comparison with [The+17]	44
3.16	C_N comparison with [The+17]	45
3.17	C_n comparison with [The+17]	45
3.18	C_p comparison with [The+17]	46
3.19	C_T of a small-scale rotor against incidence angle for various λ_∞	47
3.20	C_P of a small-scale rotor against incidence angle for various λ_∞	48
3.21	C_N of a small-scale rotor against incidence angle for various λ_∞	49
3.22	C_n of a small-scale rotor against incidence angle for various λ_∞	49
3.23	C_T of a small-scale rotor against incidence angle for various λ_∞	50
3.24	C_P of a small-scale rotor against incidence angle for various λ_∞	51
3.25	C_N of a small-scale rotor against incidence angle for various λ_∞	51
3.26	C_n of a small-scale rotor against incidence angle for various λ_∞	52
4.1	Test set-up in ENAC indoor flight arena	56
4.2	Flow angle measurement	57
4.3	Flow speed measurement	58
4.4	Motion control system and survey pattern	59
4.5	Velocity distribution at survey plane for symmetrical configuration at 8000rpm	60
4.6	Comparison of axial velocity distribution at different rotation speeds	61
4.7	Velocity distribution at survey plane for with 15° flap deflection at 8000rpm	62
4.8	Velocity distribution at survey plane for with -15° flap deflection at 8000rpm	63
4.9	Displaced propeller slipstream and connecting line vortex segments	64
4.10	Side view of an aerofoil section after up-going propeller blade	64
4.11	Imaginary propeller distributed vortex system	66
4.12	Geometry relations to determine slipstream centre	72

4.13	Velocity distribution at survey plane for symmetrical configuration at 8000rpm, with displaced slipstream boundary	73
4.14	Configuration Parameters	76
4.15	Installation of Wing on 2KPi Turntable	77
4.16	Isometric View of Sem-Span Model	77
4.17	Side and Top View of Wing Installation on 2KPi Turntable	79
4.18	Transition Corridor and Test Conditions for Tested Wing	81
4.19	Propeller Streamtube	82
4.20	Wing Geometry Definition	83
4.21	Lift coefficient for various configurations at $V_\infty = 5m/s$	87
4.22	Augmented Lift Coefficient at $\alpha = 10^\circ$ for various δ_f	88
4.23	Augmented Moment Coefficient at $\alpha = 10^\circ$ for various δ_f	88
4.24	Augmented Lift Coefficient at $\alpha = 40^\circ$ for various δ_f	89
4.25	Augmented Moment Coefficient at $\alpha = 40^\circ$ for various δ_f	90
4.26	Augmented Lift Coefficient at $\alpha = 10^\circ$ for various δ_i	90
4.27	Augmented Moment Coefficient at $\alpha = 10^\circ$ for various δ_i	91
4.28	Augmented Lift Coefficient at $\alpha = 40^\circ$ for various δ_i	91
4.29	Augmented Moment Coefficient at $\alpha = 40^\circ$ for various δ_i	92
4.30	Augmented Lift Coefficient at $\alpha = 10^\circ$ for various z_p	93
4.31	Augmented Moment Coefficient at $\alpha = 10^\circ$ for various z_p	93
4.32	Augmented Lift Coefficient at $\alpha = 40^\circ$ for various z_p	94
4.33	Augmented Moment Coefficient at $\alpha = 40^\circ$ for various z_p	94
5.1	Lifting surface panels	98
5.2	Horseshoe vortex	99
5.3	Blad tip vortices visualised from background-oriented schlieren (BOS) method	100
5.4	Wake Skew Angle	101

5.5	Non-linear Lifting Line Model for Propeller and Wing Configuration	103
5.6	Clean Configuration Lift and Pitch Moment Coefficient	104
5.7	Clean Configuration Drag Polar	105
5.8	Calculated <i>ALC</i> for various angles of attack	106
6.1	Multirotor Propulsion Group [Bic+20]	110
6.2	Main Flow chart of QOPTIMIZER program [BMH12]	111
6.3	ESC Constant Current vs Mass Model	114
6.4	Motor Max Current vs Mass Model	115
6.5	Motor Kv Rating vs Mass Model	115
6.6	Wing Spar Cross Sections	116
6.7	Wing spar under elliptical load distribution	116
6.8	Design Flow Chart for a Single Flight Phase	119
6.9	Studied VTOL aircraft configurations	122
6.10	Maximize single phase endurance XDSM	126
6.11	Power consumption by flight phase in scenario 1	130
6.12	Power consumption by flight phase in scenario 2	132
A.1	Definition of Balance Inclinations	137
D.1	-15° flap deflection	144
D.2	15° flap deflection	144
D.3	-15° flap deflection	145
D.4	15° flap deflection	145

List of Tables

3.1	Order of magnitude of CPU time per case for different numerical propeller models	38
3.2	E-prop Test Matrix	41
3.3	NACA Propellers Test Matrix	41
4.1	Slipstream Deformation Testing Conditions	58
4.2	Centreline displacement at various rotation speeds	73
4.3	Wing Specification	78
4.4	Testing Conditions	81
6.1	Design Parameters	112
6.2	Independent Variables	123
6.3	Design Parameters	124
6.4	Constraints	124
6.5	Mathematical notation for MDO problem data	125
6.6	Baseline mission specifications	127
6.7	Scenario 1 mission specifications	127
6.8	Scenario 2 mission specifications	128
6.9	Design parameters optimized for baseline mission and Tron F90+ specifications [Qua]	128
6.10	Design Parameters for scenario 1	129
6.11	Design parameters for scenario 2	131
B.1	NACA Propeller Geometry	139
C.1	NACA Proprotor Test Data	141
C.2	NACA Proprotor Test Data (continued)	141

Abbreviations

UAV	<i>Unmanned Aerial Vehicle</i>
UAS	<i>Unmanned Aerial System</i>
VTOL	<i>Vertical Take-Off and Landing</i>
ESC	<i>Electronic Speed Controller</i>
ALC	<i>Augmented Lift Coefficient</i>
ADC	<i>Augmented Drag Coefficient</i>
AMC	<i>Augmented Moment Coefficient</i>
MDO	<i>Multidisciplinary Design Optimisation</i>
CFD	<i>Computational Fluid Dynamics</i>
DC	<i>Direct Current</i>
SLSQP	<i>Sequential Least Squares Programming</i>
COBYLA	<i>Constrained Optimisation by Linear Approximation</i>
GA	<i>Genetic Algorithm</i>

Résumé des Chapitres

Introduction

Aujourd'hui les aéronefs sans pilote à bord (drones) sont utilisés dans de plus en plus de scénarios où les avions habités ont des difficultés d'accès ou sont moins efficace économiquement à cause des coûts de main d'oeuvre qui y sont liés. La croissance de l'utilisation des drones exige de nouveaux véhicules aériens plus automatisés. La technologie de l'avion à décollage et atterrissage vertical (VTOL, d'après Vertical Takeoff and Landing), ou avion convertible, aide à diminuer le besoin d'assistance d'humaine dans la phase de déploiement et de récupération.

Les véhicules à voilure tournante sont toujours adaptés aux missions qui exigent un avion convertible. Cependant, leur rendement en croisière est plus faible que celui des avions à voilure fixe. En conséquence, la configuration à voilure fixe est souvent combinée avec des hélices de sustentation, voire des dispositifs hypersustentateurs (volet soufflés) afin que les exigences du VTOL et d'une longue endurance soient satisfaits au même temps.

La conception aérodynamique de drone convertible introduit les nouveaux enjeux d'ingénierie car l'hélice et l'aile sont soumis à des effets inattendus lors de leur conception. Cette étude propose des modèles d'ordre réduit afin d'estimer les performances de l'hélice à l'incidence et l'interaction hélice-voilure. Trois campagnes d'essai ont été réalisées à la soufflerie de bas nombre de Reynolds dont les résultats ont été utilisés pour développer les modèles. Une méthodologie de conception d'aéronef est proposée en utilisant ces modèles d'ordre réduit.

Drone Convertible de Longue Endurance

La technologie de drone a mûri pendant les quatres dernières dizaines d'années. Cette technologie avait à l'origine pour objectif de remplacer l'humaine dans les missions militaires. Les avancements techniques sur la capacité des batteries et les moteurs électriques permettent un spectre étendu des applications de la livraison autonome à l'exploration des grottes. L'efficacité grâce à l'autonomie est un avantage important dont bénéficient les drones de longue endurance, mais l'assistance d'un équipage au sol pour le lancer ou la récupération de l'appareil à voilure fixe reste toujours une contrainte opérationnelle.

Plusieurs dispositifs hypersustentateurs sont expérimentés pour réaliser le décollage et l'atterrissage verticaux. L'hybridation du multicopter et de l'avion à voilure fixe est la solution technique la plus simple mais cela ajoute des groupes propulsifs supplémentaires qui augmentent la masse de l'appareil et réduisent donc les performances en vol. La configuration convertible comme le tiltrotor ou le tiltwing n'ajoutent aucun groupe propulsif supplémentaire, mais leur voilure et leurs hélices peuvent rencontrer des conditions extrêmes en terme d'angle

d'incidence pendant la phase de transition entre vol stationnaire et horizontal. L'incertitude des caractéristiques aérodynamiques mettent la performance et la contrôlabilité de ces types d'aéronefs en question.

Malgré les enjeux rencontrés en définissant un tel drone convertible, la gamme des missions accessibles peut être élargie en adoptant le décollage et l'atterrissage verticaux sans intervention humaine. La motivation d'étudier les phénomènes aérodynamiques dans la conception de drone convertible de longue endurance est bien évidente.

Hélice à Incidence

Pendant la phase de transition, les efforts aérodynamiques générés par la voilure sont faibles à cause de la très basse vitesse. Les forces et les moments aérodynamiques du véhicule proviennent principalement de l'hélice portante.

Pendant la montée ou la descente verticales, ainsi que le vol horizontal, la direction du vent à l'infini amont s'aligne générale dans l'axe du rotor. On peut supposer que l'écoulement autour de l'hélice est axisymétrique. Dans ce cas, seulement la traction et le couple dans l'axe de rotation se présentent sans aucune force latérale ni moment.

Cependant, quand le véhicule accélère ou décélère, une grande l'angle d'incidence α_p entre le vent à l'infini et l'axe de rotation peut exister. En conséquence, l'hypothèse que l'écoulement soit axisymétrique n'est plus valide, et les efforts exercés sur la pale d'hélice varient en fonction de l'angle azimutal pendant une révolution. L'effet net est la création d'une force normale N et un moment n dans le plan du disque d'hélice. De plus, une augmentation de la traction T et la puissance P est souvent rencontrée.

Dans le cadre de l'étude de l'hélice en incidence, un modèle d'ordre réduit a été développé pour estimer les quatre efforts aérodynamiques en fonction de la géométrie de l'hélice, du paramètre d'avancement μ (rapport entre la vitesse de vol et la vitesse de rotation) et de l'angle d'incidence α_p . Le modèle se base sur la performance de l'hélice dans l'écoulement axisymétrique qui est facile à estimer par une méthode expérimentale ou numérique. Ensuite, un système analytique d'équations obtenu de l'analyse d'élément pale calcule les efforts de l'hélice à incidence.

Une campagne d'essai a été réalisé à la soufflerie à bas nombre de Reynolds sur le site de l'ISAE-Supaéro. Le système de mesure a permis d'isoler les efforts d'hélice à haute fréquence (1000Hz). Pendant l'essai, l'incidence de l'hélice a changé de 0° à 180° grâce à un mât motorisé qui a supporté l'hélice. Plusieurs paramètres d'avancement sont testés sur cette hélice dont la géométrie est précisément connue. Les données expérimentales confirment que la précision du modèle analytique est suffisante pour prédire la performance de l'hélice à l'incidence entre 0° et 90° , mais la puissance peut-être sur-estimée dans les conditions extrêmes ($\mu > 0.08 \sim 0.11$).

Essai de l'Interaction Hélice-Voilure

Afin de modéliser les efforts aérodynamiques provenant de l'interaction hélice-voilure, deux campagnes d'essai ont été réalisées.

Le premier consistait un sondage de sillage en aval d'une aile soufflée par une hélice de traction. Cela nous a permis d'étudier l'interaction du sillage de l'hélice avec l'aile. Le champ de vitesse a été obtenu par une sonde à cinq trous montée sur un cadre avec des rails permettant un mouvement. Cette campagne d'essai consistait de deux parties, la première à la Volière Occitanie de l'ENAC pour étudier la condition du vol stationnaire et la deuxième partie s'est déroulée dans la soufflerie de basse vitesse à l'ENAC.

Le sillage de l'hélice en aval de l'aile, caractérisé par une zone d'écoulement à haute vitesse au rapport de son environnement, est apparu différent de celui d'une hélice seule. La partie supérieure du sillage se déplace dans la même direction que la vitesse latérale moyenne d'écoulement dans cette partie, et même sur la partie inférieure. Cela introduit une déformation du sillage loin de la forme cylindrique qui est souvent supposée dans les modèles d'interaction hélice-voilure. Ce phénomène peut s'expliquer par une modèle de la singularité en utilisant la méthode de réflexion.

Une deuxième campagne d'essai a été conçue pour mesurer indépendamment les efforts aérodynamiques d'une combinaison hélice-voilure similaire à celle testée pendant la première campagne. Cette campagne s'est concentrée sur trois paramètres de conception : le braquage de volet δ_f , l'angle d'installation δ_i de l'hélice et son décalage vertical z_p au niveau de l'aile. L'angle d'incidence α , la vitesse du vent V_∞ et la vitesse de rotation Ω de l'hélice ont été contrôlés pour simuler la condition de vol de transition. Cet essai a eu lieu dans la soufflerie à bas nombre de Reynolds à l'ISAE-Supaéro.

Les résultats sont adimensionnés en prenant en compte la condition atmosphérique ainsi que la traction de l'hélice (défini par un coefficient d'énergie de sillage). Les résultats ont révélé une augmentation significative de la portance d'une voilure. L'effet dépend de l'angle d'incidence. À l'incidence faible, la composante de portance induite par la circulation semble être constante pour un coefficient d'énergie de sillage élevé, alors que cette composante devient variable à un angle d'attaque plus élevé. Un angle d'installation de l'hélice négatif ou des positions d'hélice plus élevées ont tendance à augmenter légèrement cet effet d'augmentation, bien que déplacer trop haut l'hélice ($\approx 0.2D_p$) risque de faire sortir la voilure du sillage de l'hélice.

Une augmentation du moment de tangage a également été observée. À faible angle d'attaque, l'effet de sillage de l'hélice amplifie uniquement le moment de tangage à portance nulle par la traction. À un angle d'attaque plus élevé, il existe un coefficient d'énergie de sillage critique au-dessous duquel le sillage de l'hélice ne peut plus augmenter le moment de tangage des ailes. L'angle d'installation de l'hélice et la position verticale ne semblent pas avoir une influence significative sur le moment de pas des ailes parmi les cas de test, bien que le décalage de la ligne de la traction de l'hélice puisse créer un moment de tangage

supplémentaire.

Modélisation de l'interaction Hélice-Voilure

Un modèle de lignes portantes numérique a été développé sur la base de la bibliothèque MachUp pour prédire les efforts aérodynamiques de la combinaison hélice-voilure. Le modèle original a été formulé comme un système linéaire d'équations pour les tourbillons attachés. Cependant, le modèle a dû être généralisé afin d'être utilisé pour les conditions de vol de transition. L'angle d'incidence élevée invalide les hypothèses d'un sillage d'hélice droit, de l'aérodynamique linéaire du profil et d'un système linéaire de tourbillons en fer à cheval.

Pour estimer la déformation du sillage, la méthode de Froude a été appliquée à l'axe du sillage. Les points immergés de l'aile ont été identifiés en conséquence selon l'axe dévié. Les performances de l'hélice ont également été corrigées par le modèle de l'hélice à l'incidence élevée développée dans le chapitre 3.

Les coefficients aérodynamiques C_L , C_D et C_m d'un profil 2D peuvent être interpolés des données expérimentales à forte incidence. La limitation majeure de cette méthode est sa dépendance à la disponibilité des données expérimentales du profil choisi. Une autre méthode pourrait être une transition vers des formules empiriques de plaque plane.

Le système d'équation pour les tourbillons attachés a été pris de sa forme d'origine non-linéaire et une méthode de Newton-Raphson a été utilisée pour résoudre le système.

Le modèle aérodynamique révisé a été validé avec les données de configuration lisse et s'est révélé tout aussi robuste et légèrement plus précis au rapport de la version originale.

Lorsque le sillage de l'hélice a été inclus, il a été observé que la vitesse tangentielle pouvait créer une instabilité numérique, et un facteur de réduction de la vitesse tangentielle doit être appliqué, et a été fixé à $\epsilon_t = 0,075$. Il a été déterminé qu'il s'agissait probablement d'une combinaison de la déformation du sillage observée dans le chapitre 4 et du profil de la vitesse tangentielle dans le sillage. Le modèle s'est avéré être en accord avec les données expérimentales à l'incidence inférieure à 10° ou au-dessus de l'incidence de décrochage à 20° à un coefficient d'énergie de sillage modéré.

Optimisation de Drone Convertible de Longue Endurance

Basé sur les modèles aérodynamiques développés, une évaluation rigoureuse des différentes configurations de drones convertibles sur différents cahiers de charge est effectuée. Contrairement à la conception d'aéronefs à grande échelle, la configuration aérodynamique des UAV est très diversifiée et, par conséquent, une manière claire d'adapter la configuration de l'aéronef selon le cahier de charge est souhaitée au vu des études antérieures. Pour résoudre ce problème, un outil d'optimisation multidisciplinaire est développé à partir de la bibliothèque

OpenMDAO pour aider la conception aérodynamique préliminaire d'un drone convertible.

La méthodologie finale permet de optimiser plusieurs configurations de drones convertibles et de les comparer ensuite en termes de la consommation énergétique pour différentes phases de vol. L'outil effectue une série de boucles d'optimisation en tenant compte de paramètres importants tels que les surfaces alaires et les éléments de propulsion pour dimensionner la configuration la plus efficace. Il s'agit de permettre une comparaison objective et quantifiable entre les configurations.

Une comparaison entre la configuration d'un quadcoptère et d'un avion hybride a été réalisée en utilisant la méthodologie proposée. Il a été démontré qu'il était possible d'adapter les paramètres de conception des aéronefs au profil de mission spécifié et il a été révélé que différentes stratégies doivent être adoptées pour optimiser la configuration des différents véhicules.

Conclusions

Les travaux présentés ont démontré une vision moderne de l'exploitation de la conception aérodynamique des drones convertibles à échelle réduite propulsé par un système électrique. L'étude examine les progrès techniques des techniques de modélisation aérodynamique nécessaires pour évaluer les performances de vol dans le contexte de la conception préliminaire. Il a également envisagé comment ces outils pourraient être assemblés pour évaluer l'impact des choix de conception selon le cahier de charge. L'étude cadre bien avec les recherches sur d'autres fronts technologiques du vol électrique VTOL et devrait travailler de concert avec d'autres avancées, telles que celles dans les domaines de l'aéro-structure, du contrôle de vol, pour faciliter la conception du futur véhicule de vol autonome à longue endurance.

La recherche actuelle a réussi à identifier le besoin de modèles aérodynamiques précis et efficaces en termes de temps de calcul dans la phase de conception préliminaire. Des progrès importants ont été réalisés pour répondre à ces besoins. Cependant, au cours du processus de développement, plusieurs modifications importantes ont été découvertes pour être bénéfiques pour d'autres améliorations. Ils n'ont pas pu être intégrés aux travaux en cours en raison de contraintes technologiques ou de temps.

Le modèle actuel de déformation de sillage n'est applicable que pour une aile de profil symétrique placée le long de l'axe de sillage. Un développement futur pourrait généraliser la théorie pour permettre un déplacement et un profil cambré.

La stabilité numérique du modèle de lignes portantes peut être encore améliorée par une meilleure modélisation de la vitesse induite du sillage. Une hypothèse différente du profil de vitesse tangentielle devrait améliorer la robustesse de la solution.

La performance de la méthode d'optimisation peut être améliorée en utilisant le calcul parallèle et, par conséquent, davantage de paramètres de conception peuvent être pris en compte sur la même durée. Les modèles de structure et de contrôle de vol pourraient être

plus précis pour augmenter le niveau de confiance de la solution optimisée.

Introduction

1.1 Background

It is not an easy task to break free from gravity. Since the first manned powered flight by Wright brothers in 1903, new aircraft designs have always included the study of launch and recovery requirements. Take-off and landing are the phases where aircraft transit between ground and air, during which the suspension forces switch between ground support and aerodynamic lift.

The creation of aerodynamic lift requires the lifting surfaces to displace relative to surrounding air. Sufficient lift is typically obtained by either accelerating the entire vehicle to high speed or by fast movements of lifting surfaces.

The first method is widely used by fixed-wing aircraft such as airliners. The distance required for successful take-off is strongly related to the minimum airspeed required and the attainable acceleration. They are determined by a number of variables but principally involve wing and airfoil design, as well as thrust-to-weight ratio. A balanced configuration considering also cruise performance results in a noticeable runway length. The use of high-lift devices such as flaps and slats reduces take-off distance, and in special conditions, it can be further reduced by a catapult system which is used when highly constrained by space such as on an aircraft carrier or the field launch of an unmanned aerial vehicle.

The idea of rotating wing inspires another type of flying vehicle mostly represented by helicopters. The helicopter uses a main lifting rotor that rotates at high speed to generate sufficient lift while the vehicle velocity has little influence. This allows the aircraft to take-off and land vertically, hence reduce field requirement to minimum. The flapping wings of birds or insects have similar effects, but from a back-and-forth motion. For helicopters, minimum airspeed doesn't physically exist but their maximum airspeed is usually constrained by the drag increase from advancing-retreating-blade effect. Furthermore, the power consumption from blade rotation is usually higher than a comparable fixed-wing aircraft.

Besides sufficient lift generation, robust flight control is another key to enable low-speed flight. Intrinsicly, low airspeed over flight control surfaces reduces their efficiency in moment generation. Since the amount of moment generated from control surface deflection is proportional to dynamic pressure, the maximum achievable moment diminishes with the square of airspeed. Furthermore, as Reynolds number decreases, the risk of flow separation at

large deflection angle increases, and thus the useful travel of control surface is smaller, which further limits moment generation. Two strategies are commonly used in unmanned aerial vehicle to ensure sufficient control authority. First method utilises high-speed flow downstream of propeller to augment local flow speed at existing control surfaces. The second method uses multiple propellers for attitude control. For convertible vehicle, the first method calls for more integrated design since the architecture of control devices remains largely the same in the entire flight phase, while the second method involves control law switching between vertical and horizontal flight regimes.

The aforementioned challenges and various viable solutions to address those issues give birth to different aircraft configurations over a broad spectrum. The differences in design choices reflect the disparities of their operating scenario, or performance requirements from respective mission types. Current battery technology allows for pack energy density up to $250Wh/kg$, which would generally allow 20 minutes flight of a quadcopter while carrying a viable amount of payload. For longer endurance flight, the battery package would be too heavy if power consumption is kept at hover level. Typically a large portion of such flight profile contains a long distance segment at relatively high speed. Operating a fixed-wing type aircraft in this scenario could potentially reduce power consumption by a fifth, and thus such transition between VTOL and cruise phase could extend significantly the endurance capability of convertible UAVs.

This research was an attempt to a broad study of available technologies in aerodynamic engineering specific or beneficial to long endurance convertible UAV design and a synthesis of design methodology dedicated to such type of aircraft.

1.2 Objectives

The research was divided into two principle parts. The first part contains an analysis and modelling of propeller and lifting surface aerodynamic loads in unusual flight conditions encountered in VTOL operations. The second part continues on a methodology study aimed at convertible UAV design based on more detailed findings on vehicle aerodynamic characteristics in the first part.

The aerodynamic study concentrated first on asymmetric propeller load measurements and modelling. The work is presented in chapter 2, and has compared various theories based on their accuracies and computational costs. The work was validated against a dedicated windtunnel test campaign, which allowed fine tuning of eventual method. This work is followed closely by a study on propeller-wing aerodynamic interactions, which put focus on the lift and moment augmentation effects of a propeller wake over a wing. The aerodynamic study concludes with validated reduced-order models for forces and moments at hover and transition flight condition.

The methodology study was conducted on the basis of developed reduced-order models. The objective was to construct the optimisation loops for different convertible UAV design

based on mission profile and analyse the solution algorithm. Finally it concludes with impacts of aerodynamic characteristics over the design space.

1.3 Structure

The manuscript is organized to follow a logical path to address the issue of convertible long endurance UAV design. Chapter 2 presents past studies and state-of-art on VTOL aircraft research, where major challenges in vehicle aerodynamics were concluded. Chapter 3, 4 and 5 introduce studies on propeller and wing aerodynamics modelling in order to provide rapid analysis model with sufficient accuracy for preliminary design. Chapter 6 presents a possible optimization architecture for prototyping such aircraft. The presented method is able to generate optimal sizing for given aircraft configuration and mission profile. Sensibility studies on principle design parameters and important conclusions were also introduced.

Long Endurance Convertible UAV

Contents

2.1	Introduction	11
2.2	Unmanned Aerial Vehicle	11
2.3	Vertical Take Off and Landing (VTOL) aircraft	13
2.4	Long endurance VTOL flight	16

2.1 Introduction

This chapter explores the concept of long endurance convertible UAV. The features, development and notable examples of an unmanned aerial vehicle (UAV) is introduced first. These are followed by an introduction of technologies that enable vertical take-off and landing capability. The chapter concludes with possible applications of long endurance convertible UAV.

2.2 Unmanned Aerial Vehicle

Unmanned aerial vehicle is an aircraft that is either remotely controlled or autonomously piloted. Generally, the UAV category contains a vast collection of aircraft configurations. Some of them have counterpart in manned aviation, while some others, such as the quadcopter, are seldom seen until its wide adoption in UAV applications.

The reason of different configurations chosen for unmanned system development is worth noting. The emergence of unmanned aircraft vehicle is driven by missions that are either less efficient or inaccessible with a human pilot. Thus, taking the flight crew outside of design constraints changes the philosophy of how the aircraft is adapted to the mission profile. For example, quadcopters in Fig. 2.1 are widely used as micro UAVs instead of scaled down helicopters. Removing the pilot often lowers the payload and dimension of the aircraft, and at smaller dimensions, the mechanism and control strategy of a quadcopter design is usually simpler than that of helicopters to achieve similar flight stability. On the other hand, efficient power system that can be integrated in a full-scale quadcopter hasn't become possible until the



Figure 2.1: DJI Phantom 4 quadcopter

last decade. Similarly, other mission requirements call for various adaptations and innovations in UAV design.

Within the last four decades, the world has witnessed a rapid expansion of UAV deployment in various kinds of missions, with the goal to replace human in high workload, high fatigue or high risk missions. One of its first successful applications is in military combat and surveillance where all criteria are satisfied. A long-range missions can be carried out by UAVs such as Global Hawk shown in Fig. ??, while small hand-deployed drone (RQ-11, Fig. ??) are used for on-site short-range operations.



(a) Northrop Grumman RQ-4 Global Hawk



(b) AeroVironment RQ-11 Raven

Figure 2.2: Military Applications of UAVs

As UAV technologies mature, the capability of developing autonomous system was no longer restricted to military units. UAVs start to play an increasingly important role in industrial applications. Land survey, aerial photogrammetry and search & rescue operations see some of the largest growth in UAV applications, as the benefit of safety, cost and time savings becomes more apparent.

It is thus not a surprise that behind the concept of UAV exist aircraft configurations that

hardly have anything in common, and as new applications like autonomous delivery become more common, new designs of UAV are bound to appear. However, it is a formidable task to draw fair and valid conclusions from comparisons of all possible concepts, therefore it is necessary to draw some boundaries. To limit the scope of the current research within the most concerned applications, only heavier-than-air aircraft are considered. The propulsion system is assumed to be fully electrical and propulsive power is delivered through rotating propeller.

2.3 Vertical Take Off and Landing (VTOL) aircraft

A VTOL aircraft is a heavier-than-air aircraft that can sustain level, climb and descent flight without establishing a forward speed. By definition, helicopters as shown in Fig. 2.3 are examples of VTOL aircraft. The main rotor acts as lift generator to sustain the weight of aircraft through high speed rotation relative to ambient air. Blade pitch angle can be adjusted by the swash plate mechanism : collective pitch change alters rotor lift ; periodic pitch change helps to rotate rotor plane to provide control force and moment. Thanks to its agility to perform precise flight manoeuvres at low speed, helicopters are widely used in missions such as search and rescue, where take off and landing field conditions are restricted. Complexity in manufacture and maintenance of main rotor mechanism as well as its power consumption poses restrictive acquire and operational costs.



Figure 2.3: Bell 206 Helicopter

Amongst mini and micro drone applications, the quadcopter is one of the widely adopted VTOL configuration. As the name suggests, a quadcopter has four propellers installed in the same plane. These propellers are usually fixed-pitch and thus can be manufactured easily in a smaller scale. Flight control signals are distributed among speed controllers for each propeller which varies rotational speed individually to achieve desired lift and control moments. The affordability of electrical components and the simple design makes quadcopter a popular design for micro UAV solutions, but the installation of four fixed-pitch propellers limits horizontal flight speed and their power consumption is a major constrain for endurance.

Some VTOL concepts sought to adapt different aircraft configurations based on flight phases. Tilt-rotor aircraft is a typical example, where the lifting rotor used for hover flight can pivot about 90 degrees to provide thrust for horizontal flight. Another major distinction



(a) V-22 Osprey in Transition Flight



(b) Quantum Systems Tron

Figure 2.4: Tilt-Rotor Aircraft

from the previous rotor-based concepts is the utilisation of lifting surfaces. The aircraft "transforms" itself from a rotorcraft to an airplane as airspeed increases, and lift generation transfers from propellers powered lift to wing generated lift. As the latter is greatly more efficient, cruise power consumption can be reduced significantly hence longer endurance. This concept has been adapted by large aircraft like the V-22 'Osprey' (Fig. ??) as well as micro UAV like Quantum (Fig. ??). Major difficulties are often found in achieving robust flight control between hover and cruise. Wing lift can only be reliably leveraged below critical angle of attack, which is typically between 10° and 20° . Such an angle would be too shallow for the vertical thrust component to sustain the vehicle while providing sufficient safety margin. Thus the propeller tilt must be carefully scheduled as a function of wing angle of attack, which creates additional requirements on external perturbations.



(a) Canadair CL-84



(b) NASA GL-10

Figure 2.5: Tilt-Wing Aircraft

An alteration of the tilt-rotor design is the tilt-wing aircraft, where instead of individual propellers, the whole wing pivots around its lateral axis. This brings two advantages : firstly, certain sections of the wing can be immersed in propeller high speed wake and thus maintain their aerodynamic loading capability in order to facilitate lift augmentation and/or flight

control ; secondly, the pivot mechanism is centralised in the fuselage thus reducing the number of moving parts. On the other hand, the degree of freedom in propeller angle relative to the wing is lost. Tilt-wing configuration has been realised in various technology demonstrators such as the CL-84 and GL-10 (Fig. 2.5)



Figure 2.6: Convair XFY-1

The last VTOL configuration discussed here is the tail-sitter aircraft. As the name suggests, a tail-sitter sits on the rear end of its fuselage so that the propeller could provide vertical lift. Once airborne, the aircraft changes its attitude towards horizontal flight. The concept has been studied in various demonstrators such as the Convair XFY-1 (Fig. 2.6) program in the 1954 as a manned VTOL aircraft. The difficulty for human pilot to maintain precise control while experiencing such drastic attitude change limited the development of such concept.

Its major advantage is the simplicity in aircraft structures as no moving parts are required for the transition flight. Considering limitations on human pilot are removed, this configuration has attracted interests in UAV applications. MAVION and Cyclone as shown in Fig. 2.7 are two past research projects based on tail-sitter aircraft.

The five VTOL aircraft concepts discussed are not a comprehensive list of all possible configurations to achieve vertical take-off and landing capability, however they represent the most accessible and reliable technologies in the design of such vehicle, and thus were chosen to be the focus of current research.

There isn't an 'ultimate' solution in choosing a VTOL aircraft configuration. The analysis above has illustrated that these five concepts have their individual features, advantages and disadvantages. Therefore, each configuration is suitable to perform a different set of missions. The current study attempts to answer the question on how mission profiles influences the design choices of a fully electrical unmanned VTOL aircraft.



(a) ENAC Cyclone [Bro+17]



(b) ISAE MAVION [LDM14]

Figure 2.7: Tail-Sitter UAVs

2.4 Long endurance VTOL flight

Analysis on current applications of UAVs in section 2.2 has revealed that UAVs help to replace human pilot in high workload or high risk missions. It is thus expected the autonomous level of unmanned aerial system (UAS) to continue increase. Advances in electronics and flight control / guidance (FCG) software has been the major drivers of the highly intelligent UAS deployed today. The availability of open-source autopilot such as Pixhawk or Paparazzi helps to integrate more onboard sensors and to provide more accurate trajectory generation and guidance. Long endurance missions with multiple waypoints or inspection missions required at precise locations become easy to plan and execute.

On the other hand UAV launch and recovery methods have remained relatively unchanged. Fixed-wing UAV cannot take-off and land at zero airspeed. Small scale UAVs are typically launched by hand, while larger ones may require a cleared field to serve as a runway. Catapult system is sometimes used to reduce the required field length. Thus, additional human intervention is needed to either directly launch the aircraft or assist in preparation. This creates extra operations and efforts at the launch-site and furthermore, remote stop-over would not be possible.

The need to sustain a minimal airspeed also means that the aircraft would be less manoeuvrable compared to helicopters or quadcopters. Fixed-wing UAVs are usually flown in empty open fields instead of constrained environment.

The application of VTOL UAV in these scenarios is a viable solution. Once power supply is established, the aircraft can take-off and land on itself without external assistance. Thanks to its ability to hover, the launch and recovery can take place in relatively constrained environment as well as certain parts in the flight mission. Quadcopters are already widely used



Figure 2.8: Illustration of Long Range VTOL Operation

in inspection or urban surveillance missions, which tend to be of short endurance around the station of deployment. This research envisioned the concept of long-endurance convertible UAV to explore the possibility of autonomous flight towards remote locations as demonstrated in Fig. 2.8, and strived to provide the necessary tools and methodology in achieving an aerodynamic concept according to envisioned deployment.

Propeller Aerodynamics in Transition Flight

Contents

3.1	Introduction	20
3.1.1	Background	20
3.1.2	Literature review	22
3.2	Theoretical Analysis and Analytic Model Derivations	23
3.2.1	Blade element analysis	23
3.2.2	Thrust and power model	26
3.2.3	Off-axis loads model	30
3.2.4	Model implementation	33
3.2.5	Comparisons with Classical Theories	34
3.3	Experimental Studies	38
3.3.1	Test Setup	39
3.3.2	SaBRe Windtunnel	39
3.3.3	Data Process	42
3.4	Results and discussions	46
3.4.1	Validation of the analytical model for thrust and power	46
3.4.2	Validation of analytical model for off-axis efforts	48
3.4.3	Backflow condition	49
3.5	Conclusions	51

Author's Contributions

Published Papers

Y. Leng, J.-Marc Moschetta, T. Jardin, M. Bronz, "An Analytical Model for Propeller Efforts at High Incidence", *3AF Conference on Applied Aerodynamics*, Paris, France, Mar.25-27, 2019.

Y. Leng, T. Jardin, M. Bronz, J.-Marc Moschetta, "Experimental Analysis of Propeller Forces and Moments at High Angle of Incidence", AIAA Paper 2019-1331, *AIAA Applied Aerodynamics Conference, AIAA SciTech Forum*, San Diego, United States, Jan. 7-11, 2019.

Y. Leng, H. Yoo, T. Jardin, M. Bronz, J.-Marc Moschetta, "Aerodynamic Modelling of Propeller Forces and Moments at High Angle of Incidence", AIAA Paper 2019-1332, *AIAA Applied Aerodynamics Conference, AIAA SciTech Forum*, San Diego, United States, Jan. 7-11, 2019.

Publications in progress

Y. Leng, T. Jardin, M. Bronz, J.-M. Moschetta, "Development of an Analytic Model of Proprotor Forces and Moments at High Incidence", *Journal of American Helicopter Society*

3.1 Introduction

3.1.1 Background

Advances in new electric propulsion technologies renewed interests in the prospect of vertical take-off and landing (VTOL) aircraft. According to [Vto], over 200 electric VTOL (eVTOL) manned or unmanned concepts are currently under development. A majority of them uses one or multiple rotors for both lift generation and flight control during VTOL operations.

To fully extract the advantage of eVTOL aircraft, a robust autonomous flight control system is used to manage the transition flight phase between hover and horizontal cruise. Its implementation requires good understanding and precise modelling of the external forces and moments on aircraft. At low airspeed, aerodynamic forces and moments from the proprotor constitute the main part of the vehicle loads.

In pure vertical ascent/descent as well as horizontal cruise, freestream velocity is closely aligned with rotor axis. In these situations, flow condition around the rotor could be treated as axisymmetric. Thanks to this assumption, only thrust force and rotor torque are generated along the rotor axis, no lateral force or moment model is required.

For the transition flight phase, the rapid change of trajectory causes a large difference between freestream direction and rotor axis, which is characterised as rotor incidence angle α_p in Fig. 3.1. For rotor modelling concerns, α_p should be considered independent from aircraft aerodynamic angles. In the aircraft reference frame, aerodynamic angles include angle of attack α_{ac} and side-slip angle β_{ac} : angle of attack α_{ac} is measured from the freestream component in the aircraft symmetric plane to its longitudinal axis; side-slip angle β_{ac} is

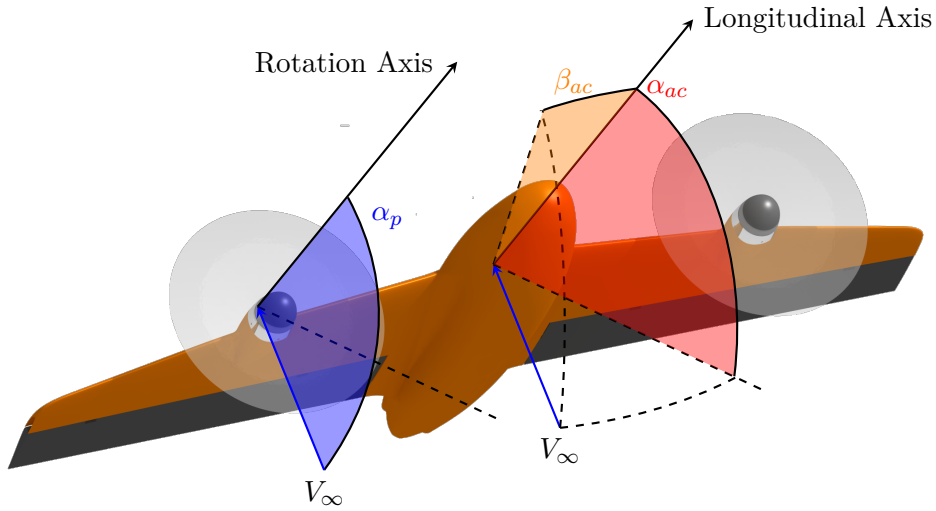


Figure 3.1: Definition of aerodynamic angles in rotor and aircraft reference frames

measured from the freestream component in the aircraft lateral plane to its longitudinal axis. To determine rotor performance, only one aerodynamic angle is required, the rotor incidence angle is defined as the angle between freestream direction and rotor axis. For full aircraft analysis, it is possible to convert α_{ac} and β_{ac} to α_p for each propeller considering its individual orientation respective to the aircraft longitudinal axis. Such conversion is usually trivial and won't be discussed in the current study.

In axial flow condition, α_p is zero and increases to $\pi/2$ for edgewise flow. For non-zero incidence angles, a rotor coordinate system is defined in Fig. 3.2. Freestream V_∞ is projected into two components: V_A along rotation axis and V_Z in rotor disk plane. The rotor coordinate takes the rotor centre as origin, with x -axis being the rotating axis and z -axis aligning with V_Z . The z -axis is referred to as the downwind axis.

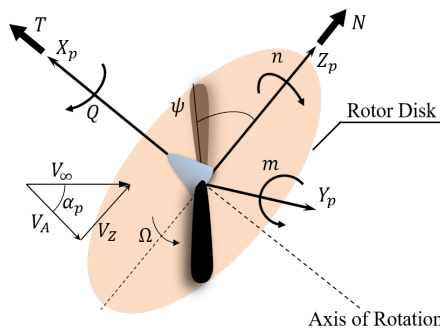


Figure 3.2: Aerodynamic loads on a propeller at incidence

As a consequence of non-zero incidence angle, axisymmetric assumption is no longer valid. Local velocity and angle of attack for each blade section vary with azimuth position ψ on the rotor disk, therefore an imbalance of lift and drag forces exists on a blade section over

a full revolution. As will be further discussed, lift imbalance creates an in-plane moment n around the downwind axis and drag imbalance causes normal force N along the downwind axis. Furthermore, because blade loading depends quadratically on relative wind speed, the local variations in velocity and angle of attack cause change in disk averaged thrust T and torque Q in respect to their values at axial flow condition. The main forces and moments affecting rotor performance at high incidence are defined in Fig. 3.2.

This research concentrates on the development of a computationally efficient method to model the four proprotor aerodynamic forces and moments (T , Q , N and n) at high incidence, a condition typical during VTOL transition. To keep it computationally efficient, the proprotor loads are given in explicit form. The model also takes into account proprotor geometry to aide preliminary design requirements.

A review of notable researches in this field is introduced in the section 3.1.2, followed by a detailed derivation of the mathematical model in analytical form in section 3.2. A dedicated wind-tunnel test for a rotor with known geometry is documented in the third section and its main results are used to validate the proposed analytical model. Main findings and comparison with experimental results are presented in section 3.3.

3.1.2 Literature review

Studies on rotor at non-zero incidence angle first appeared in [Har18]-[Gla19]. These early results focused on stability issues of fixed wing aircraft at relatively a small pitch angle. Their methods were based on momentum theory and were linearised by assuming small angles. The resulting methods cannot consider the effect of blade shape on rotor off-axis loads.

Reference [Rib45b] and [Rib45a] derived an analytic model for propeller off-axis loads. The model considers propellers to be vertical fins having an equivalent side area, and thus propeller planform shape, including chord and pitch angle laws, was considered. The linearised theory showed good agreement for incidence angle up to 20° . A further extension in [DY65] attempted to simplify the linear model in [Rib45b] and cover a higher incidence angle range to 65° . However, authors have found that singularities around 90° incidence angle and minor errors in the derivation limited its application.

Various numerical models have also been proposed to treat rotor performance at incidence. The development of a numerical method enabled more detailed analysis based on either blade element theory (BET), vortex method and numerical solution of Navier-Stokes equations. Notable research includes the blade element momentum theory formulated in [Lei06], dynamic inflow model for helicopter rotor in [PH88]. A more recent blade element study in [Len+19a] observed several particular aerodynamic phenomena associated with high incidence flight condition. A stall delay model and inflow model were determined to be critical in achieving good correlation with experimental data. Despite the advancements, these numerical methods were relatively costly to be integrated into a full-vehicle optimisation routine.

It can be concluded that a more detailed yet computationally efficient approach is of

interest for VTOL capable convertible aircraft studies. Evidence appears in recent researches on propeller off-design conditions of UAVs. Experimental research in [The+17] provided forces and moments measurements over a wide range of incidence angles and freestream speeds on small-scale propellers. A set of new parametric models was recently proposed in [GD19]. The model followed first-principle blade element derivations. Experimental data were needed for training to determine four model parameters. Geometry information was implicitly considered. The model was computational efficient, however, prediction of off-axis loads directly from propeller geometry might be difficult.

In view of past studies, the current study presents an analytic data-driven model with significant advantage in computational efficiency over current numerical approach. In addition, the model overcomes constraining hypothesis in conventional momentum methods presented in [Lei06] and [Joh12], for example, to be better suited for VTOL transition flight phase. Uniform disk loading is assumed in these theories because they focus on high-speed forward flight helicopters, where induced velocity is of smaller order of magnitude compared to freestream. This potential error has been mentioned in [Lei06] and [Bra74]. Generally these theories are applicable to high-speed forward flight ($\alpha_p \approx 90^\circ$).

To present the current research, the model formulation is firstly introduced in the next section. Proprotor geometry is used to calculate model coefficients, and axisymmetric thrust and power curves, which are easy to predict theoretically or to be obtained experimentally, are needed as a base case. In the following section, results from a small-scale proprotor test are presented to validate the current model. The comparison demonstrates sufficient capability in current model to estimate asymmetric force and moment while power consumption is usually underestimated at high incidence conditions. The proposed method is sufficiently accurate and has significant advantage in computational efficiency, and thus is suitable for preliminary vehicle design or real-time applications.

3.2 Theoretical Analysis and Analytic Model Derivations

3.2.1 Blade element analysis

To better elucidate the formulation of analytical models, it is imperative to understand the main aerodynamic loads present on the proprotor blade. The production of these force and moment will be briefly introduced in this section using blade element analysis. Axial flight condition will first be analysed and then expanded to conditions at non-zero incidence.

3.2.1.1 Axial flight condition

A rotor is considered to be immersed in uniform freestream whose direction is in the axis of rotation. Under such an assumption, each infinitesimal blade section at the same radius r from hub should encounter identical flow condition, and thus the flowfield is axisymmetric.

The analysis will be limited to low speed condition, hence incompressible flow is assumed.

Consider a blade section along the circumference at radius r from the axis of rotation. Its orientation is determined relative to rotor disk plane, which is represented by the horizontal lines in Fig. 3.3. The local pitch angle β is defined as the angle between the sectional zero-lift line and the rotor disk plane, as in [Phi04].

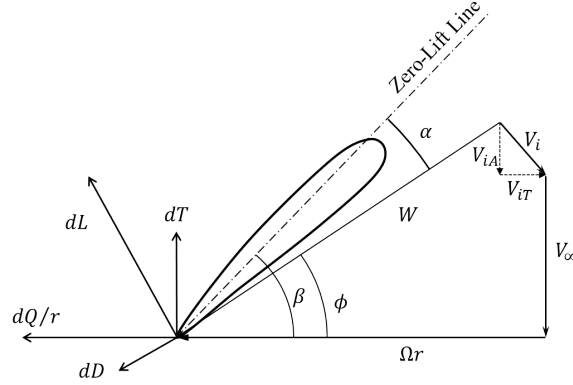


Figure 3.3: Blade section in axial flow

As the blade rotates, there are two major components of imposed flow velocity in Fig. 3.3. Firstly, the freestream velocity V_∞ and secondly circumferential rotation velocity Ωr .

Besides V_∞ and Ωr , velocity V_i induced by the production of thrust and torque on the rotor blade is also depicted in Fig. 3.3. To produce forward thrust, momentum must be added to the fluid in axial direction, thus creating an incremental velocity component in the rotation axis V_{iA} . To sustain rotor rotation, a torque must be supplied, and similarly a tangential flow component V_{iT} is induced due to the exchange of angular momentum.

The local effective wind velocity W is the vector sum of all the velocity components. The angle between W and propeller disk plane is inflow angle ϕ . The difference between blade pitch and inflow angle gives the local angle of attack $\alpha = \beta - \phi$.

The lift and drag of the blade section can be resolved in directions perpendicular and parallel to the effective wind respectively, taking chord Reynolds number and local angle of attack into account. They can then be transferred into sectional thrust and torque.

$$\begin{aligned} dT &= \frac{1}{2} \rho W(r)^2 c(r) [C_L(r) \cos \phi(r) - C_D(r) \sin \phi(r)] dr \\ dQ &= \frac{1}{2} \rho W(r)^2 c(r) [C_L(r) \sin \phi(r) + C_D(r) \cos \phi(r)] r dr \end{aligned} \quad (3.1)$$

Rotor thrust and torque can be found by integrating Eq. 3.1 along the blade radius.

Because of the axisymmetric flow condition, the analysis is independent of blade azimuthal position. The total thrust and torque are given in Eq. 3.2.

$$\begin{aligned} T &= \pi \rho R^2 \int_{\bar{r}_0}^1 W(\bar{r})^2 \sigma(\bar{r}) [C_L(\bar{r}) \cos \phi(\bar{r}) - C_D(\bar{r}) \sin \phi(\bar{r})] d\bar{r} \\ Q &= \pi \rho R^3 \int_{\bar{r}_0}^1 W(\bar{r})^2 \sigma(\bar{r}) [C_L(\bar{r}) \sin \phi(\bar{r}) + C_D(\bar{r}) \cos \phi(\bar{r})] \bar{r} d\bar{r} \end{aligned} \quad (3.2)$$

where $\sigma = \frac{N_{bc}}{2\pi R}$ is rotor local solidity. Typically the thrust and torque are normalised according to air density ρ , rotor tip speed ΩR and disk area $S_p = \pi R^2$.

$$\begin{aligned} C_T &= \frac{T}{\rho(\Omega R)^2 S_p} = \int_{\bar{r}_0}^1 \left[\frac{W(\bar{r})}{\Omega R} \right]^2 \sigma(\bar{r}) [C_L(\bar{r}) \cos \phi(\bar{r}) - C_D(\bar{r}) \sin \phi(\bar{r})] d\bar{r} \\ C_P &= \frac{Q\Omega}{\rho(\Omega R)^3 S_p} = \int_{\bar{r}_0}^1 \left[\frac{W(\bar{r})}{\Omega R} \right]^2 \sigma(\bar{r}) [C_L(\bar{r}) \sin \phi(\bar{r}) + C_D(\bar{r}) \cos \phi(\bar{r})] \bar{r} d\bar{r} \end{aligned} \quad (3.3)$$

3.2.1.2 Non-zero incidence angle

At non-zero α_p , freestream can be broken down into an axial component $V_A = V_\infty \cos \alpha_p$ and $V_Z = V_\infty \sin \alpha_p$ in the rotor disk plane. Component V_A has a reduced freestream effect in axial direction and V_Z causes a variation of flow condition as a function in blade azimuthal position ψ .

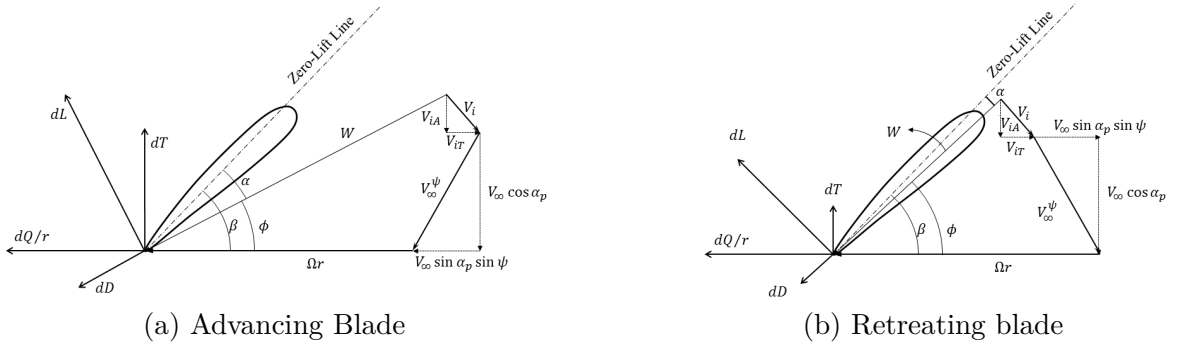


Figure 3.4: Flow directions of advancing and retreating blade sections

Blade element analysis for non-zero α_p follows the same fashion except that most flow components vary with ψ , which is defined to be zero when the blade is aligned with the downwind direction.

Flow conditions for a blade section on two sides of the rotor are illustrated in Fig. 3.4.

On the advancing side of the rotor, where $0 < \psi < \pi$, the in-plane projection is in the same direction of blade rotation. Its effect is to increase local relative wind speed and angle

of attack. The opposite is true for the retreating side, where $\pi < \psi < 2\pi$. As a consequence, the magnitude and direction of local relative wind for each blade section are now functions of \bar{r} and ψ . Sectional lift and drag coefficients also depend on ψ . Therefore the mean thrust and power coefficients become double integration in both \bar{r} and ψ .

$$\begin{aligned} C_T &= \int_0^{2\pi} \int_{\bar{r}_0}^1 \left[\frac{W(\bar{r}, \psi)}{\Omega R} \right]^2 \sigma(\bar{r}) [C_L(\bar{r}, \psi) \cos \phi(\bar{r}, \psi) - C_D(\bar{r}, \psi) \sin \phi(\bar{r}, \psi)] d\bar{r} d\psi \\ C_P &= \int_0^{2\pi} \int_{\bar{r}_0}^1 \left[\frac{W(\bar{r}, \psi)}{\Omega R} \right]^2 \sigma(\bar{r}) [C_L(\bar{r}, \psi) \sin \phi(\bar{r}, \psi) + C_D(\bar{r}, \psi) \cos \phi(\bar{r}, \psi)] \bar{r} d\bar{r} d\psi \end{aligned} \quad (3.4)$$

The imbalance of sectional forces results in axisymmetric normal force and in-plane moment in a global sense. The normal force can be explained by taking the net contribution of tangential force in the downwind axis, as shown in Eq. 3.5.

$$\begin{aligned} C_N &= \frac{N}{\rho(\Omega R)^2 S_p} \\ &= \frac{1}{2\pi} \int_0^{2\pi} \sin \psi \int_{\bar{r}_0}^1 \left[\frac{W(\bar{r}, \psi)}{\Omega R} \right]^2 \sigma(\bar{r}) [C_L(\bar{r}, \psi) \sin \phi(\bar{r}, \psi) + C_D(\bar{r}, \psi) \cos \phi(\bar{r}, \psi)] \bar{r} d\bar{r} d\psi \end{aligned} \quad (3.5)$$

The in-plane moment is obtained by taking the moment of thrust force around the downwind axis in Eq. 3.6.

$$\begin{aligned} C_n &= \frac{n}{\rho(\Omega R)^2 S_p R} \\ &= \frac{1}{2\pi} \int_0^{2\pi} \sin \psi \int_{\bar{r}_0}^1 \left[\frac{W(\bar{r}, \psi)}{\Omega R} \right]^2 \sigma(\bar{r}) [C_L(\bar{r}, \psi) \cos \phi(\bar{r}, \psi) - C_D(\bar{r}, \psi) \sin \phi(\bar{r}, \psi)] \bar{r} d\bar{r} d\psi \end{aligned} \quad (3.6)$$

3.2.2 Thrust and power model

Rotor thrust and power coefficients have been well studied for axisymmetric conditions, a semi-empirical estimation for an arbitrary propeller can be found in [VM59]. For fixed-pitch configuration at zero incidence angle, the coefficients mainly depend on rotor tip speed ratio $\lambda_\infty = \frac{V_\infty}{\Omega R}$, which is the ratio of freestream speed and the rotor tip speed. Reference [VM59] suggested a linear approximation for thrust and power coefficients :

$$C_T = K \pi \bar{r}' \sigma' \cos \beta' (\lambda_{\infty 0T} - \lambda_\infty) \quad (3.7)$$

$$C_P = K (\pi \bar{r}')^2 \sigma' \sin \beta' (\lambda_{\infty 0P} - \lambda_\infty) \quad (3.8)$$

where K is an empirical constant and \bar{r}' is the position of the representative section in percentage radius (generally 75%). The solidity σ' and pitch angle β' are evaluated at the representative section. Two important parameters are $\lambda_{\infty 0T}$ and $\lambda_{\infty 0P}$, they are the tip speed ratios where the thrust and power coefficients reach zero respectively. They can be found

graphically or estimated empirically in [VM59].

For a non-zero incidence angle, two additional ratios are used to describe freestream condition: rotor climb inflow ratio $\lambda_c = \frac{V_\infty \cos \alpha_p}{\Omega R}$ is taken from the rotation axis and rotor advance ratio $\mu = \frac{V_\infty \sin \alpha_p}{\Omega R}$ is taken from the flow component parallel to disk plane. For zero incidence angle, $\lambda_\infty = \lambda_c$ and $\mu = 0$.

Ref. [DY65] proposed an analytical approach to apply a high incidence angle correction factor to thrust and power coefficients in an effective axisymmetric condition with the same climb inflow ratio λ_c . The correction factor is a function of both climb inflow ratio λ_c and advance ratio μ .

$$\eta_T = \frac{C_T(\mu, \lambda_c)}{C_T(0, \lambda_c)} \quad (3.9)$$

$$\eta_P = \frac{C_P(\mu, \lambda_c)}{C_P(0, \lambda_c)} \quad (3.10)$$

This method proves to be sufficiently accurate even for high incidence angles and it forms the basis for off-axis efforts modelling, and thus is briefly presented in this section.

3.2.2.1 Local advance ratio

As seen in the blade element analysis in off-axis condition, inflow angle ϕ is a function in ψ . It reaches a minimum at $\psi = \pi/2$ and a maximum at $\psi = 3\pi/2$. This variation of inflow angle ϕ can be characterised by local speed ratio at representative blade section.

$$\lambda_{local} = \frac{\lambda_c}{1 + \mu \sin \psi / \bar{r}'} \quad (3.11)$$

We also denote three particular local advance ratios at $\psi = 0, \pi/2$ and $3\pi/2$.

$$\lambda_0 = \lambda_c \quad (3.12)$$

$$\lambda_{min} = \frac{\lambda_c}{1 + \mu / \bar{r}'} \quad (3.13)$$

$$\lambda_{max} = \frac{\lambda_c}{1 - \mu / \bar{r}'} \quad (3.14)$$

From linear approximations in [VM59], the local thrust coefficient can be related to freestream dynamic pressure and local advance ratio.

$$C_T(\psi) = K \pi \bar{r}' \sigma \cos \beta' (\lambda_{\infty 0T} - \lambda_{local}) \left(\frac{\lambda_c}{\lambda_{local}} \right)^2 \quad (3.15)$$

3.2.2.2 High incidence angle corrections for thrust and power

Variations in blade angle of attack and dynamic pressure induces periodic load variation in ψ , which could be approximated by a 2-harmonic cosine series as in [DY65].

$$\tilde{C}_T(\psi) = A_0 + A_1 \cos\left(\psi - \frac{\pi}{2}\right) + A_2 \cos(2\psi - \pi) \quad (3.16)$$

The curve notably has several characteristic points :

$$\begin{cases} C_{T_{base}} = A_0 - A_2 & \psi = 0 \\ C_{T_{max}} = A_0 + A_1 + A_2 & \psi = \pi/2 \\ C_{T_{min}} = A_0 - A_1 + A_2 & \psi = 3\pi/2 \end{cases} \quad (3.17)$$

This approximation, though not exact, is a reasonable description of sectional thrust variation, as seen in Fig. 3.5. The curve depicts thrust variation at different azimuthal positions of one blade section situated at $76\%R$ for a constant chord propeller with NACA0012 airfoil (see [Len+19b] for details). The analysis was performed at a typical condition with moderate tip speed ratio $\lambda_\infty = 0.14$ and medium incidence $\alpha_p = \pi/4$.

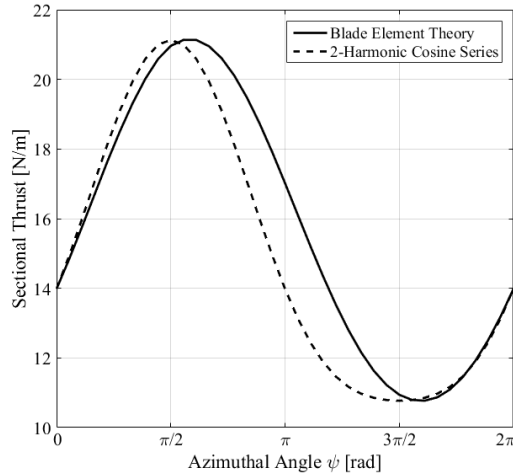


Figure 3.5: Comparison between a blade element solution of thrust variation and cosine approximation

The solid line was obtained by performing blade element analysis with a dynamic inflow model, interested readers could find more detail regarding the model in [PH88]. The dash line is the 2-harmonic cosine series approximation by using the characteristic points calculated from blade element theory. The estimation is reasonable for downwind blade where $\psi \in [0, \pi/2) \cup (3\pi/2, 2\pi)$, while the upwind blade thrust is underestimated. The difference is caused by variation of induced velocity in the upwind part, where upwash tends to increase

local angle of attack for an upstream blade.

The averaged thrust within one revolution can be represented by thrust condition at characteristic points.

$$\begin{aligned}
C_T &= \frac{1}{2\pi} \int_0^{2\pi} \tilde{C}_T(\psi) d\psi \\
&= \frac{1}{2\pi} \int_0^{2\pi} A_0 + A_1 \cos\left(\psi - \frac{\pi}{2}\right) + A_2 \cos(2\psi - \pi) d\psi \\
&= A_0 = \frac{1}{4} (2C_{T_0} + C_{T_{min}} + C_{T_{max}})
\end{aligned} \tag{3.18}$$

Assume the maximal, mean and minimal thrust coefficients correspond to the minimal, mean and maximal speed ratios respectively.

$$\begin{aligned}
C_{T_{max}} &= K \pi \bar{r}' \sigma \cos \beta' (\lambda_{\infty 0T} - \lambda_{min}) (\lambda_c / \lambda_{min})^2 \\
C_{T_0} &= K \pi \bar{r}' \sigma \cos \beta' (\lambda_{\infty 0T} - \lambda_0) \\
C_{T_{min}} &= K \pi \bar{r}' \sigma \cos \beta' (\lambda_{\infty 0T} - \lambda_{max}) (\lambda_c / \lambda_{max})^2
\end{aligned} \tag{3.19}$$

Substitute the local speed ratios from Eqs. (3.12)-(3.14), and insert Eq. (3.19) into Eq. (3.18), the averaged thrust coefficient at climb inflow ratio λ_c and advance ratio μ can be obtained.

$$C_T(\mu, \lambda_c) = K \pi \bar{r}' \sigma \cos \beta' \left[\lambda_{\infty 0T} - \lambda_c + \frac{\lambda_{\infty 0T}}{2} \left(\frac{\mu}{\bar{r}'} \right)^2 \right] \tag{3.20}$$

Notice that without the last term, Eq. (3.20) is identical to the thrust at effective axisymmetric condition. Divided by the thrust coefficient at the corresponding axisymmetric condition, an expression for the thrust correction factor at high incidence angle can be resolved.

$$\eta_T = 1 + \frac{(\mu/\bar{r}')^2}{2(1 - \lambda_c/\lambda_{\infty 0T})} \tag{3.21}$$

Correction factor for power coefficient can similarly be found.

$$\eta_P = 1 + \frac{(\mu/\bar{r}')^2}{2(1 - \lambda_c/\lambda_{\infty 0P})} \tag{3.22}$$

A final correction to thrust and power coefficients is added in [DY65] to make them consistent with analysis of helicopter rotor in forward flight condition detailed in [GM52]. The second term in thrust and power correction factors is multiplied by a geometry term

$\delta(\mu, \lambda_c)$, which varies with α_p .

$$\delta(\mu, \lambda_c) = \frac{3}{2} \cos \beta' \left[1 + \frac{\sigma'}{\tan \beta'} \left(1 + \sqrt{1 + \frac{2 \tan \beta'}{\sigma'}} \right) \left(1 - \frac{\lambda_c}{\sqrt{\lambda_c^2 + \mu^2}} \right) \right] \quad (3.23)$$

The final thrust and power high incidence correction factors are given in Eqs. (3.24), (3.25)

$$\eta_T = 1 + \frac{(\mu/\bar{r}')^2}{2(1 - \lambda_c/\lambda_{\infty 0T})} \delta(\mu, \lambda_c) \quad (3.24)$$

$$\eta_P = 1 + \frac{(\mu/\bar{r}')^2}{2(1 - \lambda_c/\lambda_{\infty 0P})} \delta(\mu, \lambda_c) \quad (3.25)$$

3.2.3 Off-axis loads model

Besides the increase in thrust and power at high α_p , extra off-axis efforts C_N and C_n appear as a result of non-uniform blade loading.

An analytical approach was produced as a linear approximation for small α_p in Refs. [Rib45a]; [Rib45b]. Reference [DY65] later extended the estimation to high incidence cases. The normal force and in-plane moment were modelled as ratios to their respective gradient at zero incidence angle, which were obtained using the theory in [Rib45b]. Reference [DY65] derived these ratios to be $\tan \alpha_p$, which is actually incorrect. The error results in significant overestimation at high α_p and singularity at $\alpha_p = \pi/2$.

The theory in [Rib45b] for off-axis effort gradients at small incidence is presented in this section firstly in a form suitable for low-speed / hover condition. A correct evaluation of normal force and in-plane moment in relation to their gradients at zero incidence is then derived. To validate the theoretical prediction, several results in comparison with classical theories will follow.

3.2.3.1 Gradient of off-axis efforts at zero incidence angle

The theory for normal force and in-plane moment gradients at small incidence angle has been well expressed in [Rib45a]. The gradients are closed form solutions obtained by analysis of deflected momentum through the analogy of a vertical fin having equal area as the projected area of rotor blades perpendicular to the rotor disk. In the expressions, the geometry of the rotor blade was taken into consideration. Although the theory will only be briefly introduced and readers should refer to the original publication for detailed derivation, there are two incentives to present it here again: 1. To remind readers of the results for later usage; 2. The original theory was expressed for high-speed cruise condition, while a form more suitable for low-speed / hover conditions is presented here.

The gradients are expressed in Eqs. (3.26), (3.27) with all velocity terms normalised by ΩR , and dynamic pressure terms by $\frac{1}{2}\rho(\Omega R)^2$, which is more appropriate for low-speed/hover conditions.

$$\left. \frac{\partial C_N}{\partial \alpha_p} \right|_{\alpha_p=0} = \frac{1}{2\pi^2} \frac{k_s f(\lambda_i) \sigma I_1}{\frac{I_1}{I_1 - \Delta} + k_a \sigma I_1} \quad (3.26)$$

$$\left. \frac{\partial C_n}{\partial \alpha_p} \right|_{\alpha_p=0} = \frac{1}{\pi^2} \frac{k_s f(\lambda_i) m}{1 + k_a \sigma (I_1 - \Delta)} \quad (3.27)$$

where λ_i is the induced inflow ratio $\frac{V_i}{\Omega R}$. k_s and k_a are the spinner factor and the sidewash factor taken as constants ($k_s = 1.14$ and $k_a = 0.4$) in the current study, as suggested in [Rib45b]. Their analytical definitions can be found in [Rib45b].

The function $f(\lambda_i)$ is the effect of induced velocity V_i on the dynamic pressure at propeller disk compared to $\frac{1}{2}\rho(\Omega R)^2$, defined in Eq. (3.28).

$$f(\lambda_i) = \frac{\pi^{\frac{3}{2}} \lambda_\infty^{\frac{1}{2}} (\lambda_\infty + \lambda_i) \left[\lambda_\infty (\lambda_\infty + \lambda_i) + (\lambda_\infty + 2\lambda_i)^2 \right]}{\lambda_\infty^2 + (\lambda_\infty + 2\lambda_i)^2} \quad (3.28)$$

For other quantities in Eqs. (3.26), (3.27), we first introduce three integrations based on rotor blade geometry.

$$I_1 = \frac{3}{4} C_{L_\alpha} \int_{\bar{r}_0}^1 \frac{c}{c_{0.75R}} \sin \beta' d\bar{r} \quad (3.29)$$

$$I_2 = \frac{3}{4} C_{L_\alpha} \int_{\bar{r}_0}^1 \frac{c}{c_{0.75R}} \cos \beta' \bar{r} d\bar{r} \quad (3.30)$$

$$I_3 = \frac{3}{4} C_{L_\alpha} \int_{\bar{r}_0}^1 \frac{c}{c_{0.75R}} \frac{\cos^2 \phi}{\sin \phi} \bar{r}^2 d\bar{r} \quad (3.31)$$

where the mean lift line slope C_{L_α} was approximated as $0.95 \times 2\pi$ in [Rib45a].

Terms Δ and m are defined with these geometry integrals.

$$\Delta = \frac{(\sigma I_2 - 2\lambda_i)(\sigma I_2 + 4\lambda_i)}{\sigma(1 + \sigma I_2)} \quad (3.32)$$

$$m = \frac{\sigma I_2 + 4\lambda_i}{2(1 + \sigma I_3)} \quad (3.33)$$

3.2.3.2 Off-axis efforts at high incidence

The off-axis effort gradients calculated from [Rib45b] agree with various experimental data for incidence angle of up to 20° . Linearity however doesn't hold for high incidence angles, and the change in local dynamic pressure and flow angle must be taken into consideration. In

this section, a formulation of off-axis efforts at high incidence is derived in detail for normal force. Expression for the in-plane moment can be derived in a similar procedure.

The normal force N is a result of averaged tangential force projected in downstream direction. The integration of the moment generated by tangential force at propotor hub amounts to propotor torque. From Eq. (3.8), the local torque can be expressed in terms of local advance ratios.

$$\tilde{Q}(\psi) = \frac{4\rho(\Omega R)^2 S_p R}{\pi^2} K \sigma \sin \beta' A(\psi) B(\psi) \quad (3.34)$$

where factor $A(\psi)$ estimates the influence of local dynamic pressure change and factor $B(\psi)$ includes the effect of local inflow angle variation implicitly. The two factors are calculated from Eqs. (3.35), (3.36).

$$A(\psi) = (1 + \mu \sin \psi / \bar{r}')^2 \quad (3.35)$$

$$B(\psi) = \lambda_{\infty 0P} - \frac{\lambda_c}{1 + \mu \sin \psi / \bar{r}'} \quad (3.36)$$

The tangential force \tilde{F}_T can be estimated by dividing the local torque by the representative radius r' , and thus is proportional to torque $\tilde{Q}(\psi)$. For clarity in the following derivations, proportional constants are neglected.

$$\tilde{F}_T(\psi) = \frac{\tilde{Q}(\psi)}{r'} \propto A(\psi) B(\psi) \quad (3.37)$$

Expand Eq. (3.37) and re-arrange terms, the tangential force expression can be reformulated as Eq. (3.38).

$$\tilde{F}_T(\psi) \propto (\lambda_{\infty 0P} - \lambda_c) + \left(\frac{\mu}{\bar{r}'}\right) (2\lambda_{\infty 0P} - \lambda_c) \sin \psi + \left(\frac{\mu}{\bar{r}'}\right)^2 \lambda_{\infty 0P} \sin^2 \psi \quad (3.38)$$

Assume that the averaged normal force N is proportional to the mean of integrated tangential force projected in downwind direction in one revolution. Constant and second order terms in Eq. (3.38) are zero after integration. The normal force is written as a function in α_p and λ_∞ in Eq. 3.40, as it makes the form easier to apply the force and moments gradients in Eqs. 3.26, 3.27.

$$N(\alpha_p, \lambda_\infty) \propto \frac{1}{2\pi} \int_0^{2\pi} \tilde{F}_T(\psi) \sin \psi d\psi \quad (3.39)$$

$$\propto (2\lambda_{\infty 0P} - \lambda_\infty \cos \alpha_p) \lambda_\infty \sin \alpha_p \quad (3.40)$$

Differentiate Eq. (3.40) with respect to incidence angle α_p and evaluate the normal force

gradient at zero incidence.

$$\left. \frac{dN(\alpha_p, \lambda_\infty)}{d\alpha_p} \right|_{\alpha_p=0} \propto \lambda_\infty (2\lambda_{\infty 0P} - \lambda_\infty) \quad (3.41)$$

Thus the evolution of normal force at high incidence can be evaluated as a ratio to normal force gradient at zero incidence with the same λ_∞ . The resultant relation is a product of $\sin \alpha_p$ and λ_∞ terms.

$$\frac{N(\alpha_p, \lambda_\infty)}{\partial N / \partial \alpha_p(0, \lambda_\infty)} = \frac{2\lambda_{\infty 0P} - \lambda_\infty \cos \alpha_p}{2\lambda_{\infty 0P} - \lambda_\infty} \sin \alpha_p \quad (3.42)$$

In a similar manner, the same relation can be obtained for the in-plane moment by using the azimuthal variation of local thrust. The off-axis efforts are expressed as coefficients in Eqs. (3.43), (3.44).

$$C_N = \frac{2\lambda_{\infty 0P} - \lambda_\infty \cos \alpha_p}{2\lambda_{\infty 0P} - \lambda_\infty} \sin \alpha_p \left. \frac{\partial C_N}{\partial \alpha_p} \right|_{\alpha_p=0, \lambda_\infty} \quad (3.43)$$

$$C_n = \frac{2\lambda_{\infty 0T} - \lambda_\infty \cos \alpha_p}{2\lambda_{\infty 0T} - \lambda_\infty} \sin \alpha_p \left. \frac{\partial C_n}{\partial \alpha_p} \right|_{\alpha_p=0, \lambda_\infty} \quad (3.44)$$

3.2.4 Model implementation

In this section, the model derivations were summarised in a suggested way of implementation.

1. Required model inputs.

- Proprotor geometry : R , $\beta(r)$, $c(r)$ (or estimations of integrals I_1, I_2, I_3 in Eqs. (29)-(31)).
- Proprotor axial performance : thrust coefficient $C_T(0, \lambda_\infty)$ and power coefficient $C_P(0, \lambda_\infty)$.
- Freestream conditions : tip-speed ratio λ_∞ , rotor incidence angle α_p .

2. Calculation of model coefficients.

- Decomposition of tip-speed ratio.
 - Climb inflow ratio : $\lambda_c = \lambda_\infty \cos \alpha_p$.
 - Rotor advance ratio : $\mu = \lambda_\infty \sin \alpha_p$.
- Zero thrust and power tip-speed ratios, $\lambda_{\infty 0T}$, $\lambda_{\infty 0P}$.

3. Interpolation of $C_T(0, \lambda_c)$ and $C_P(0, \lambda_c)$.

4. Calculation of high incidence correction factor $\delta(\mu, \lambda_c)$, and then η_T , η_P .

- $\delta(\mu, \lambda_c) = \frac{3}{2} \cos \beta' \left[1 + \frac{\sigma'}{\tan \beta'} \left(1 + \sqrt{1 + \frac{2 \tan \beta'}{\sigma'}} \right) \left(1 - \frac{\lambda_c}{\sqrt{\lambda_c^2 + \mu^2}} \right) \right]$.
- $\eta_T = 1 + \frac{(\mu/\bar{r}')^2}{2(1-\lambda_c/\lambda_{\infty 0T})}$.
- $\eta_P = 1 + \frac{(\mu/\bar{r}')^2}{2(1-\lambda_c/\lambda_{\infty 0P})}$.

5. Calculation of thrust and power coefficients at incidence.

- $C_T(\mu, \lambda_c) = C_T(0, \lambda_c) \eta_T$.
- $C_P(\mu, \lambda_c) = C_P(0, \lambda_c) \eta_P$.
- $\eta_P = 1 + \frac{(\mu/\bar{r}')^2}{2(1-\lambda_c/\lambda_{\infty 0P})}$.

6. Calculation of induced inflow ratio λ_i .

7. Calculation of model coefficients for off-axis efforts.

- dynamic pressure coefficient $f(\lambda_i) = \frac{\pi^{\frac{3}{2}} \lambda_{\infty}^{\frac{1}{2}} (\lambda_{\infty} + \lambda_i) [\lambda_{\infty} (\lambda_{\infty} + \lambda_i) + (\lambda_{\infty} + 2\lambda_i)^2]}{\lambda_{\infty}^2 + (\lambda_{\infty} + 2\lambda_i)^2}$.
- geometric coefficients : Δ and m .
 - $\Delta = \frac{(\sigma I_2 - 2\lambda_i)(\sigma I_2 + 4\lambda_i)}{\sigma(1 + \sigma I_2)}$.
 - $m = \frac{\sigma I_2 + 4\lambda_i}{2(1 + \sigma I_3)}$.

8. Calculation of normal force and in-plane moment gradient around zero incidence angle.

- $\left. \frac{\partial C_N}{\partial \alpha_p} \right|_{\alpha_p=0} = \frac{1}{2\pi^2} \frac{k_s f(\lambda_i) \sigma I_1}{I_1 - \Delta + k_a \sigma I_1}$.
- $\left. \frac{\partial C_m}{\partial \alpha_p} \right|_{\alpha_p=0} = \frac{1}{\pi^2} \frac{k_s f(\lambda_i) m}{1 + k_a \sigma (I_1 - \Delta)}$.

9. Calculation of normal force and in-plane moment at high incidence.

- $C_N = \frac{2\lambda_{\infty 0P} - \lambda_{\infty} \cos \alpha_p}{2\lambda_{\infty 0P} - \lambda_{\infty}} \sin \alpha_p \left. \frac{\partial C_N}{\partial \alpha_p} \right|_{\alpha_p=0, \lambda_{\infty}}$.
- $C_m = \frac{2\lambda_{\infty 0T} - \lambda_{\infty} \cos \alpha_p}{2\lambda_{\infty 0T} - \lambda_{\infty}} \sin \alpha_p \left. \frac{\partial C_m}{\partial \alpha_p} \right|_{\alpha_p=0, \lambda_{\infty}}$.

3.2.5 Comparisons with Classical Theories

The analytical model was compared with classical theories for non-zero incidence angle conditions. These consist of mainly two categories : linear analysis in aircraft stability (Refs. [Rib45a], [Phi04], [Rum42]); and performance analysis on helicopter lift and drag (Refs. [GM52], [Joh12], [Lei06]). The first category considers rotor off-axis loads at small incidence ($\alpha_p \approx 0$) while the second category focuses at α_p near $\pi/2$. Models in these two well-studied conditions serves as benchmark to the validity of the current analytic model, which is applicable to arbitrary α_p .

A small-scale rotor with predefined geometry was used in model validation. The rotor features a constant chord and NACA0012 blade section profile, and thus is referred to as a



Figure 3.6: 3D Printed NACA propellers

NACA rotor. The twist distribution is given as $\beta = \tan^{-1} \frac{C}{r}$, where $C = \tan \beta_{tip}$. The tip blade angle β_{tip} is equal to 20° , as shown in Fig. 3.6. Tabulated chord and pitch distribution laws with root cut-off can be found in Appendix B. A physical model was manufactured for the wind tunnel experiment discussed in the next section.

3.2.5.1 Linearised model for off-axis loads at small incidence

Linearised normal force and in-plane moment models have been used frequently in fixed-wing aircraft researches, since they typically fly at small incidence angle. The original model developed in [Rib45b] is one of these types. A more recent model documented in [Phi04] and implemented in [Goa18] will be used as a reference in this section to demonstrate the accuracy of the proposed model at incidence angle below 45° .

The linearised theory was formulated from a blade element approach. The off-axis force and moments were linearised around $\alpha_p = 0$ based on small angle assumptions. The theory also assumes that freestream velocity is small compared to rotor speed ($\lambda_\infty \ll 1$).

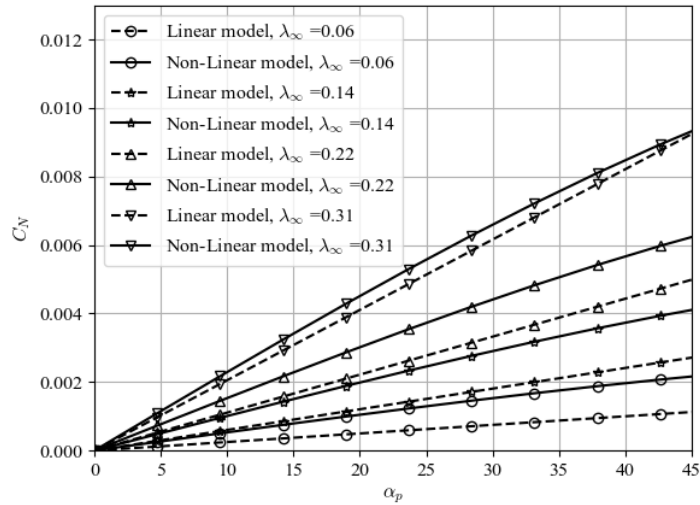


Figure 3.7: C_N of a small-scale rotor versus α_p from theory in [Phi04] and from current theory

Normal force and in-plane moment coefficients are plotted in Fig. 3.7 and Fig. 3.8 respectively. The linear theory results are plotted in a dashed line and results from the current non-linear theory are presented in a solid line. Different markers represent various tip speed ratios.

In Fig. 3.7, the normal force estimations from both theories are compared. The theory in [Phi04] underestimates the normal force. The discrepancies appear to reduce with increasing tip speed ratio. For example, at $\lambda_\infty = 0.06$, the linear theory gives a value 53% lower than the non-linear model at $\alpha_p = 10^\circ$. The difference decreases to 27% at higher tip speed ratio of 0.31. The linear model evidently could not predict the level-off of normal force at higher incidence angle, but such discrepancy is not significant in the low incidence angle range.

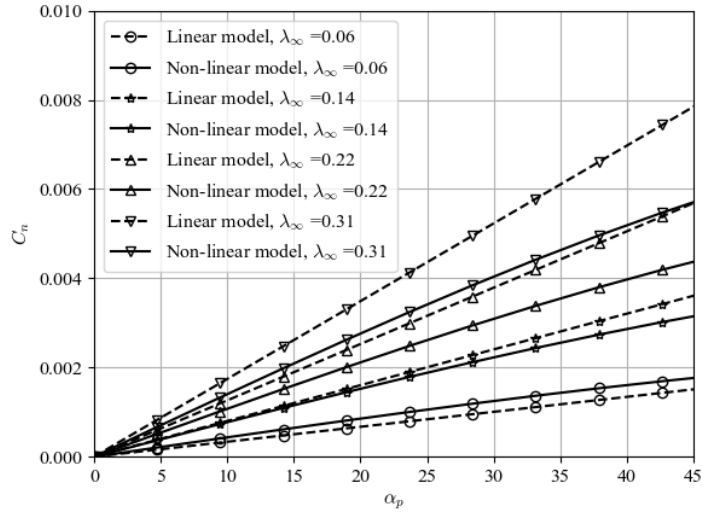


Figure 3.8: C_n of a small-scale rotor versus α_p from theory in [Phi04] and from current theory

For in-plane moment estimations presented in Fig. 3.8, both theories give consistent values for $\lambda_\infty \leq 0.14$. The difference typically doesn't exceed 20% in low incidence angle range. At higher speed ratio, the linear theory starts to underestimate in-plane moment. This is because the assumptions of small angle and low tip speed ratio start to break down.

3.2.5.2 Helicopter forward flight theory

A comparison with classical helicopter forward flight theory may give further insight into the validity of current model at $\alpha_p \approx \pi/2$. A detailed discussion of such analysis can be found in [Joh12].

The theory is based on a linearised blade element model, small angle assumption on inflow angle and non-flow-reversal assumption. The latter was validated in [Joh12] with limitation of $\mu \leq 0.3$. The theory is developed in [Joh12] for articulated straight high aspect-ratio blade. As a result, blade flapping terms were included in the original form. However small-scale rotors are usually hingeless and rather rigid, and thus the extra terms were omitted.

Extensive reviews from [Har08] and [Joh15] further extended the applicable μ range for normal force estimation at higher flight speed. This is also included in the normal force comparison.

From forward flight theory, rotor thrust, power and normal force can be directly resolved for $\alpha_p = \pi/2$. Thrust and normal force are compared with the current model in this section.

The thrust and normal force coefficients are presented in Fig. 3.9 against advance ratio μ . An error band of $\pm 5\%$ is also plotted for each dataset from the current model.

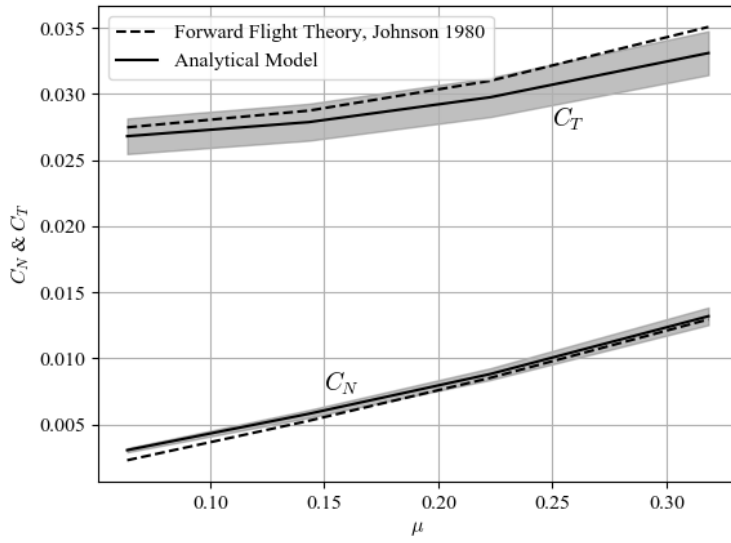


Figure 3.9: Thrust and normal force coefficients of small-scale propeller for various μ

Over the rotor advance ratio range, the prediction of the current model agrees mostly within 5% of the forward flight theory. Both thrust and normal coefficients increase with advance ratio with C_N exhibiting a more linear characteristics.

Classical forward flight theory starts to overestimate thrust coefficient at high advance ratio. Considering the theory's limit of $\mu \leq 0.3$, the overestimated value might be explained by the extension of the flow reversal region. The current model interprets aerodynamic characteristics according to axial rotor performance (usually obtained by wind tunnel tests), and thus the thrust performance is restricted while no explicit treatment of flow reversal is included.

Classical forward flight theory is in close agreement with the current model in normal force prediction. C_N estimation in classical forward flight theory consists of two parts: induced and profile drag. The first part considers inflow angle variation due to thrust induced flow while the second part considers contributions due to sectional and radial drag. The agreement in Fig. 3.9 suggests that influences from both parts has been included in the current model and

the results are quantitatively consistent.

3.2.5.3 Computational efficiency

One of the major advantage of the analytic model is its computational efficiency. Table. 3.1, illustrates typical order of magnitude of processor time per calculation case for widely-used propeller models. The figures were obtained through in-house calculations on similar low Reynolds number proprotor cases over a limited test conditions ([Len+19a], [Jo+19], [Gou+17]).

Numerical method	Level of resolution	CPU time per case [s]
Analytical method (current)	Low	10^{-3}
BEMT [Len+19a]	Medium	10^1
Non-Linear Vortex Lattice Method [Jo+19]	High	$10^4 - 10^6$
Unsteady RANS [Gou+17]	High	10^7

Table 3.1: Order of magnitude of CPU time per case for different numerical propeller models

According to the table, the current method has a significant advantage over other methods in preliminary design phase, where the requirement of rapid and robust calculation outweighs solution precision. Its computational efficiency may also benefit further real-time applications. The accuracy of current model will be further discussed in the following section through comparison of experimental data.

Blade element momentum method is also widely used for propeller design. However, since axisymmetric flow condition no longer exists, the method must be expanded to calculate solution at each azimuthal angle, hence the increased CPU time compared to a usual axisymmetric case.

Both non-linear vortex lattice method and unsteady RANS method solve directly wall boundary condition to achieve high resolution spatial solution. A large amount of calculation is required for sufficient wake development in order to obtain steady state solution. Therefore these methods are more suitable for detailed design.

3.3 Experimental Studies

To validate the analytical model derived in section 3.2, an experimental study was conducted and is presented in this section. The test was performed in low Reynolds number wind tunnel SaBRe at ISAE-Supaero to simulate typical UAV transition flight condition. An in-house manufactured rotor was used to ensure sufficient geometric information is available to compare experimental results and numerical model.

3.3.1 Test Setup

3.3.2 SaBRe Windtunnel

The measurement, along with other test campaign in the current study, was carried out at ISAE low Reynolds number wind tunnel SaBRe (Fig. 3.10), which is dedicated for micro aerial vehicles research.

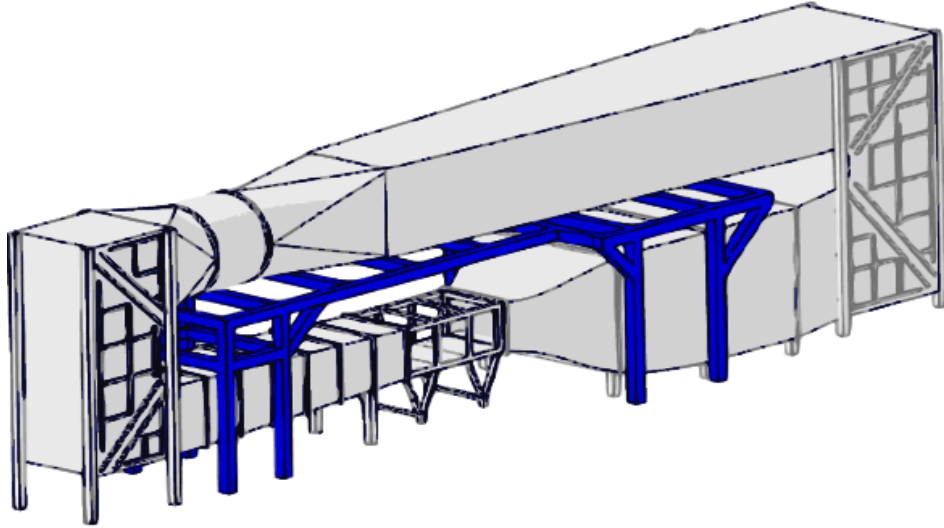


Figure 3.10: ISAE SaBRe Wind Tunnel

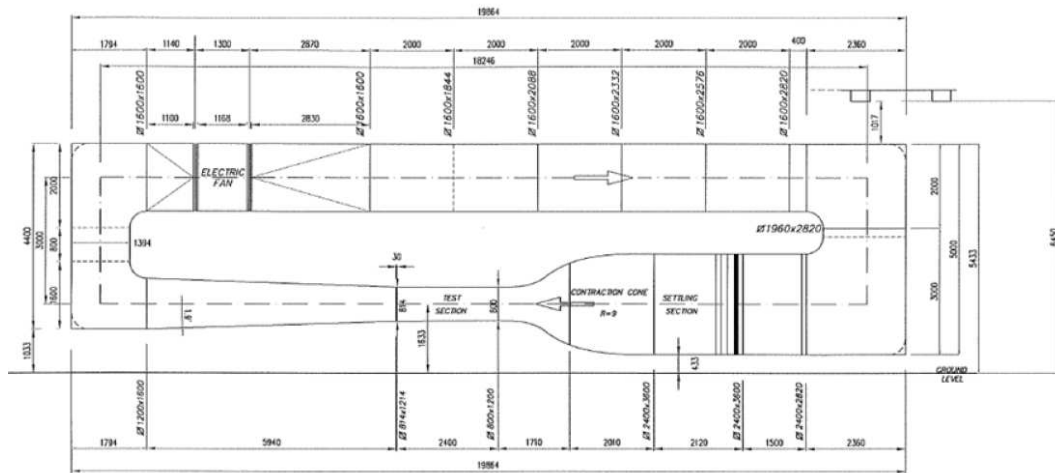
The windtunnel employs a closed-circuit design to achieve better flow quality, as shown in Fig. 3.11. Air flow is accelerated by a variable pitch fan whose pitch setting is regulated to reduce turbulent level. Multiple layers of honeycomb grid in the settling section further stabilise the flow before testing section. Calibration conducted in the windtunnel suggested turbulent intensity of less than 0.1% for windtunnel speed between $2m/s$ and $20m/s$.

The test section is $2400mm$ in length and has a cross-section with entrance dimension of $1200 \times 800mm$. To minimise windtunnel wall effect on streamwise pressure gradient, the test section diverges by $7mm$ on each side towards downstream. Parts of test section window frame can be removed during test, but they remained closed during all tests for current study.

3.3.2.1 Mounting and measurement system

The propeller-motor assembly was supported by a rotating strut installed from the test section ceiling. The metal strut was driven by an actuator which allowed 180° rotation around its vertical axis in either direction, simulating variation of incidence angle.

At the lower tip of the strut, a custom-designed five-component balance was mounted both as a structural connection to the propeller-motor assembly and as the load measuring



3.3.2.2 Tested Rotors

A 9-inch Graupner E-prop was first tested to compare with experiments documented in [The+14] for validation. The rotor was operated at 4000 and 4500RPM with freestream velocity $V_\infty = 6m/s$. The compared study controlled motor voltage and thus rotation speed varied with incidence angle. Due to excessive vibration below 4000RPM in current setup, the rotation speeds could not exactly match with published data points.

Rotation Speed (<i>RPM</i>)	Freestream Velocity (<i>m/s</i>)	
4000	3	6
4500	3	6

Table 3.2: E-prop Test Matrix

For model validation, the small-scale NACA rotor discussed earlier was used since its geometry information is fully accessible. The rotor was tested at four different tip speed ratios. To achieve the desired λ_∞ 's, freestream velocity and rotation speed were changed as listed in Table. 3.3. The reference Reynolds numbers at 75% radius are also listed, which takes into account both freestream and rotation speed.

$$Re_{\bar{r}=0.75} = \frac{V_\infty c}{\nu} \sqrt{1 + \left(\frac{0.75}{\lambda_\infty}\right)^2} \quad (3.45)$$

Tip Speed Ratio λ_∞	Freestream Velocity (<i>m/s</i>)	<i>Re</i> at 75% <i>R</i>
0.06	3	5.3×10^4
0.14	6	4.7×10^4
0.22	9	4.5×10^4
0.32	10	3.5×10^4

Table 3.3: NACA Propellers Test Matrix

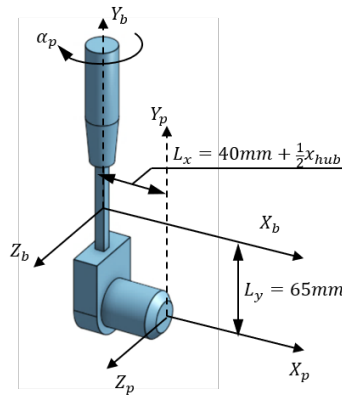


Figure 3.13: Balance and propeller coordinates

3.3.3 Data Process

3.3.3.1 Coordinate system

To describe the rotor assembly movement and the transformation from measurement datum to rotor centre, a clear definition of the coordinate system is required.

Two coordinates are used. The propeller frame has its origin O_p at the rotor centre, and its orientations are defined in the same way as the analytical model. Therefore its x -axis coincides with the axis of rotation, and its y -axis points vertically towards the wind tunnel ceiling.

The balance frame has the same orientation as the propeller system, but its origin is at the measurement datum, which is located $L_y = 0.065m$ above, and $L_x = 0.04m$ behind the base of the rotor mount. The geometric relation between two coordinates is illustrated in Fig. 3.13.

Rotor thrust T , torque Q , normal force N , in-plane and pitch moments (n , p) were measured during the test. All rotor aerodynamic loads follows the same definition as in Fig. 3.2. As mentioned before, the balance used for measurement is only sensitive in five components, namely two forces and three moments along an orthogonal coordinate. Based on [Phi04]; [YR60]; [The+14], side force Y is negligible and thus the insensitive force axis is aligned with Y_b -axis.

3.3.3.2 Compensation for external disturbances

The force measurement from 5-component balance contains several external loads apart from rotor aerodynamic efforts, and thus must be compensated to obtain propeller loads. The external disturbances are categorised as following.

1. Static structural load : It is a result of the gravitational force of the test bench and rotor-motor assembly. This component is measured for each rotor at various incidence angles. In the general form it contains five components, and its variation with incidence angle is caused by the slight alignment error in balance installation, which is derived in appendix A.

$$\begin{bmatrix} \vec{F}_0 \\ \vec{M}_0 \end{bmatrix} = [F_{x0}, F_{z0}, M_{x0}, M_{y0}, M_{z0}]^T \quad (3.46)$$

2. Static aerodynamic load : The second component is the aerodynamic efforts produced by structures other than the rotor, and is denoted by subscript $aero$. The structure contains mainly cylinder geometries, and thus airflow around those structures should be well separated at testing speeds so that the Reynolds number effect is negligible according to [Hoe01]. This component is obtained through two measurements. Firstly, with the rotor

uninstalled and $V_\infty = 0$, the motor mass effect F_{m0} and M_{m0} are measured at various incidence angles. The wind-tunnel is subsequently run at test speed and acquisitions of F_m^* and M_m^* are made at corresponding incidence angles. The aerodynamic load is further derived as the difference between these two measurements.

$$\begin{bmatrix} \vec{F}_{aero} \\ \vec{M}_{aero} \end{bmatrix} = \begin{bmatrix} \vec{F}_m^* \\ \vec{M}_m^* \end{bmatrix} - \begin{bmatrix} \vec{F}_{m0} \\ \vec{M}_{m0} \end{bmatrix} \quad (3.47)$$

To compensate the influence of atmosphere condition on dynamic pressure, the aerodynamic disturbances are further normalised by measured dynamic pressure.

$$\begin{bmatrix} \vec{C}_{F_{aero}} \\ \vec{C}_{M_{aero}} \end{bmatrix} = \frac{2}{\rho V_\infty^2} \begin{bmatrix} \vec{F}_{aero} \\ \vec{M}_{aero} \end{bmatrix} \quad (3.48)$$

To obtain the rotor aerodynamic forces and moments, those two external disturbances are subtracted from the raw data measured at the measurement datum (F_b^* , M_b^*). The static aerodynamic effects are scaled with measured dynamic pressure before compensation.

$$\begin{bmatrix} \vec{F}_b \\ \vec{M}_b \end{bmatrix} = \begin{bmatrix} \vec{F}_b^* \\ \vec{M}_b^* \end{bmatrix} - \begin{bmatrix} \vec{F}_0 \\ \vec{M}_0 \end{bmatrix} - \frac{1}{2} \rho V_\infty^2 \begin{bmatrix} \vec{C}_{F_{aero}} \\ \vec{C}_{M_{aero}} \end{bmatrix} \quad (3.49)$$

To obtain aerodynamic efforts at the rotor centre, the compensated forces and moments should be transformed. Following the test bench convention in Fig. 3.13, the transformation is given in Eq. 3.50.

$$\begin{bmatrix} \vec{F}_p \\ \vec{M}_p \end{bmatrix} = \begin{bmatrix} 1 & 0 & 0 & 0 & 0 \\ 0 & 1 & 0 & 0 & 0 \\ 0 & L_y & 1 & 0 & 0 \\ 0 & L_x & 0 & 1 & 0 \\ -L_y & 0 & 0 & 0 & 1 \end{bmatrix} \begin{bmatrix} \vec{F}_b \\ \vec{M}_b \end{bmatrix} \quad (3.50)$$

where L_x and L_y are the moment arms from measurement datum to the rotor centre in x and y directions, respectively. It is assumed that, after compensation of the mass effect, force in y direction is negligible.

3.3.3.3 Test Bench Validation

The five components obtained from the experiment with Graupner E-prop were compared with values in [The+17] at similar rotation speeds, namely, thrust T , normal force N , pitching moment p , in-plane moment n and torque Q . All results are presented for an incidence angle from 0° to $\pi/2$ by an interval of $\pi/6$, and are in the form of non-dimensional coefficients.

Figures 3.14 and 3.15 compare results on thrust and torque. The curves from the ISAE experiment share a similar trend in [The+17]. At constant rotational speed, the thrust and torque coefficients increase with incidence angle, and reach peak value beyond 90° .

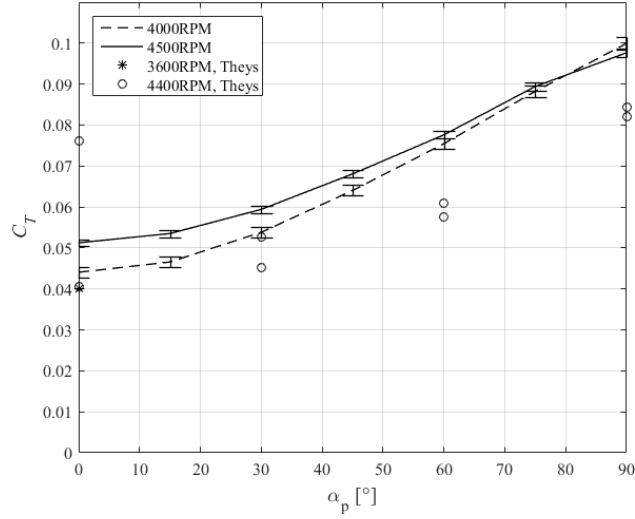


Figure 3.14: C_T comparison with [The+17]

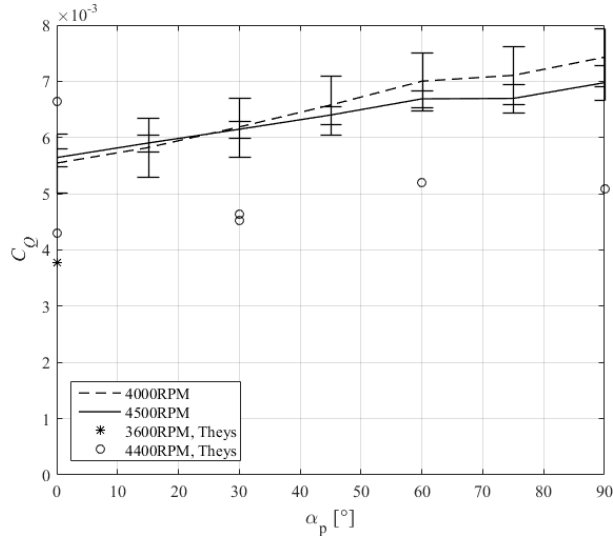


Figure 3.15: C_Q comparison with [The+17]

An overestimation can be observed when compared with [The+17]. The discrepancy is highly likely due to the difficulty in matching rotor rotational speed. The rotor in [The+17] was controlled by constant voltage input, and thus rotational speed varies slightly with incidence angle. In general, the propeller rotated at a higher speed than the comparison case, producing larger thrust and torque coefficients.

Off-axis forces and moments are presented in Figs. 3.16, 3.17 and 3.18.

In Figs. 3.16, 3.17, C_N and C_n are presented. The normal force increases with α_p until around $\pi/3$. The measurement from the two experiments agree well in the tested range.

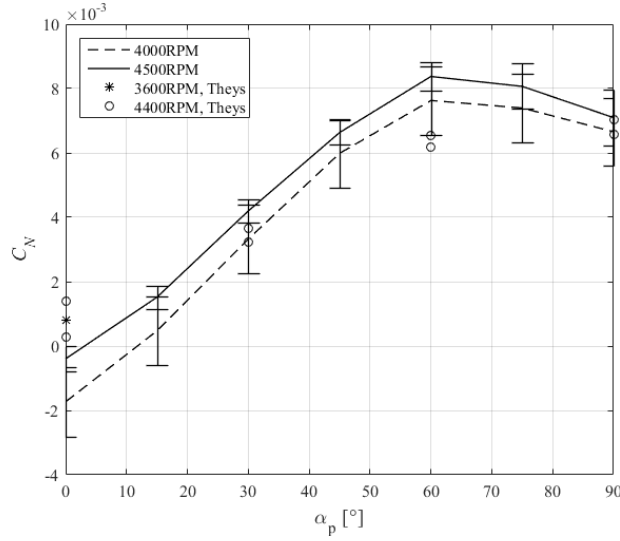


Figure 3.16: C_N comparison with [The+17]

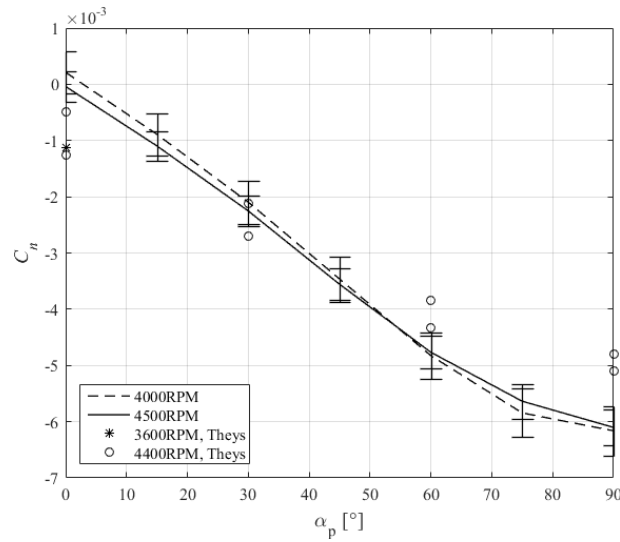


Figure 3.17: C_n comparison with [The+17]

The in-plane moment measurement largely agrees with data in [The+17]. The data suggest a quasi-linear increase in n till around $\pi/3$. The off-axis moment levels off thereafter near $\pi/2$, and a slightly larger value is observed compared to data in [The+17].

Figure 3.18 shows the variation in pitching moment, the supposedly secondary rotor off-axis load. Current measurement is consistent with data in [The+17]. C_p rises gradually from zero up to around $\pi/3$, where a sharp increase follows.

The origin of pitch moment is likely due to 3 dimensional effects when the blades are nearly aligned with the flow direction. It may be further analysed by comparing phase shift

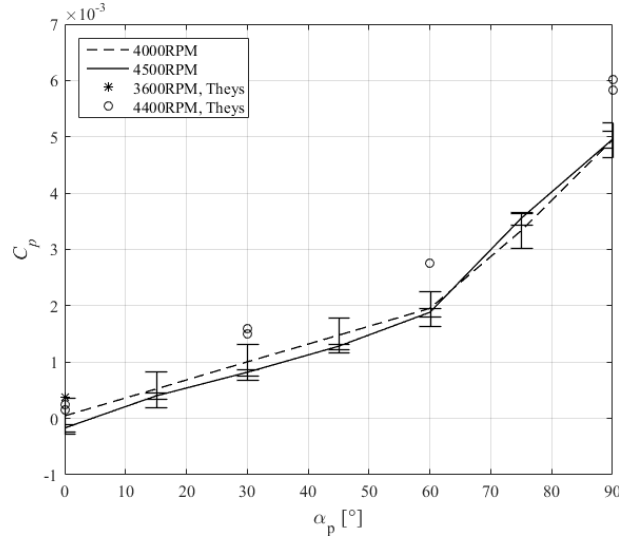


Figure 3.18: C_p comparison with [The+17]

to in-plane moment. The phenomena may be roughly simulated through pressure distribution on a circular wing according to [Bra74].

The comparison, although not exact, demonstrates the validity of the propeller test bench in the ISAE-SaBRe wind tunnel in providing credible force and moment measurement for a rotor at high incidence angle. Data acquired from the balance capture principle variation in rotor aerodynamic loads and are accurate for qualitative analysis at practical range.

3.4 Results and discussions

3.4.1 Validation of the analytical model for thrust and power

Comparisons between the analytical model and the small-scale rotor test were made for the four tip speed ratios mentioned before. In the following figures, experimental data were plotted by asterisk mark of different colors for the four λ_∞ . Theoretical results were calculated from coefficients obtained in experiments at zero incidence angle, and were plotted in solid lines for the current theory and in dashed lines for the theory in Ref. [DY65].

In Fig. 3.19, the thrust coefficient was compared between the analytical models and the experimental data. As expected from classic rotor analysis, at axial conditions, the thrust coefficient decreases with λ_∞ . The theoretical value matches exactly with the experimental results since the thrust ratio η_T is unity at zero incidence. With increasing α_p thrust starts to rise gently initially, and more drastically at higher incidence. The variation is larger at high advance ratio. The differences between two analytical models are small, as the theory in Ref. [DY65] uses simplified approximations for geometric integrals.

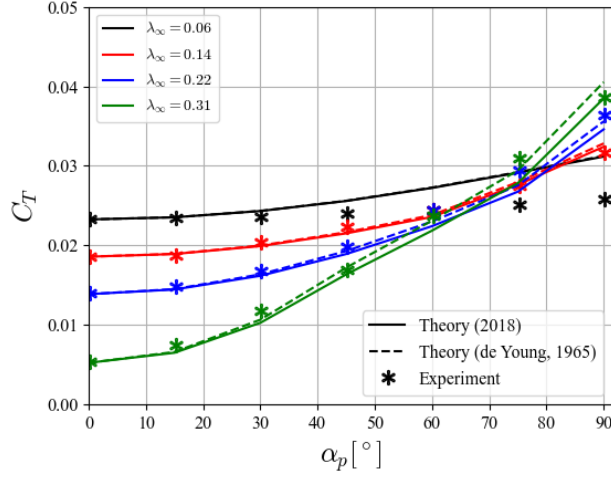


Figure 3.19: C_T of a small-scale rotor against incidence angle for various λ_∞

The theoretical results agreed reasonably well for all tested conditions, particularly at smaller α_p . At around $\alpha_p = \pi/3$ a convergence region can be observed, where all curves seem to pass through. A slight over estimation is observed in low tip-speed ratio $\lambda_\infty = 0.06$.

The comparison for power coefficient is depicted in Fig. 3.20. The non-linear trend is very similar to that of thrust coefficient. However, the difference between test data and theoretical results is larger for tip-speed ratio $\lambda_\infty \leq 0.22$. The on-set angle of incidence of deviation decreases with tip-speed ratio, which are at 30° for $\lambda_\infty = 0.22$ and at 15° for $\lambda_\infty = 0.31$. Beyond the on-set incidence angle, theoretical estimation underestimates prop rotor torque.

The reason for such deviation is probably due to effect of in-plane flow component on tangential force hypothesis. The 2-harmonic cosine series model used may not be able to capture the exact tangential force under high incidence flow.

By calculating the rotor advance ratio μ at on-set incidence, the model is found to be accurate up to $\mu_{crit} = 0.08 \sim 0.11$.

From the validation, it can be concluded for the tested small-scale propeller, the analytical model applies well for various combinations of λ_∞ and α_p . It also explains well the increasing amplitude of thrust and power coefficients at higher λ_∞ . The high incidence thrust and power correction factors in Eqs. (3.24), (3.25) can be re-written in the form of Eqs. (3.51), (3.52).

$$\eta_T = 1 + \frac{\lambda_\infty (\sin \alpha_p / \bar{r}')^2}{2(1/\lambda_\infty - \cos \alpha_p / \lambda_{\infty 0T})} \delta(\alpha_p) \quad (3.51)$$

$$\eta_P = 1 + \frac{\lambda_\infty (\sin \alpha_p / \bar{r}')^2}{2(1/\lambda_\infty - \cos \alpha_p / \lambda_{\infty 0P})} \delta(\alpha_p) \quad (3.52)$$

The numerator is proportional with λ_∞ , while the first term in the denominator reduces.

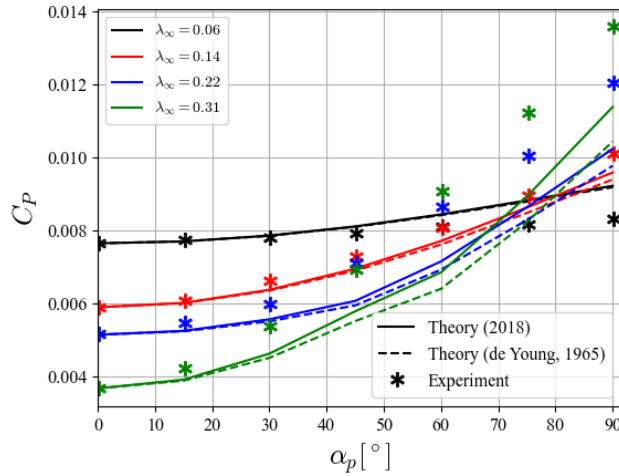


Figure 3.20: C_P of a small-scale rotor against incidence angle for various λ_∞

Thus the thrust and power correction factors increase faster with tip speed ratio than a linear function.

3.4.2 Validation of analytical model for off-axis efforts

The normal force coefficient for a small-scale propeller is presented in Fig. 3.21. The current model as indicated by solid lines is in good agreement with the experimental results. For small tip speed ratios, the model mostly resembles the behaviour of a sine function, with the largest value obtained at $\pi/2$. For higher tip speed ratios, the λ_∞ term becomes significant, and the normal force coefficient is larger than the $\sin \alpha_p$ correction. The dashed lines represent results from the previous theory from Ref. [DY65]. While both theories agree at low incidence angle, the $\tan \alpha_p$ correction in Ref. [DY65] overestimates normal force at high incidence and leads eventually to a singularity at 90° .

There exists a local maximum in normal force coefficient for each tip speed ratio. The analytical model isn't able to predict this peak, and the theoretical curve overshoots the experimental value after this local maximum.

In Fig. 3.22, the in-plane moment coefficients from the theoretical model and experimental measurement are plotted. The result demonstrated a good trend and agreement of current theory for small λ_∞ . The theory in Ref. [DY65] again overestimates the off-axis moment at high incidence.

For $\lambda_\infty \geq 0.32$, the theoretical value is overestimated. The difference is caused by the linear lift line assumption made at the blade sections. The outer section of the advancing blade is likely to stall at these tip speed ratios, and cannot sustain such a large in-plane moment. As a result, its $\lambda_{\infty_{OT}}$ is significantly larger, which reduces the influence of the λ_∞

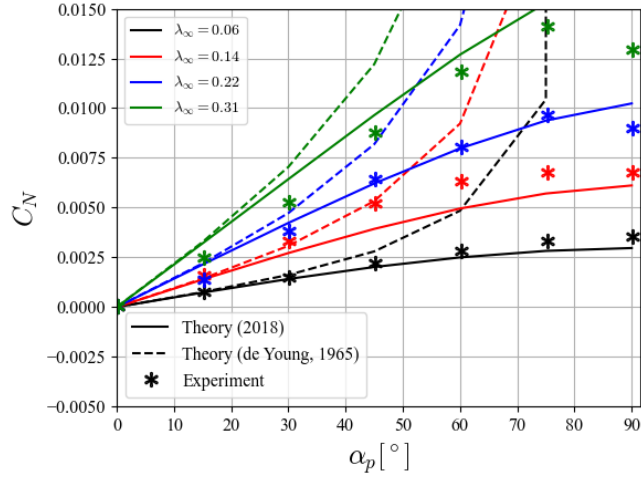


Figure 3.21: C_N of a small-scale rotor against incidence angle for various λ_∞

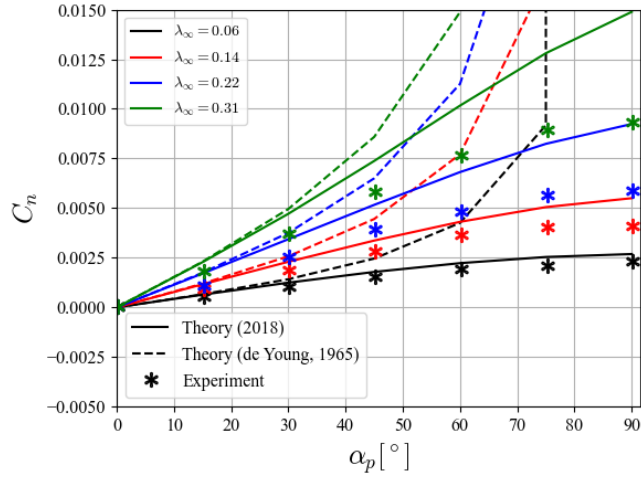


Figure 3.22: C_n of a small-scale rotor against incidence angle for various λ_∞

term in Eq. (3.44), indicating less severe blade stall.

Despite the discrepancies between theoretical and experimental results at large λ_∞ and/or high α_p , the model generally provides a reasonable estimation of propeller behaviours at off-design conditions for a fractional cost of higher-order methods.

3.4.3 Backflow condition

Between 90° and 180° rotor incidence, the prop rotor encounters backflow condition where the axial freestream component $V_{\infty A}$ originates from behind the rotor. This condition appears

rarely, if ever, to aircraft propeller during cruise flight, but it is a typical scenario for a helicopter main rotor in descent. Although the analytical model cannot treat rotor incidence angle higher than 90° , the proprotor was tested up to 180° with exception of $\lambda = 0.06$ to assess rotor performance in backflow condition.

Thrust and power coefficients are presented in Fig. 3.23 and Fig. 3.24 in a similar fashion as in the previous sections except that the abscissa extends up to $\alpha_p = 180^\circ$. Beyond 90° rotor incidence, the thrust and power coefficients continue to increase up to 120° . There appears to be different situations depending on the tip speed ratio. For $\lambda_\infty \leq 0.22$, C_T and C_P reach their maximal values and start to decrease when α_p approaches 180° . However, when at higher tip speed ratio ($\lambda_\infty = 0.31$), C_T and C_P continue to increase although at less steep gradient with respect to α_p . In this case, the maximal thrust and power are reached at pure descent.

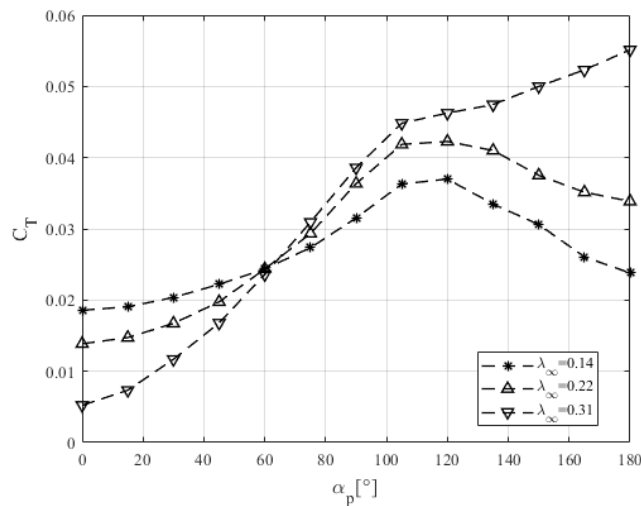


Figure 3.23: C_T of a small-scale rotor against incidence angle for various λ_∞

C_N and C_n are plotted in Fig. 3.25 and Fig. 3.26. As mentioned before, the maximal normal force and in-plane moment are reached slightly before or at $\alpha_p = 90^\circ$. Afterwards, a sharp reduction in both C_N and C_n are observed up to $\alpha_p = 120^\circ$. From the blade element analysis, the flow condition from freestream remains highly asymmetric in this incidence angle range, thus the reduction in off-axis efforts is most likely a consequence of either enlarged stall region or interference with tip vortices, which is a sign of vortex ring state.

Above 120° , the situation again depends on tip speed ratio λ_∞ . C_N and C_n from the two cases at smaller λ_∞ continue to decrease until a local extrema is obtained in the opposite direction, then return to zero in axial descent. C_N and C_n reduce monotonously to zero at the highest tip speed ratio.

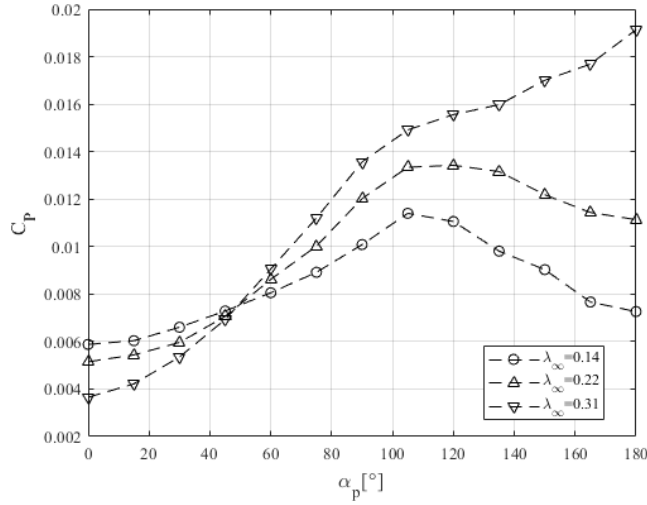


Figure 3.24: C_P of a small-scale rotor against incidence angle for various λ_∞

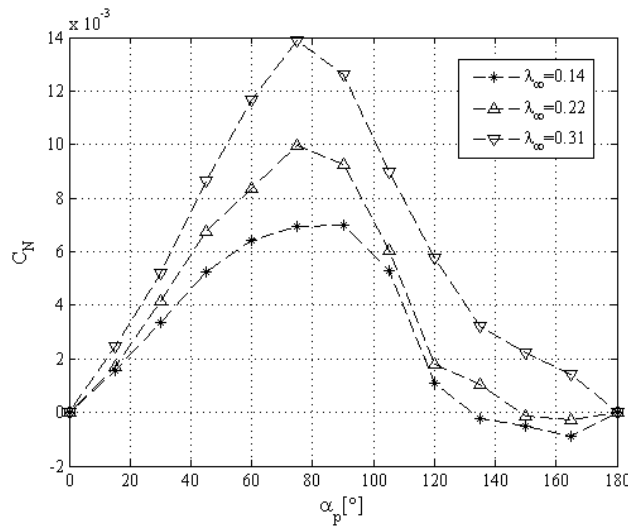


Figure 3.25: C_N of a small-scale rotor against incidence angle for various λ_∞

3.5 Conclusions

An analytical model was derived, benchmarked and validated to estimate proprotor thrust, power, normal force and in-plane moment at non-zero incidence angle. Assumptions typical for the transition flight phase were made to keep the model in closed and tractable form. Blade element theory and representative blade section analysis were used to include influences of proprotor geometry. In light of the studies available, the current model offers a computationally efficient tool over incidence angles between 0 to $\pi/2$. The model is suitable for preliminary design or potentially used as surrogate model for real-time applications.

The accuracy of the model was studied with both classical theories in specific α_p conditions

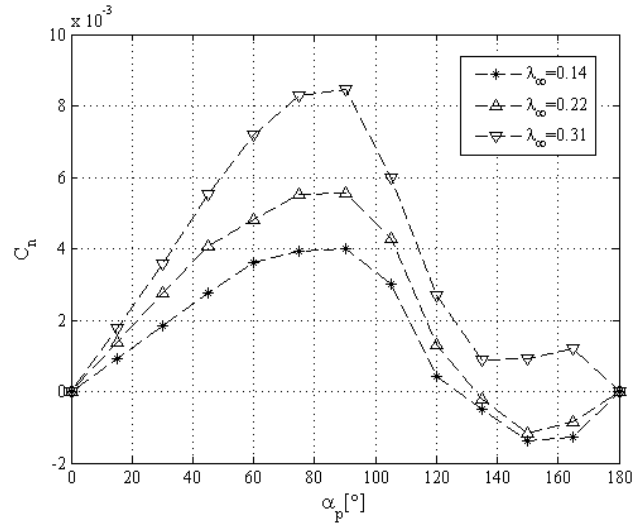


Figure 3.26: C_n of a small-scale rotor against incidence angle for various λ_∞

and experimental data over the full α_p range. Analysis confirms the model includes principle aerodynamic effects, including both induced and profile drag components. The agreement with test data within the transition flight phase is desirable. Limitation of the model exists for power estimation at or above rotor advance ratio $\mu = 0.08 \sim 0.11$, although such condition appears to be extreme for practical transition flight.

Although the current model is able to predict proprotor performance over a wide range of flight conditions, limitations still exist for certain flight regimes of interest. Backflow condition at moderate descent speed may require analysis for $\alpha_p > \pi/2$, as well as dynamic aerodynamic efforts encountered in gusty conditions or during rapid manoeuvres. Furthermore, geometry modifications such as swept angle of some low-noise proprotor designs may be studied.

Experimental Study on Propeller-Wing Aerodynamic Interactions

Contents

4.1 Introduction	54
4.2 Propeller wake development	55
4.2.1 Test set-up	56
4.2.2 Results	59
4.2.3 Analytical Model of Wake Displacement	63
4.2.4 Conclusion	74
4.3 Aerodynamic augmentation of closely-coupled propeller	74
4.3.1 Background	74
4.3.2 Present Work	75
4.4 Experiment Set-Up	76
4.4.1 Description of Apparatus	76
4.4.2 Test Conditions	80
4.5 Decomposition of Thrust-Augmented Aerodynamic Loads	81
4.5.1 Momentum theory	82
4.5.2 Augmented aerodynamic loads	83
4.6 Results and Discussions	86
4.6.1 Measurement of Aerodynamic Loads	86
4.6.2 Propeller wake effect on wing flap	87
4.6.3 Effect of propeller install angle	90
4.6.4 Effect of vertical displacement	92
4.7 Conclusion	93

Author's Contributions

Published Papers

- Y. Leng, M. Bronz, T. Jardin, J.-M. Moschetta, "Slipstream Deformation of a Propeller-Wing Combination Applied for Convertible UAVs in Hover Condition", *Unmanned System Journal*, septembre 2020.
- Y. Leng, T. Jardin, M. Bronz, J.-Marc Moschetta, "Experimental Analysis of a Blown-Wing Configuration during Transition Flight", *AIAA Paper 2020-1983, AIAA Applied Aerodynamics Conference, AIAA SciTech Forum*, Orlando, United States, Jan. 6-10, 2020.
- Y. Leng, M. Bronz, T. Jardin, J.-Marc Moschetta, "Slipstream Deformation of a Propeller-Wing Combination Applied for Convertible UAVs in Hover Condition", *11th International Micro Air Vehicle Competition and Conference*, Madrid, Spain, Oct. 1-4, 2019.
- Y. Leng, M. Bronz, T. Jardin, J.-Marc Moschetta, "Comparisons of Different Propeller Wake Models for a Propeller-Wing Combination", *8th European Conference for Aeronautics and AeroSpace Sciences*, Madrid, Spain, Jul. 1-4, 2019.

4.1 Introduction

Convertible aircraft - aircraft capable of vertical take-off and landing, has long attracted attention from aeronautical community due to its reduced field requirement as well as cruise efficiency comparable to a fixed-wing aircraft [McC94]. However, complicated systems required to improve transition flight characteristics and guarantee flight safety typically offset these advantages, and as a result regular commercial programme has yet been realised. The affordability of electrical propulsion in recent years has inspired VTOL programmes in unmanned aerial system development for surveillance, ground mapping or delivery, as well as in future autonomous aerial vehicle for urban transportation.

Relevant researches, such as MAVION developed at ISAE [Ita+11] or Cyclone from ENAC, have demonstrated operational advantages in its convenience of recovery. To fully exploit the potential of VTOL operations, the dynamics during transition flight between hover and cruise is critical [LDM14] for robust unmanned aerial system development. In this flight phase, the aircraft experiences unusual attitudes outside of a fixed-wing aircraft flight envelope [McC94]. Fig. ?? represents a tailsitter configuration, which eventually reaches 90° angle of attack at near hover conditions.

At these conditions, equilibrium is typically achieved through a combination of high propeller thrust and special high-lift aerodynamic designs such as externally or internally blown

flap. High speed flow accelerated by the propulsor (a propeller for example) is blown onto a lifting surface and thus maintains sufficient aerodynamic load for lift augmentation and/or flight control. An external blown flap is also simpler as no internal bleed routing is required.

4.2 Propeller wake development

During preliminary design, reduced-order models such as panel method, vortex lattice method, to name a few, are preferred thanks to their capability of analysing large amount of candidate configurations at a relatively small computational cost [Vel04]. Veldhuis et al. has identified two approaches in analysing propeller-wing systems : single approach and dual-coupling approach.

In single analysis mode, only the influence of propeller slipstream is taken into consideration. When calculating wing lift for sections immersed in propeller slipstream, the accelerated freestream velocity and sometimes the circumferential swirl velocity are applied to calculate local angle of attack and dynamic pressure. The velocities in the slipstream are computed from a free propeller model, such as one based on blade element momentum theory.

To improve accuracy, dual-coupling mode is sometimes used. The same calculation on wing sections still applies. A main difference is that the freestream condition of the propeller is also modified after the wing circulation distribution is solved, and induced velocity from the lifting surfaces is added to flight speed for propeller calculation. Ideally, an iterative approach is used until both solutions converge.

Both analysis modes require an empirical coefficient to attenuate propeller induced velocity before application in wing calculation [AKDS14]; [Epe17]. This suggests that propeller induced velocity distribution might have changed due to the presence of the wing. The effect was treated semi-empirically [AKDS14], but a clear physical understanding is still absent.

Recent studies on tractor propeller wake measurements have found that the influence of the wing on the propeller isn't limited to the flow upstream of the rotor disk. Deters et al [DAS15] have used a seven-hole probe to make wake survey at different downstream locations after three different propellers. A flat plate wing is situated close to the propeller. The presence of the wing is significant that the upper and lower halves of the slipstream were observed to be offset in opposite directions by a distance up to 1 propeller radius at survey plane. The phenomenon was first observed and analysed by Witkowski et.al [WLS89]. However neither studies provided quantitative analysis.

In this study, a wake survey in static condition is presented at different rotation speeds and flap deflection angles. The test equipment and condition will be introduced in Section 4.2.1. Results and quantitative analysis will be shown in Section 4.2.2. The test was also performed with flap deflection to investigate the slipstream development when the wing was generating lift.

In Section 4.2.3, an analytical model based on potential flow analysis was developed to

estimate the deformation of propeller slipstream.

4.2.1 Test set-up

4.2.1.1 Test equipments

The test was conducted in the indoor flight arena at Ecole National de l'Aviation Civile (ENAC). The flight arena's volume provides static ambient environment for simulating hover condition.

The test equipments were divided into three subsystems : 1) propeller-wing combination and their relevant motion control system ; 2) 5-hole probe and its data acquisition system ; 3) motion control system for 5-hole probe. The test setup is shown in Fig. 4.1.

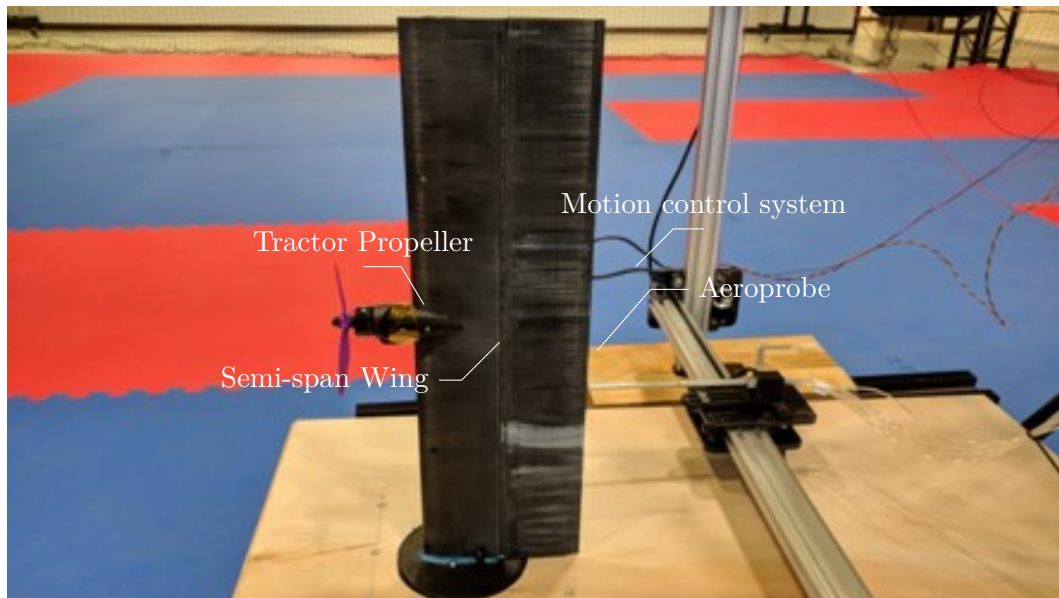


Figure 4.1: Test set-up in ENAC indoor flight arena

The wing tested was a semi-span model with 500mm span. The straight wing had a constant chord length of 150mm and NACA0012 aerofoil section. A propeller nacelle was situated at 55mm from plane of symmetry, where a CM2206 direct current brushless motor was enclosed. A full-span plain flap was installed for the last 50% chord, and a servo allowed symmetrical flap deflection of 15° in either direction.

An APC 3-blade 5x4.6E propeller was tested. A tilt-rotor mechanism was designed to allow propeller install angle to change between -10° to 10° with respect to wing chord line. The tilt mechanism was fixed at 0° for this experiment.

The wake survey was conducted with an Aeroprobe 5-hole probe. The centre of the probe head was located 15mm behind the trailing edge or 1.7 times propeller diameters downstream

of rotor plane.

At the centre sphere, five holes were arranged in a cross pattern with one in the centre, a pair in vertical plane and another pair perpendicularly arranged. A series of static ports were situated after the probe head. When air is blown, the velocity, pitch and yaw attitude of probe will produce pressure difference between centre hole and static ports, vertical pair and side pair holes.

Honeywell analogue differential pressure sensors were used to measure the three pairs of pressure differences which were needed to resolve flow velocity. A calibration method proposed by Reichert et al [RWS94] were used to take into consideration cross-product terms and to correct alignment errors.

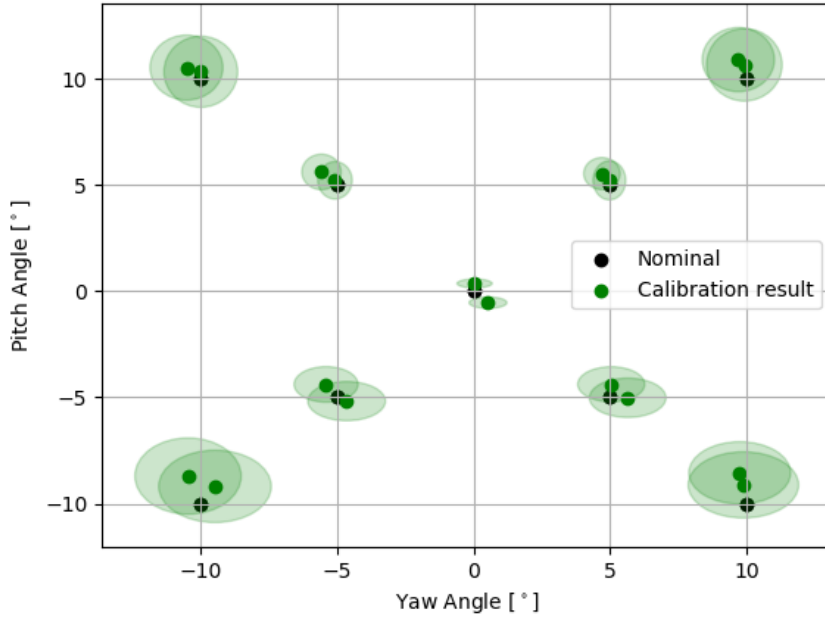


Figure 4.2: Flow angle measurement

The calibration was also analysed for measurement error. An uncertainty analysis was performed similar to the one described by Reichert et al, and fitting error as well as pressure fluctuations were considered in uncertainty propagation. A validation test was performed in a wind tunnel with known wind velocity and probe attitude. Flow angle measurement and its uncertainty is plotted in Fig. 4.2; flow speed measurement and its uncertainty is plotted in Fig. 4.3.

From the validation case, uncertainty in flow speed was estimated at $\pm 0.3m/s$ and error in flow angle was estimated to be less than 2° below 20° .

A 2-axis linear motion frame was constructed to allow automatic wake survey at a given

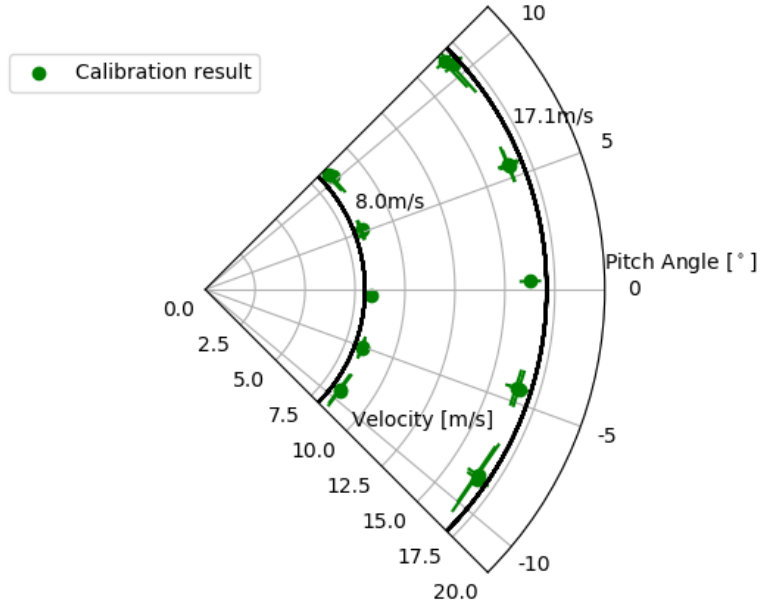


Figure 4.3: Flow speed measurement

plane perpendicular to propeller axis. Three stepper motors controlled by I2C bus were used to move a cart on which the 5-hole probe was mounted within the survey plane. The measurement was made on a 15×15 grid using alternating survey pattern as depicted in Fig. 4.4. Mean velocity data were obtained from sample recorded at $700Hz$ over a period of $5s$.

4.2.1.2 Test conditions

All tests were conducted at $V_\infty = 0$ to analyse flow condition at hover flight. Different propeller rotation speed and flap angle were tested, and the test matrix is given in Table 4.1.

Test Variables	
Rotation Speed [<i>rpm</i>]	5770 / 8000 / 10000
Flap Deflection [°]	0, ± 15

Table 4.1: Slipstream Deformation Testing Conditions

The rotation of the propeller in front of a finite wing made the situation no longer symmetrical. Since lift must vanish at wing tip, spanwise lift distribution isn't uniform for a finite wing without propeller. Furthermore, an up-going propeller blade influences the wing section behind in a different way from the down-going blade, hence the influence of a single rotating propeller isn't symmetrical. For this reason, both positive and negative flap deflections were tested.

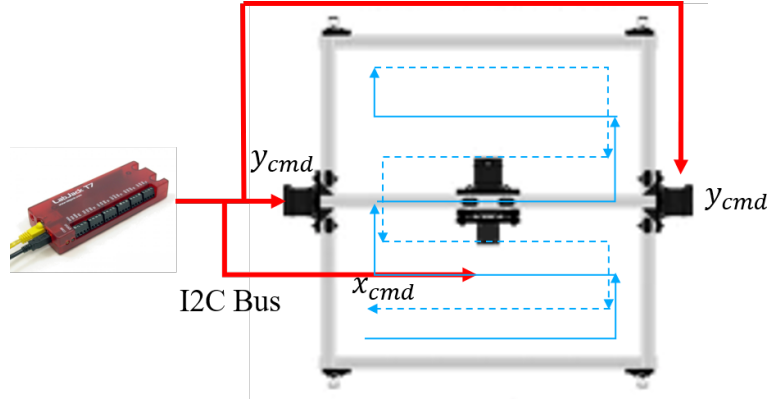


Figure 4.4: Motion control system and survey pattern

4.2.2 Results

In this section the results of 0° flap deflection will first be presented in subsection 4.2.2.1, where the effect of rotation speed as well as the general flow structure of propeller-wing interference will be discussed. Further discussion will continue in subsection 4.2.2.2 on the effect of flap deflection.

4.2.2.1 0° Flap Deflection

The configuration at neutral flap setting excluded the effect of different velocity and pressure profiles on the extrados and intrados. The wake survey therefore was only influenced by the fact that propeller slipstream was separated by a solid surface.

The wake survey at $8000rpm$ is presented in Fig. 4.5. The velocity field distribution in the survey plane is depicted as two components : the streamwise component u is perpendicular to the survey plane and the transverse component $V_t = \sqrt{v^2 + w^2}$ is situated within the survey plane. In Fig. 4.5, the background contour shows u distribution while the transverse V_t is superposed by arrow symbols that give both magnitude and direction of V_t at sample points.

Above and below the wing, propeller slipstream can be identified as a semi-circular region of high energy airflow. Within the slipstream, both u and V_t are noticeably higher in magnitude than the surrounding flow region. The increase in axial velocity is expected as the propeller produces forward thrust by accelerating air in downstream direction. The transverse velocity is caused by the air resistance against blade rotation. Transverse induced velocity thus results from viscous effect, and is commonly referred to as swirl in rotary wing terminology.

According to momentum theory [Lei06], the induced axial velocity at propeller disk can be related to thrust coefficient:

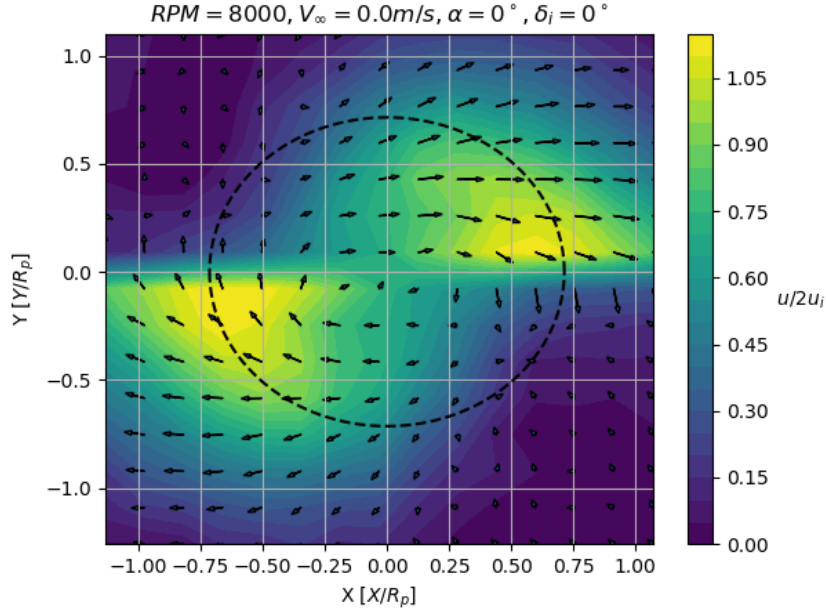


Figure 4.5: Velocity distribution at survey plane for symmetrical configuration at 8000rpm

$$u_i = nD \sqrt{\frac{2C_T}{\pi}}. \quad (4.1)$$

where n is rotation speed in revolution per second and D is propeller diameter. Thrust coefficient is defined as $C_T = \frac{T}{\rho n^2 D^4}$, and was obtained as tabulated data from propeller manufacturer at different rotation speeds [Apc]. After the rotor plane, contraction of slipstream accelerates flow towards twice of u_i at downstream infinity. The flow survey is non-dimensionalised using the induced axial velocity at ultimate wake. The benefit of such normalisation is to remove the effects of thrust loading and rotational speed.

A circle in dashed line represents the undisturbed slipstream boundary obtained from vortex theory from McCormick [McC94], where

$$R(\bar{z}) = R_p \sqrt{1 + \bar{z}^2 - \bar{z} \sqrt{1 + \bar{z}^2}}. \quad (4.2)$$

where \bar{z} is the distance from rotor disk plane normalized by propeller radius R_p and \bar{z} is negative downstream. Through comparison with the actual high-speed regions, a distinct separation of flow structures between the extrados and intrados can be observed.

While increases in u_i and V_t can be reasonably explained by free propeller theory, movement of the two slipstream regions can't be similarly explained. For a single propeller, the slipstream will stay together as in an approximate cylindrical shape. But when a wing is present, as seen in Fig. 4.5, the upper slipstream exhibited a general displacement towards

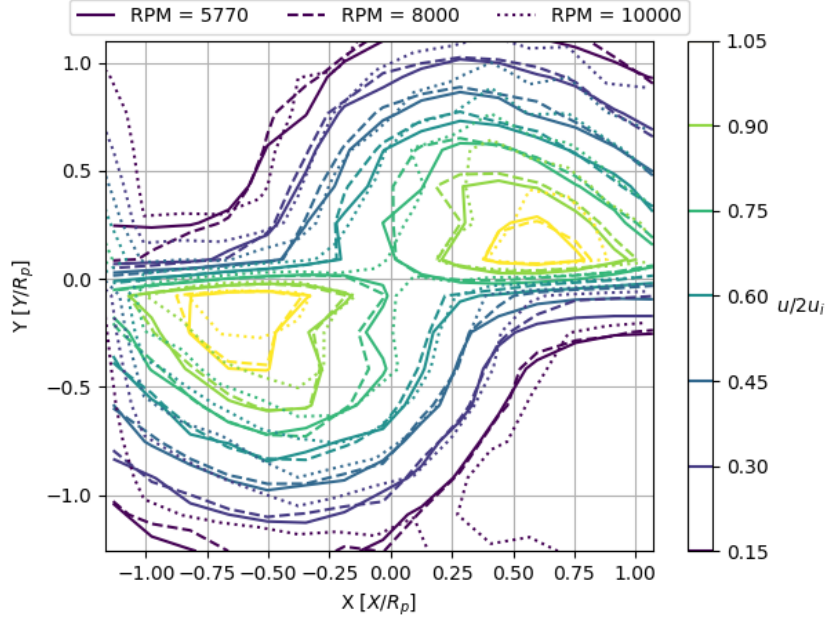


Figure 4.6: Comparison of axial velocity distribution at different rotation speeds

the right (outboard) while the lower slipstream region moves oppositely towards the left (inboard). The directions of movement is associated with the direction of propeller, where in the test case, the inboard blade was turning upward relative to the wing chord.

Axial velocity contours of cases from three different rotation speeds are plotted in Fig. 4.6, where the solid line depicts u distribution at $5770rpm$, dashed line represents the one at $8000rpm$ and dotted line is for $10000rpm$.

Plotted in non-dimensional form, the contour lines of three different cases generally overlap for most flow region. Major differences lie close to the axial velocity peaks at intrados and extrados. The general agreement of flow topology suggests that at hover condition, the wake development is scalable with thrust loading and blade rotation.

4.2.2.2 Effect of Flap Deflection

In subsection 4.2.2.1 the slipstream development in 0° flap deflection configuration was presented and analysed. In this condition the wing wasn't lifting, and thus the transverse slipstream displacement was purely caused by the presence of solid surface between the extrados and intrados parts of slipstream.

Results obtained at $8000rpm$ are included and discussed in this section, while the other results are included in appendix. A for simplicity. The effects discussed in this section are similar at a different tested rotation speed.

Figure 4.7 demonstrated the wake survey in a similar fashion as in Fig. 4.5. The dashed line represents the flap trailing edge location when deflected. High speed region can still be observed in the velocity field, but the distribution took a different shape because of the deflection of flap. Besides the transverse displacement in left and right directions, the slipstream profiles also differ from each other in their vertical expansion. On the extrados, the slipstream was displaced towards the right and took a slightly narrower width. While the highest point of extrados slipstream stayed close to 1 propeller radius, the region spread lower and generally followed the deflected trailing edge flap. The extended vertical expansion is consistent with the reduced lateral width, since flow continuity must be satisfied.

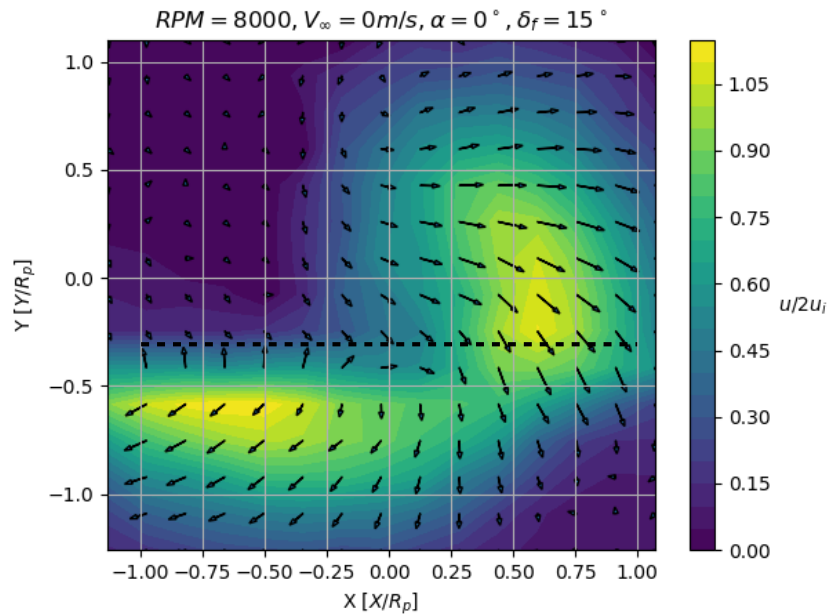


Figure 4.7: Velocity distribution at survey plane for with 15° flap deflection at 8000rpm

The intrados slipstream was wider and flatter compared to the extrados slipstream and Fig. 4.5. The combined effect produced a distinct velocity difference for the wing section after up-going blade (inboard section), while such difference was more subtle on the other side. The non-uniform velocity distribution could imply significant local lift variation in the surveyed section.

Wake survey for negative flap deflection is depicted in Fig. 4.8. The velocity distribution is generally axial symmetric of Fig. 4.7. However the vertical extent of the intrados slipstream is slightly larger than the extrados slipstream in positive flap deflection. In Fig. 4.8, the wake boundary of intrados slipstream is shown lower than 1 propeller radius.

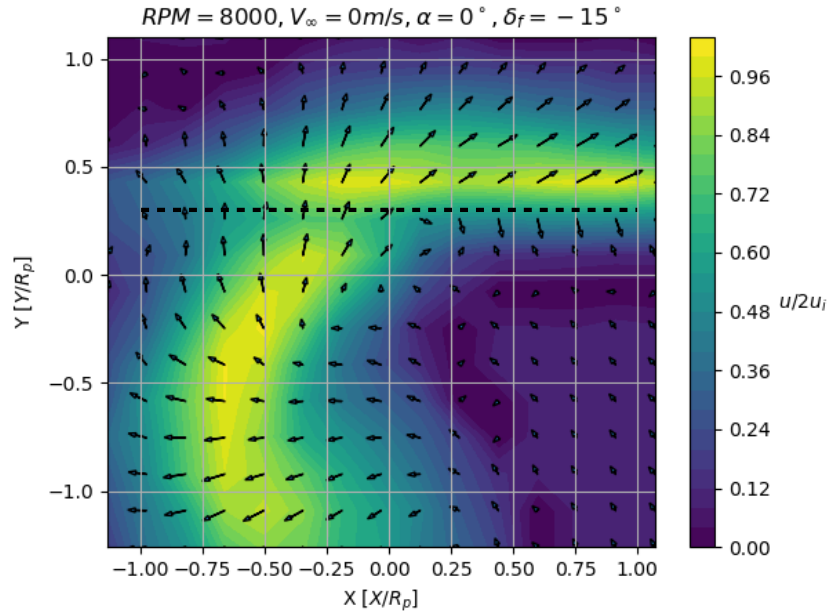


Figure 4.8: Velocity distribution at survey plane for with -15° flap deflection at $8000rpm$

4.2.3 Analytical Model of Wake Displacement

From flow survey behind propeller-wing combinations in section 4.2.2, it has been observed that when separated by the wing, two halves of propeller slipstream were subjected to opposite transverse motions, or "transverse slipstream displacement".

The phenomenon was explained by Witkowski et al [WLS89] using a method of images. They have qualitatively demonstrated that a pair of streamwise vortices mirrored by the wing surface will induce the correct trend of fluid motion. However no quantitative results were given as the effect on a propeller-wing combination at high speed condition was estimated to be small.

However such phenomenon is significant at low-speed regime, observed in section 4.2.2. From the comparisons with two recently developed reduced-order models, the phenomenon hasn't been included in performance estimation of propeller-wing combinations.

To include the transverse displacement in a potential model isn't trivial. Consider the deformed slipstream system in Fig. 4.9 where a series of vortex rings symbolise the blade tip vortices shed from one propeller blade. The vortex line is displaced in corresponding directions upon contact with the wing.

This simple model shows the discontinuity between upper and lower halves of the helical vortex and their respective translations. Such model isn't admissible in potential flow meth-

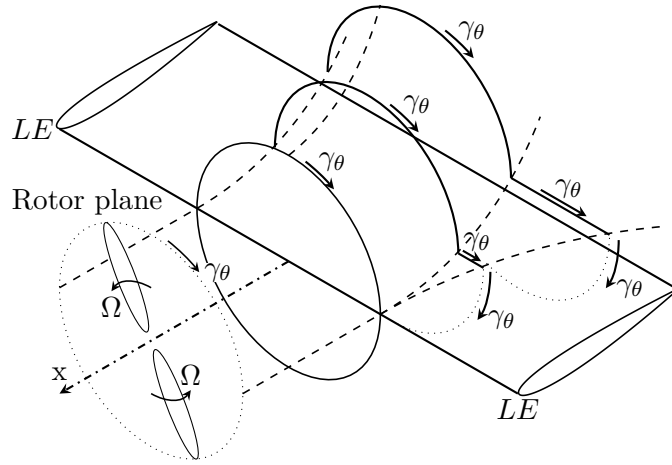


Figure 4.9: Displaced propeller slipstream and connecting line vortex segments

ods. A line vortex is needed to reconnect the ends of upper and lower vortex semi-rings. The addition of the line vortex segment is significant in three ways :

First, it completes the vortex system so that Helmholtz theorem is again respected. The solution is thus admissible in potential methods.

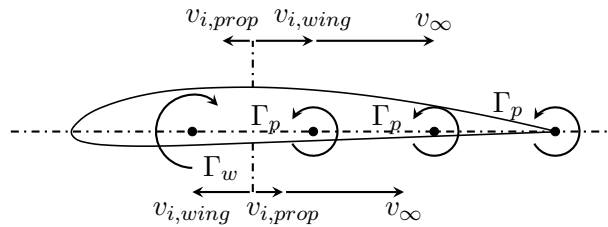


Figure 4.10: Side view of an aerofoil section after up-going propeller blade

Second, the circulation has physical meaning of streamwise velocity difference between the upper and lower surface. In Fig. 4.10, an aerofoil section after up-going blade is shown. According to Fig. 4.9, at the upper surface, the aerofoil section is situated outside of the propeller slipstream and thus experiences a smaller velocity component in streamwise direction. At lower surface the streamwise component is however augmented because of the induced velocity within propeller slipstream. The velocity difference means additional circulation exists around the aerofoil section.

Third, the direction of the vortex segment has the effect of attenuating the overestimation of propeller-wing interaction. The up-going blade induces increased local angle-of-attack and thus wing circulation Γ_w is enhanced. However from the previous discussion on Fig. 4.10, the bound line vortex segments add an opposing circulation, and hence mitigate the effect of increasing Γ_w .

To correctly place the bound vortex segments so that they affect the corresponding wing sections, an estimation of the transverse slipstream displacement is needed. The next sections present a qualitative estimation of centreline deformation for a propeller slipstream on a flat plate.

4.2.3.1 Imaginary Distributed Slipstream Vortex Field

When the wing is present, the normal velocity at the lifting surface must vanish. This non-penetration condition can be satisfied by reversing the direction of axial and radial distributed vortex elements. The imaginary system is given in Eqs. (4.4) - (4.6), and illustrated in Fig. 4.11. In Eqs. (4.4)- (4.6), angle ϕ refers to wake helix angle, which is the angle between the tangent of shed tip vortex centreline and the propeller rotor plane. Here the slipstream contraction is neglected.

$$\vec{\gamma} = (\gamma_r, \gamma_\theta, \gamma_x), \text{ where} \quad (4.3)$$

$$\gamma_r = \begin{cases} -\frac{\Gamma_0}{2\pi r} & r \leq R_p, 0 < \theta < \pi, x = 0 \\ \frac{\Gamma_0}{2\pi r} & r \leq R_p, \pi < \theta < 2\pi, x = 0 \\ 0 & \text{otherwise} \end{cases}, \quad (4.4)$$

$$\gamma_\theta = \begin{cases} -\frac{\Gamma_0 \cos \phi}{2\pi R_p} & r = R_p, x < 0 \\ 0 & \text{otherwise} \end{cases}, \quad (4.5)$$

$$\gamma_x = \begin{cases} \frac{\Gamma_0 \sin \phi}{2\pi R_p} & r = R_p, 0 < \theta < \pi, x < 0 \\ -\frac{\Gamma_0 \sin \phi}{2\pi R_p} & r = R_p, \pi < \theta < 2\pi, x < 0 \\ 0 & \text{otherwise} \end{cases}. \quad (4.6)$$

Notice that circumferential distributed vortices don't change sign, so that Helmholtz theorem at the surface is satisfied. Non-penetration condition is still assured as the circumferential component doesn't induce normal velocity at the surface. The upper half of imaginary distributed vortex system represents the upper propeller slipstream with wing leading edge situated exactly at rotor plane.

It is apparent that the axial induced velocity along centreline doesn't change in the imaginary distributed vortex system. Furthermore, it will be assumed that the induced velocity doesn't vary much around centreline, such that the centreline value could be used to trace

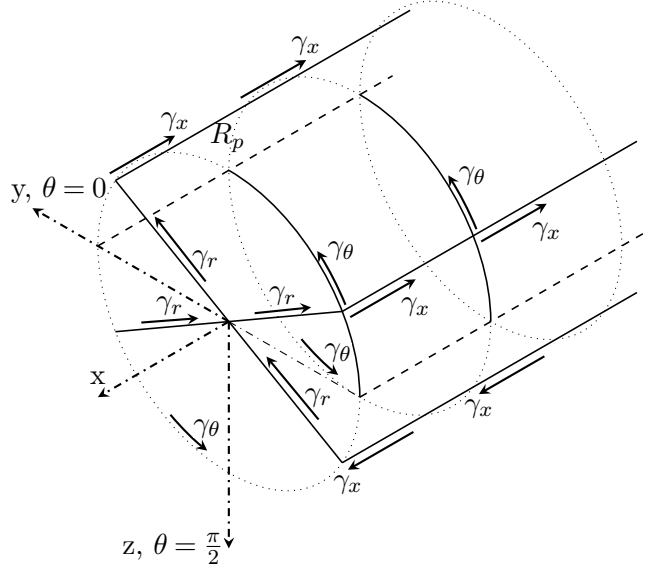


Figure 4.11: Imaginary propeller distributed vortex system

the deformed trajectory. During the process, slipstream boundary will remain as a straight semi-infinite cylinder. The problem then reduces into solving centreline transverse induced velocity v_{iy} .

Velocity v_{iy} comes from two parts : a first part induced by rotor plane vortex $v_{iy\gamma_r}$; and a second part from axial vortices in trailing wake $v_{iy\gamma_x}$.

4.2.3.2 Rotor plane induced transverse velocity $v_{iy\gamma_r}$

At rotor plane where $r \leq R_p, x = 0$, an elementary vortex segment is expressed in Eq. (4.7):

$$\begin{aligned}
 d\vec{\Gamma}_r &= \gamma_r r d\theta dr \hat{i}_r \\
 &= \mp \frac{\Gamma_0}{2\pi} d\theta dr \hat{i}_r \\
 &= \mp \frac{\Gamma_0}{2\pi} d\theta dr (\cos\theta \hat{i} + \sin\theta \hat{j}).
 \end{aligned} \tag{4.7}$$

where the expression takes negative sign above the surface ($0 < \theta < \pi$). Because of symmetry, the contribution from vortex elements above the surface is identical as that from below. Thus the induced velocity from upper vortex elements is doubled to obtain the full component.

Relative position vector from an arbitrary downstream position A is given in Eq. (4.8) :

$$\vec{r}_{\Gamma_r A} = r (\cos\theta \hat{i} + \sin\theta \hat{j}) - R_p \bar{x}_A \hat{k}. \tag{4.8}$$

where \bar{x} is x coordinate normalised by propeller radius. Differential transverse induced velocity is obtained from Biot-Savart law:

$$\begin{aligned} dv_{ix_{\gamma r}}(\bar{x}_A) &= \frac{\left(\vec{r}_{\Gamma r A} \times \vec{\Gamma}_r\right)_y}{4\pi r_{\Gamma r A}^{3/2}} \\ &= -\frac{\Gamma_0 \bar{x}_A}{8\pi^2 R_p} \frac{\sin \theta d\theta dr}{(\bar{r}^2 + \bar{x}_A^2)^{3/2}} \end{aligned} \quad (4.9)$$

Integrate on the upper half rotor plane and double the result, the transverse induced velocity from rotor plane vortex distribution is obtained:

$$\begin{aligned} v_{iy_{\gamma r}}(\bar{x}_A) &= -\frac{\Gamma_0 \bar{x}_A}{4\pi^2 R_p} \int_0^1 \int_{\pi}^{2\pi} \frac{\sin \theta d\theta d\bar{r}}{(\bar{r}^2 + \bar{x}_A^2)^{3/2}} \\ &= -\frac{\Gamma_0 \bar{x}_A}{2\pi^2 R_p} \int_0^1 \frac{d\bar{r}}{(\bar{r}^2 + \bar{x}_A^2)^{3/2}} \\ &= -\frac{\Gamma_0}{2\pi^2 R_p} \frac{1}{\bar{x}_A \zeta_A} \end{aligned} \quad (4.10)$$

where parameter $\zeta_A = \zeta(\bar{x}_A) = \sqrt{1 + \bar{x}_A^2}$

4.2.3.3 Trailing wake induced transverse velocity $v_{iy_{\gamma x}}$

At wake boundary where $r = R_p, x < 0$, streamwise elementary vortex segment is expressed in Eq. (4.11):

$$d\vec{\Gamma}_x = \gamma_x R_p^2 d\theta d\hat{x} \hat{i}_x = \pm \frac{\Gamma_0 R_p \sin \phi}{2\pi} d\theta d\hat{x} \hat{k}. \quad (4.11)$$

where the expression takes negative sign above the surface ($\pi < \theta < 2\pi$). Similar to the situation with rotor plane induced velocity, the result from upper vortex elements is doubled to obtain full component of transverse induced velocity.

Relative position vector from an arbitrary downstream position A is given in Eq. (4.12):

$$\vec{r}_{\Gamma x A} = R_p \left[\cos \theta \hat{i} + \sin \theta \hat{j} + \Delta_A \hat{k} \right]. \quad (4.12)$$

where $\Delta_A = \Delta(\bar{x}_A) = \bar{x} - \bar{x}_A$

Differential transverse induced velocity is obtained from Biot-Savart law:

$$\begin{aligned}
dv_{ix\gamma_x}(\bar{x}_A) &= \frac{\left(\vec{r}_{\Gamma_{xA}} \times \vec{\Gamma}_x\right)_y}{4\pi r_{\Gamma_{xA}}^{3/2}} \\
&= \frac{\Gamma_0 \sin \phi}{8\pi^2 R_p} \frac{\sin \theta d\theta d\bar{x}}{(1 + \Delta_A^2)^{3/2}}.
\end{aligned} \tag{4.13}$$

Integrate on the upper semi-infinite cylinder and double the result, the transverse induced velocity from trailing wake vortex distribution is obtained:

$$\begin{aligned}
v_{iy\gamma_x}(\bar{x}_A) &= \frac{\Gamma_0 \sin \phi}{2\pi^2 R_p} \int_{-\infty}^0 (1 + \Delta_A^2)^{-3/2} d\bar{x} \\
&= \frac{\Gamma_0 \sin \phi}{2\pi^2 R_p} \left(1 - \frac{\bar{x}_A}{\zeta_A}\right).
\end{aligned} \tag{4.14}$$

Finally the centreline transverse induced velocity can be obtained by combining Eqs. (4.10) and (4.14):

$$v_{iy}(\bar{x}_A) = \frac{\Gamma_0}{2\pi^2 R_p} \left[\left(1 - \frac{\bar{x}_A}{\zeta_A}\right) \sin \phi - \frac{1}{\bar{x}\zeta_A} \right]. \tag{4.15}$$

4.2.3.4 Deformed Centreline Equation

To obtain an analytical approximation of centreline equation, axial induced velocity v_{ia} obtained from vortex system is needed. It is calculated in a similar way, and a detailed derivation can also be found in McCormick [McC94]. For brevity, the expression is given in Eq. (4.16):

$$v_{ia}(\bar{x}) = -\frac{\Gamma_0 \cos \phi}{4\pi R_p} \left(1 - \frac{\bar{x}}{\zeta}\right). \tag{4.16}$$

With Eqs. (4.15) and (4.16), the deformed centreline can be expressed by considering it to be a surface streamline, where

$$\frac{d\bar{y}}{v_y(\bar{x})} = \frac{d\bar{x}}{v_x(\bar{x})}. \tag{4.17}$$

Local transverse velocity v_y and axial velocity v_x is given in Eq. (4.18):

$$\begin{aligned}
v_y(\bar{x}) &= v_{iy}(\bar{x}) \\
v_x(\bar{x}) &= -V_\infty + v_{ia}(\bar{x}).
\end{aligned} \tag{4.18}$$

The negative sign in front of V_∞ is because positive x is defined to be opposite direction of freestream. Local deflection angle is given in Eq. (4.19):

$$\theta(\bar{x}) = \frac{v_{iy}(\bar{x})}{-V_\infty + v_{ia}(\bar{x})}. \tag{4.19}$$

Thus the deformed centreline Eq. (4.20) can be approximated by integrating Eq. (4.17):

$$\bar{y}(\bar{x}) = \begin{cases} 0 & \bar{x}_{LE} \leq \bar{x} \\ \int_{\bar{x}_{LE}}^{\bar{x}} \theta(s) ds & \bar{x}_{TE} \leq \bar{x} < \bar{x}_{LE} . \\ \bar{y}_{TE} + \theta_{TE} \Delta_{TE} & \bar{x} < \bar{x}_{TE} \end{cases} \tag{4.20}$$

Equation (4.20) contains two parts : the first term represents the deformation on top of the wing starting from non-dimensional leading edge \bar{x}_{LE} until trailing edge \bar{x}_{TE} ; the second term assumes constant centreline deviation angle from rotation axis after trailing edge, and thus the transverse displacement is linear with downstream location \bar{x} .

The analytical expression of deformed centreline equation will be presented in two parts : the first part is for static case where $V_\infty = 0$ and the second part is for cases where $V_\infty > 0$

When $V_\infty = 0$ and $\bar{x} < \bar{x}_{TE}$, Eq. (4.20) simplifies to Eq. 4.21:

$$\begin{aligned}
\bar{y}(\bar{x}) &= - \int_{\bar{x}_{LE}}^{\bar{x}_{TE}} \theta(s) ds + \theta_{TE} \Delta_{TE} \\
&= - \frac{2}{\pi} \sec \phi [\sin \phi \Delta_{TE} \\
&\quad - \frac{\Delta_{TE}}{\bar{x}_{TE} (\zeta_{TE} - \bar{x}_{TE})} - \int_{\bar{x}_{LE}}^{\bar{x}_{TE}} \frac{ds}{s(\zeta - s)}] .
\end{aligned} \tag{4.21}$$

Before proceeding further, it is worth mentioning that the different factors affecting centreline deformation can be clearly observed in Eq. (4.21). The first term includes all contribution from streamwise vortices in the trailing wake, and it is a linear term in streamwise coordinate with proportional constant determined by helix angle. The second term represents the influence from blade circulation. This term grows with the proximity from leading edge to rotor plane. It is interesting to conclude that for a given geometry (\bar{x}_{LE} and \bar{x}_{TE}) in static condition, the deformed centreline shape only depends on wake helix angle ϕ .

Solving the integral and also consider all $\bar{x} < 0$, the complete static deformed centreline equation is given in Eq. (4.22), where \bar{c} is chord length normalised by propeller radius.

$$\bar{y}(\bar{x}) = \begin{cases} 0, & \bar{x}_{LE} \leq \bar{x} \\ \frac{2}{\pi} (\sec \phi - \tan \phi) \Delta_{LE} & \bar{x}_{TE} \leq \bar{x}, \\ + \frac{2}{\pi} \sec \phi \left(\zeta - \zeta_{LE} \right. & \bar{x} < \bar{x}_{LE} \\ \quad \left. + \ln \left| \frac{\bar{x}_{LE}}{\bar{x}} \frac{1 - \zeta}{1 - \zeta_{LE}} \right| \right) \\ \frac{2}{\pi} (\sec \phi - \tan \phi) \bar{c}_{TE} & \\ + \frac{2}{\pi} \sec \phi \left(\zeta_{TE} - \zeta_{LE} \right. & \bar{x} < \bar{x}_{TE} \\ \quad \left. + \ln \left| \frac{\bar{x}_{LE}}{\bar{x}_{TE}} \frac{1 - \zeta_{TE}}{1 - \zeta_{LE}} \right| \right) \\ - \frac{2}{\pi} \sec \phi \left[\sin \phi \Delta_{LE} \right. \\ \quad \left. - \frac{\Delta_{TE}}{\bar{x}_{TE} (\zeta_{TE} - \bar{x}_{TE}^2)} \right] \end{cases} \quad (4.22)$$

When $V_\infty > 0$, the slipstream will be convected in streamwise direction, which tends to attenuate centreline deformation. From Eq. (4.20), the integral term is expanded:

$$\begin{aligned} I(\bar{x}) &= \int_{\bar{x}_{LE}}^{\bar{x}} \theta(s) ds \\ &= -\frac{2}{\pi} \int_{\bar{x}_{LE}}^{\bar{x}} \frac{\tan \phi - \frac{\sec \phi}{s(\zeta - s)}}{1 + \frac{\zeta \sec \phi}{\Gamma_0(\zeta - s)}} ds, \end{aligned} \quad (4.23)$$

where the non-dimensional circulation $\bar{\Gamma}_0 = \frac{\Gamma_0}{4\pi V_\infty R_p}$. Since Γ_0 is associated with the total propeller thrust, the centreline deformation in forward flight condition is determined by both disk loading and total thrust condition. The relations between propeller thrusting condition and slipstream parameters ϕ , $\bar{\Gamma}_0$ are related from vortex theory [McC94], and demonstrated in appendix. B.

$$\tan \phi = -\frac{V_\infty + v_{ia}}{\Omega R_p} = \frac{1}{2\pi} \left(\sqrt{\frac{8C_T}{\pi} + J^2} - J \right) \quad (4.24)$$

Complete the integrations of $\tan\phi$ and $\sec\phi$ terms:

$$\begin{aligned}
I(\bar{x}) = & -\frac{2\bar{\Gamma}_0 \sin\phi}{\pi(2a-1)} [\Delta_{LE} - \zeta + \zeta_{LE}] \\
& -\frac{2(\bar{\Gamma}_0 \cos\phi)^2}{\pi\sqrt{2a-1}} \left(\frac{\tan\phi}{2a-1} - \frac{\sec\phi}{a} \right) [\psi(\bar{x}) - \psi_{LE} \\
& + \xi(\bar{x}) - \xi_{LE}] \\
& + \frac{\bar{\Gamma}_0}{\pi a} \ln \left| \frac{\zeta-1}{\zeta+1} \frac{\zeta_{LE}+1}{\zeta_{LE}-1} \right|, \tag{4.25}
\end{aligned}$$

where $a = 1 + \bar{\Gamma}_0 \cos\phi$, $\psi(\bar{x}) = \tan^{-1} \frac{\bar{x}\sqrt{2a-1}}{a}$, and $\xi(\bar{x}) = \tan^{-1} \frac{\sqrt{(2a-1)(1+\bar{x}^2)}}{a-1}$.

The complete deformed centreline equation in forward flight condition is in Eq. (4.26).

$$\bar{y}(\bar{x}) = \begin{cases} 0, & \bar{x}_{LE} \leq \bar{x} \\ -\frac{2\bar{\Gamma}_0}{\pi} \left\{ \frac{\sin\phi}{2a-1} [\Delta_{LE} - \zeta + \zeta_{LE}] \right. \\ \quad + \frac{\bar{\Gamma}_0 \cos\phi}{\sqrt{2a-1}} \left(\frac{\sin\phi}{2a-1} - \frac{1}{a} \right) & \bar{x}_{TE} \leq \bar{x}, \\ \quad \times [\psi(\bar{x}) + \xi(\bar{x}) - \psi_{LE} - \xi_{LE}] & \bar{x} \leq \bar{x}_{LE} \\ \quad \left. - \frac{1}{2a} \ln \left| \frac{\zeta-1}{\zeta+1} \frac{\zeta_{LE}+1}{\zeta_{LE}-1} \right| \right\}, \\ -\frac{2\bar{\Gamma}_0}{\pi} \left\{ \frac{\sin\phi}{2a-1} [\bar{c} - \zeta_{TE} + \zeta_{LE}] \right. & \bar{x} < \bar{x}_{TE} \\ \quad + \frac{\bar{\Gamma}_0 \cos\phi}{\sqrt{2a-1}} \left(\frac{\sin\phi}{2a-1} - \frac{1}{a} \right) \\ \quad \times [\psi_{TE} + \xi_{TE} - \psi_{LE} - \xi_{LE}] \\ \quad \left. - \frac{1}{2a} \ln \left| \frac{\zeta_{TE}-1}{\zeta_{TE}+1} \frac{\zeta_{LE}+1}{\zeta_{LE}-1} \right| \right\} \\ -\frac{2\bar{\Gamma}_0 \sin\phi (\zeta_{TE} - \bar{x}_{TE}) - 1/\bar{x}_{TE}}{\pi a (\zeta_{TE} - \bar{x}_{TE}) + \bar{x}_{TE}} \Delta_{TE} \end{cases} \tag{4.26}$$

4.2.3.5 Comparison with wake survey in hover condition

A quantifiable measurement is made by determining the centres of extrados and intrados slipstreams. Due to the presence of wing wake, the slipstream centre cannot be easily defined. An indirect method was used to determine slipstream centre through shear stress at the boundary.

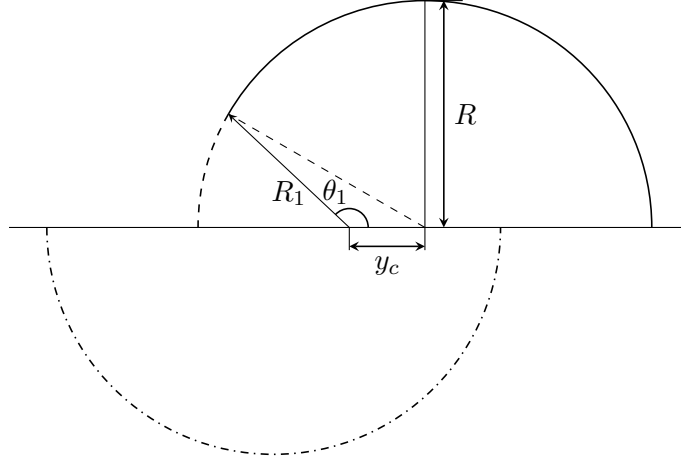


Figure 4.12: Geometry relations to determine slipstream centre

From turbulent jet theory, it can be concluded that the axial velocity profile of a round jet surrounded by static air can be approximated by Gaussian function. The jet boundary corresponds to where the extrema of shear stress exists. If streamwise partial derivatives ($\frac{\partial}{\partial x}$) are assumed to be small compared to cross flow derivatives, the cross-flow shear stress can therefore be determined as

$$\tau_{xy} = \mu \frac{\partial u}{\partial y} \quad (4.27)$$

$$\tau_{xz} = \mu \frac{\partial u}{\partial z}. \quad (4.28)$$

The wake boundary was then determined to be the locus of maximum transverse shear stress, drawing analogy from conclusions of turbulent jet theory:

$$(y, z) : \max \sqrt{\tau_{xy}^2 + \tau_{xz}^2}. \quad (4.29)$$

The vertical extrema of the slipstream boundary were chosen as the radius of contracted wake R , as shown in Fig. 4.12. The angular and radial position of the closest points of slipstream boundary to rotational axis were determined as R_1 and θ_1 . From geometry relations, the slipstream centre can then be determined as

$$y_c = \sqrt{R_w^2 - (R_1 \sin \theta_1)^2} + R_1 \cos \theta_1. \quad (4.30)$$

The displacement of slipstream centre from propeller axis can therefore be found, and the results for three test cases can be found in Table 4.2.

RPM	C_T	y_c/R_p	Theoretical y_c/R_p	Error
5770	0.1907	0.4290	0.4252	0.9%
8000	0.1908	0.4086	0.4253	3.9%
10000	0.1906	0.4017	0.4252	5.5%

Table 4.2: Centreline displacement at various rotation speeds

From Table 4.2 it can be concluded that the three cases have nearly identical wake displacement. A theoretical result was also calculated for each case. This value is based on the previously derived potential flow method.

The resulting model for centreline displacement $\bar{y}_c = y_c/R_p$ is a function of downstream location $\bar{z} = z/R_p$, with blade tip vortex shedding angle ϕ as a parameter. The centreline displacement is given in Eq. (4.22) at static condition.

Angle ϕ can be calculated from momentum theory using thrust coefficient, and \bar{z}_{LE} , \bar{z}_{TE} are leading edge and trailing edge locations divided by propeller radius with origin at rotor centre and negative direction pointing downstream.

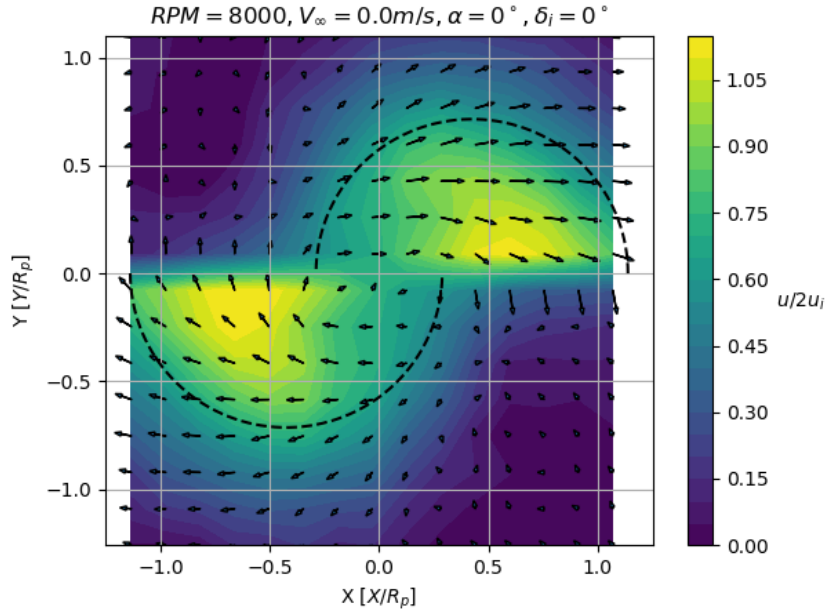


Figure 4.13: Velocity distribution at survey plane for symmetrical configuration at 8000rpm, with displaced slipstream boundary

In Fig. 4.13, slipstream boundary from momentum theory was displaced by the predicted amount from Table 4.2. The deformed boundary appeared to include both high-speed flow regions at extrados and intrados. The results confirm that at static condition, displaced centreline can be accurately calculated using the theoretical model. The results seem to affirm that the presence of wing serves as an imaginary plane for slipstream vortex system,

and its induced transverse velocity component explains centreline displacement.

4.2.4 Conclusion

In this section, a wake survey was presented immediately after a propeller-wing combination to investigate the flow interaction for a convertible UAV under hover condition. A symmetric wing profile was tested in ENAC indoor flight arena at calm wind condition. Velocity magnitude and direction were measured by a 5-hole probe at a plane perpendicular to streamwise direction and downstream of trailing edge. The test was conducted with zero flap deflection, as well as with flap deflection of 15° in either direction.

The results demonstrated that the presence of wing influences velocity distribution within propeller slipstream compared to a free propeller. In the experiment, the upper half slipstream was observed to translate towards outboard while the lower half slipstream translates towards inboard. The results contrast with most reduced-order model of propeller-wing interaction where propeller wake was assumed to keep its cylindrical shape.

Comparison with a theoretical model suggests that wing influence on propeller slipstream velocity distribution can be accurately modelled using method of reflection on slipstream streamwise vorticity.

The influence of wing on velocity distribution within slipstream was observed to be different between upper and lower surfaces when flap deflection was present, with the deformation being stronger on the wing surface opposite to flap deflection.

The present study is a first step towards more accurate prediction of forces and moments on convertible UAVs via reduced order models.

4.3 Aerodynamic augmentation of closely-coupled propeller

4.3.1 Background

Blown flap configuration has been studied experimentally in aeronautical community. During the 1950s, with the development of VTOL aircraft, tests have been performed at NASA research centres on propeller-wing combinations. Kuhn et al [KD56] investigated a four-propeller wing combination intended for a tilt-wing design. The tests were conducted in NASA Langley MPH 300 7- by 10-foot tunnel with a semi-span scaled model. The propeller-wing combination can be rotated to simulate angle of attack from 0° to 90° . The test gave invaluable information on longitudinal flight characteristics on a blown flap configuration. Moreover, the test was destined for transition flight study, and thus flight conditions at large angle of attack were surveyed. Kuhn et al notably pointed out that at hover condition, aerodynamic coefficients should be defined in terms of slipstream condition instead of freestream condition, which reaches singularity at hover. The test revealed significant challenge to mitigate nose-

down pitch moment generated by the blown-flap. A hypothetical transition corridor where equilibrium flight could be achieved was also presented. The experiment used flap only for lift augmentation and not for flight control purposes.

In 1992, Gentry et al [GJTA94] conducted a reduced-scale experiment of an external blown flap model in NASA Langley 14- by 22-foot wind tunnel at cruise condition. The experiment explored various installation parameters including propeller install angle, vertical position. The high-aspect-ratio wing was equipped with a double-slotted flap, and was tested from -30° to 40° angle of attack. Results showed that the impact of install angle and vertical placement of propeller has large influence on lift augmentation. No independent thrust measurement was conducted and thus global force and moment values contain the propulsive force.

In recent years, high fuel prices motivated research on the beneficial interaction between propeller and lifting surfaces. Notable studies such as the ones conducted by Veldhuis et al [Vel04]; [Epe17] looked at aircraft optimisation from propeller and wing interaction. Various parameters such as propeller placement, wing twist and rotation direction were studied. Wind tunnel experimental data emphasise the importance of propeller install angle and vertical placement. Inboard-up rotation configuration was determined to be most beneficial for a twin engine aircraft to maximise lift-to-drag ratio. Tested condition however remains in cruise flight with small angle of attack.

4.3.2 Present Work

In view of past studies, the present work focused on providing a parametric study on convertible aircraft configuration during transition flight. Various propeller install positions and flap deflection angles were tested and longitudinal aerodynamic loads including lift, drag and pitch moment were measured to conduct analysis on transition flight dynamics, although only lift and pitch moment results are presented.

In section 4.4, the experiment set-up in ISAE low Reynolds number SaBRe wind tunnel is presented. The test condition is specified and explained.

In section 4.5, a theoretical analysis on the composition of aerodynamic loads for wing surface under propeller wake influence is introduced. This new approach normalises the propeller effects and allows comparison of experimental data at different thrust conditions.

Experimental data of wing lift and moment characteristics processed through this method are then presented in section 4.6. Propeller wake effect is analysed in three scenarios : 1) different flap settings δ_f ; 2) different propeller install angles δ_i ; 3) different vertical positions z_p . Wing chord line were used to define propeller install angle and vertical displacement, as illustrated in Fig. 4.14. For each scenario, two cases at different angles of attack are presented. $\alpha = 10^\circ$ represents low angle of attack situation where wing is free from stall onset ; $\alpha = 40^\circ$ represents high angle of attack encountered during transition flight.

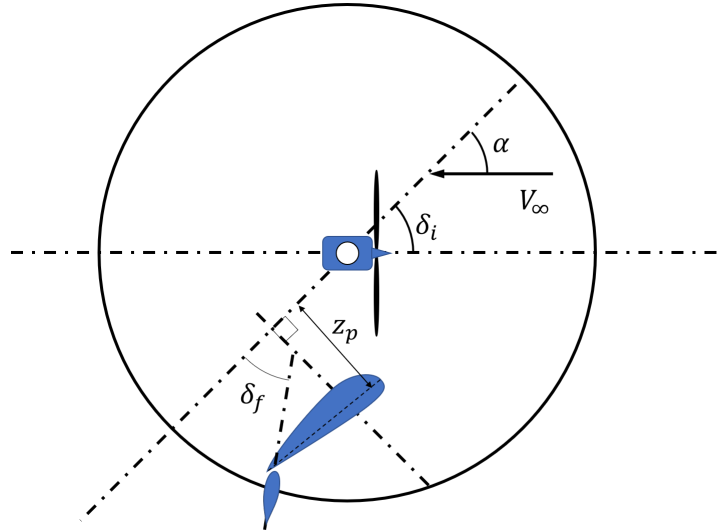


Figure 4.14: Configuration Parameters

4.4 Experiment Set-Up

An explanation of the propeller-wing configuration is presented in this section to provide a complete understanding of the mechanisms and effects involved in the measurement. Experiment equipment set-up is presented first, followed by intended test conditions.

4.4.1 Description of Apparatus

The measurement system was installed at ISAE low Reynolds number wind tunnel SaBRe, which is described in section 3.3. The model comprises two independent parts : a high-aspect-ratio wing and a propeller-motor assembly. The latter was the identical system described and tested in section 3.3, shown in Fig. 3.12.

4.4.1.1 Half-span wing model

The wing model tested was designed to represent a typical long endurance convertible UAV. To reduce induced drag in cruise flight, a high aspect ratio is desired, which is different from general convertible UAVs [LDM14]. The full-span aspect ratio is chosen to be 5 with a 200mm chord length. Due to the wing tunnel test section dimension being 1200mm \times 800mm, only half-span model is manufactured to minimise wall effect. Figure. 4.16 illustrates the semi-span wing model.

The wing plan-form adopted a generic rectangular shape. Its cross-section profile was chosen to be constant NACA0018 airfoil, since thick airfoils are typically used for UAV design due to their higher maximal lift coefficient and extra volume to accommodate structural

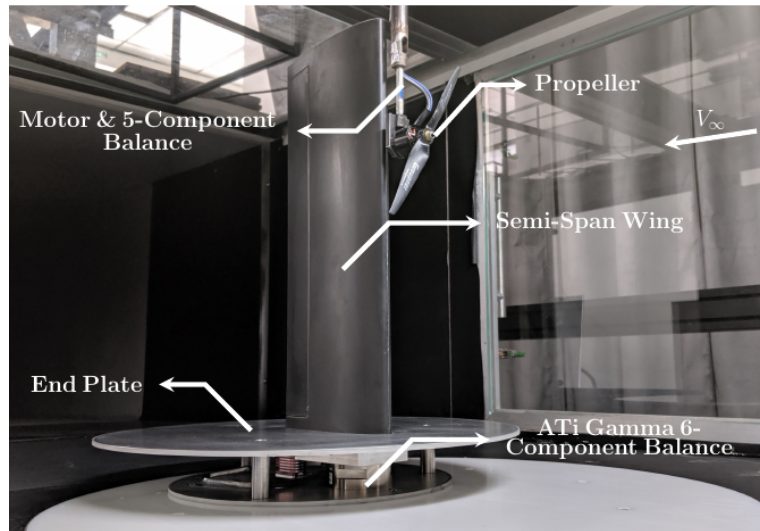


Figure 4.15: Installation of Wing on 2KPi Turntable

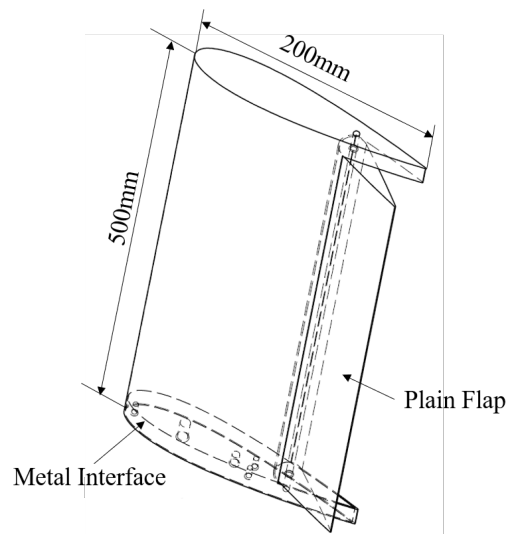


Figure 4.16: Isometric View of Sem-Span Model

components. The last 30% of the wing featured a plain flap that can be deflected up to 30° on either side.

The wing was supported by a metal double-spar structure with carbon-fibre skin. The structure was stronger and heavier than conventional UAV design but was necessary to ensure no structure influences in the test results. The root section contains a metal machined rib to facilitate installation on balance. The wing main characteristics are summarised in Table 4.3.

Items	Value	Unit
Aerofoil	NACA0018	–
Span	500	[<i>mm</i>]
Chord	200	[<i>mm</i>]
Flap Chord	60	[<i>mm</i>]
Flap Limitation	± 30	[$^{\circ}$]

Table 4.3: Wing Specification

4.4.1.2 Installation and motion control

The wing was mounted on a 2KPi turntable underneath the wind tunnel floor to allow angle of attack variations. The installation is shown in Fig. 4.17.

The wing assembly was attached to the larger 2KPi turntable plate through a smaller position plate 50*mm* beneath the root section. This was designed to facilitate change of vertical displacement respect to propeller axis. Various positioning holes were machined on the turntable plates perpendicular to wing chord line, so that the position plate could displace the wing relative to propeller, allowing studies of different propeller vertical displacements z_p . Furthermore, a constant difference between wing angle and propeller angle represents propeller installation angle δ_i .

On top of the position plate, the 6-component balance was installed which will be further detailed in the next section. The wing was connected to the balance through an intermediate piece, and this ensures that wing loads were isolated from other factors in the balance measurement.

Three columns on the position plate supported an end plate whose lower surface was aligned with wing root section. The end plate was added to minimise the interference of windtunnel wall boundary layer which is developed from the test section entrance. Such interference prevents the assumption that wing root plane is a symmetric plane [Die+15]. By adding the end plate, the root section encounters boundary layer developed from the end plate edge and thus a reduction in its thickness. The diameter of end plate was determined to be 520*mm* to minimise effect of end plate leading edge. There was a 0.2*mm* gap between the contour of wing root and the end plate to ensure end plate plate load doesn't interfere with wing load. The gap has been visually checked during test condition and no contact between wing model and end-plate was observed.

The installation allowed adjustments of wing flap angle δ_f , propeller install angle δ_i and vertical displacement z_p during test, as shown in Fig. 4.14. The installation ensures a longitudinal distance of 60*mm* between wing leading edge and propeller centre.

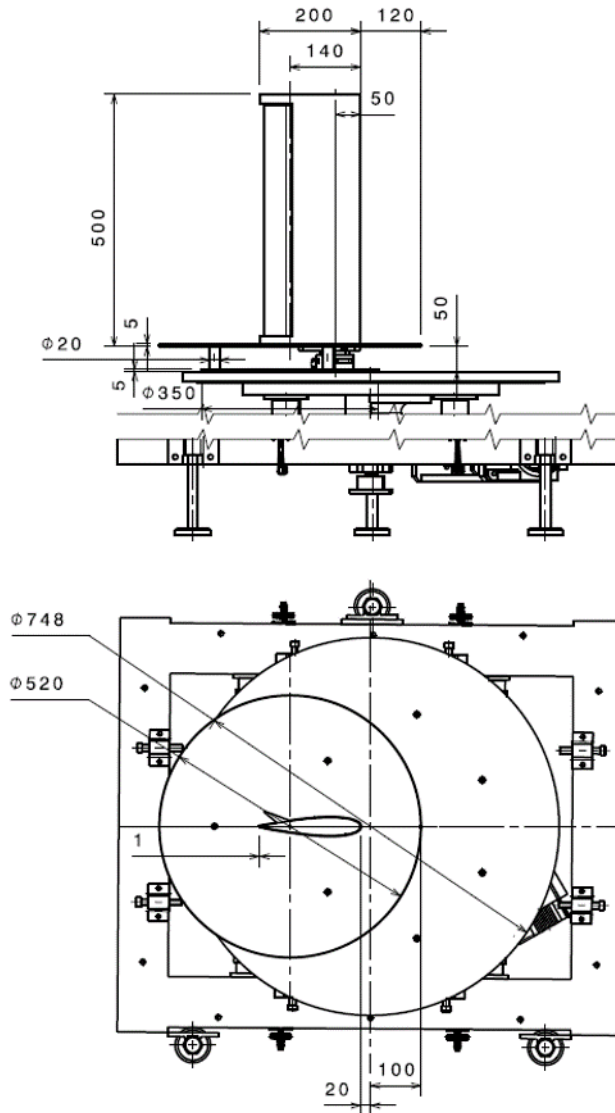


Figure 4.17: Side and Top View of Wing Installation on 2KPi Turntable

4.4.1.3 Wing load measurement

Propeller and wing aerodynamic loads were measured independently. Balance on the propeller assemble was described in section 3.3 and appendix A, and thus won't be discussed here. Aerodynamic force and moment on the wing were measured by an ATi Gamma six-component balance. The balance was directly connected with wing and flap assembly. Installation was designed that the end plate connects independently from balance-wing assembly to the turntable, and thus balance measurements will be free of aerodynamic forces on the end plate. A 0.2mm gap was left where the wing enters the end plate.

Manipulation of test equipment and data sampling were conducted through National

Instrument LabView interface. The data were sampled at $1000Hz$ for $5s$ period. It was then filtered by a low-pass filter at $0.1Hz$ cut-off frequency before average.

4.4.2 Test Conditions

Test conditions were determined to survey a "transition corridor" - a relationship between maximum / minimum equilibrium airspeeds and aircraft attitude [PW91].

The flow condition is defined by the transition corridor, which is approximated by the square root of co-tangent of propeller angle, $V_\infty \approx 4.369\sqrt{\cot \alpha_p}$. This approximation is done by analysing the thrust requirement near $\alpha_p = 90^\circ$, where

$$T \sin \alpha_p = W = mg \quad (4.31)$$

$$T \cos \alpha_p = D = \frac{1}{2}\rho C_D S_{\text{ref}} V_\infty^2 \quad (4.32)$$

This assumes that flow separation at near hover condition causes negligible lift coefficient and little drag coefficient variation, and thus :

$$V_\infty = \sqrt{C_1 \cot \alpha_p} \quad (4.33)$$

where $C_1 = \frac{2W}{\rho C_D S_{\text{ref}}}$.

Obviously, the same analysis cannot directly apply to horizontal flight, where from conventional flight performance analysis :

$$V_\infty \propto \sqrt{\frac{1}{\alpha}} \quad (4.34)$$

The proportional constant is found for a cruise flight at $\alpha = 5.5^\circ$ and $V_\infty = 15m/s$ generating $10N$ lift, as analysed by XFLR5 lifting-line method [Xfl].

The estimated transition corridor is plotted in Fig. 4.18. The orange curve depicts low-speed portion of transition corridor and the green curve represents high-speed portion. The upper limit is derived from critical angle of attack for NACA0018 airfoil at $V_\infty = 15m/s$.

It should be pointed out that this analysis is very rudimentary and should only be used as a model analysis. The hover relation is obtained by neglecting aerodynamic lift, while the horizontal flight relation mainly considers aerodynamic lift and neglects propeller thrust. Thus the proportional constants aren't necessarily the same. Furthermore, for detailed transition analysis, both propeller thrust and aerodynamic lift must be considered.

However, a verification test was conducted in the windtunnel to find flight equilibrium at various speed. The blue locus represents the actual transition corridor obtained in the

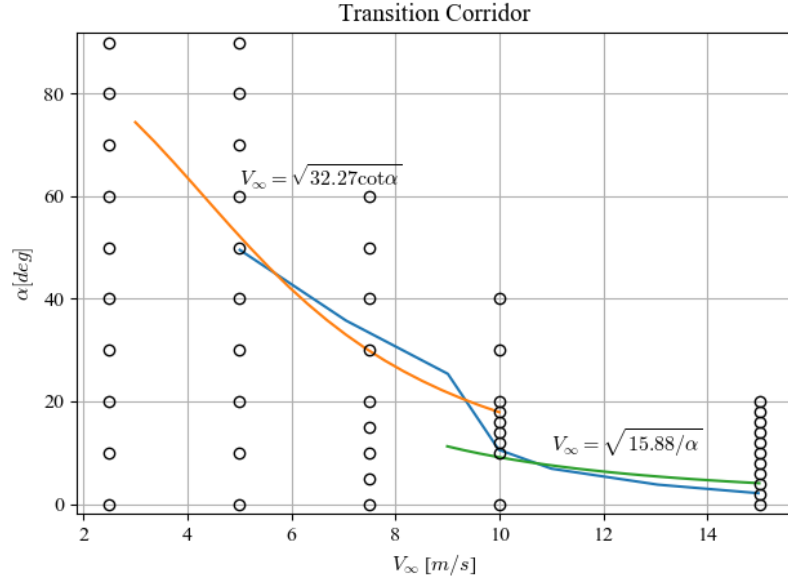


Figure 4.18: Transition Corridor and Test Conditions for Tested Wing

verification test, and it situates very close to the previous estimates.

The less accurate analysis is also justified considering test conditions will cover a wider range on both side of the transition curve.

From the bounded region, a test condition matrix can be derived in Table 4.4.

V_∞ [m/s]	Re	α [°]										
2.5	3.4×10^4	0	10	20	30	40	50	60	70	80	90	
5.0	6.8×10^4	0	10	20	30	40	50	60	70	80	90	
7.5	1.0×10^5	0	10	20	30	40	50	60	–	–	–	
10.0	1.4×10^5	0	10	12	14	16	18	20	30	40	–	

Table 4.4: Testing Conditions

4.5 Decomposition of Thrust-Augmented Aerodynamic Loads

Among the test cases, freestream and thrust condition vary greatly, and thus measurements under different conditions cannot be compared directly. This chapter seeks to provide a method to decompose and normalise the variations in wing aerodynamic loads according to different origins. Such decomposition, while not a complete analytic model for arbitrary propeller-wing configuration, provides further insight into different contributions in interactions between propeller and wing, with their proper scaling laws. Therefore, it enables detailed comparisons of propeller wake effects of different δ_f , δ_i and z_p .

The momentum theory is briefly introduced, which is used to model the propeller wake. Decomposition of wing lift, drag and moment variations due to propeller wake is derived, these variations are characterised by respective augmented aerodynamic coefficients, a newly introduced set of non-dimensional coefficients.

4.5.1 Momentum theory

Propeller momentum theory is a well-developed analytical model to describe relations between flow conditions and aerodynamic efforts. The model assumes uniform thrust loading over propeller disk, which is related to a constant discontinuity in static pressure across the disk.

$$\Delta p = T/S_p \quad (4.35)$$

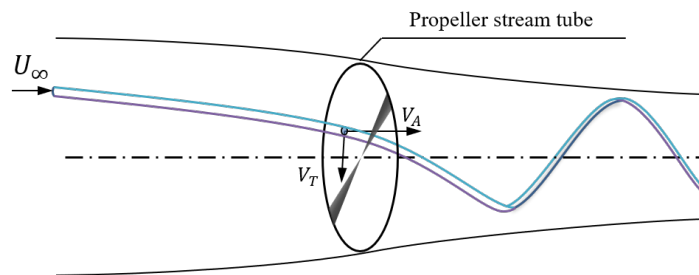


Figure 4.19: Propeller Streamtube

The flow properties are derived for the streamtube that encloses exactly the propeller disk. Fig. 4.19 gives an illustration of the flow pattern as the streamtube passes propeller boundary.

Due to Δp , airflow starts to accelerate as it approaches propeller disk, and the streamtube consequently contracts to preserve continuity. Momentum analysis establishes relation between thrust loading and flow acceleration at propeller disk.

$$T/S_p = \rho V_w (V_\infty + V_i) \quad (4.36)$$

where V_w is the difference in flow speed at far downstream (ultimate wake) from V_∞ and V_i is the flow speed difference at propeller disk (induced speed).

Streamtube contraction continues downstream until ambient pressure is reached in the ultimate wake. By satisfying continuity and momentum conservation, the ultimate wake velocity can be resolved.

$$V_w = 2V_i \quad (4.37)$$

The streamline in Fig. 4.19 also demonstrates a swirling motion about the propeller axis. This circular motion is mainly due to skin friction over propeller blade and can be related to power consumed by the rotor. Since swirl velocity observes anti-symmetry on points at equal distance away on opposite sides from propeller axis, this component will not be further analysed for its effect on the wing surface.

4.5.2 Augmented aerodynamic loads

An unswept wing with propulsion system is described by geometry parameters shown in Fig. 4.20. Wing geometry is described by its chord, twist distribution laws : $c(y)$, $\theta(y)$. The following non-dimensional measures are introduced :

$$\bar{y} = 2y/B \quad (4.38)$$

$$\bar{c}(\bar{y}) = c(y)/c_0 \quad (4.39)$$

where c_0 is geometric mean chord and B is wingspan, whose product is reference surface area $S_{\text{ref}} = Bc_0$.

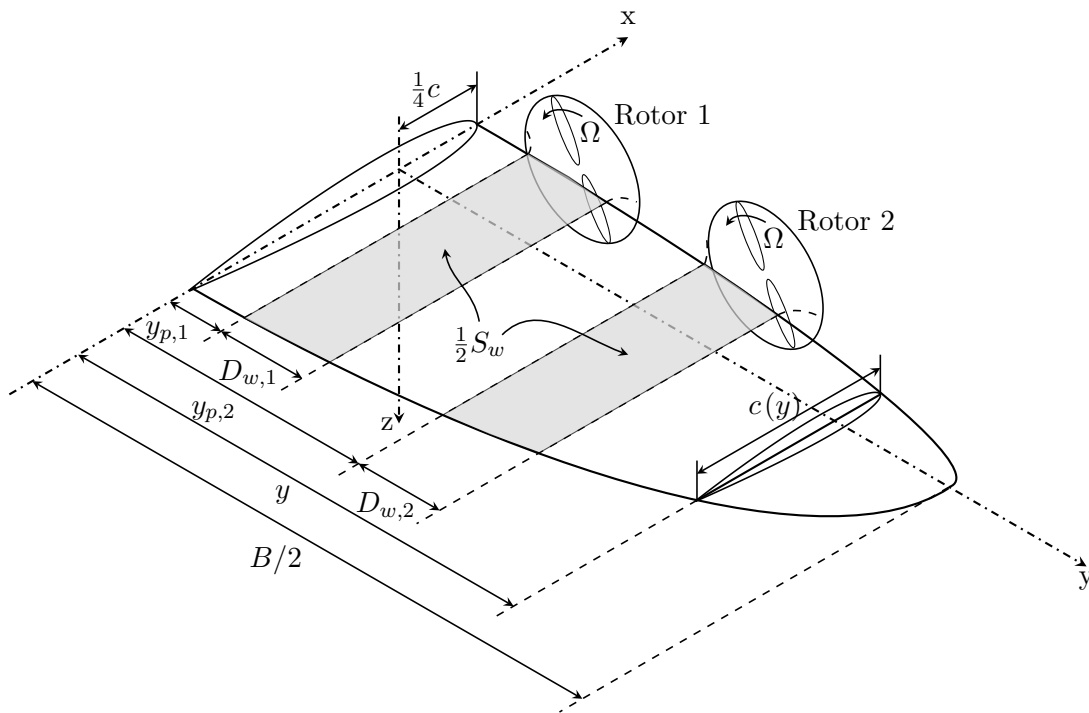


Figure 4.20: Wing Geometry Definition

Aerodynamic load on the wing without propeller is first considered. Suppose flow pattern over the wing to be quasi 2-dimensional, wing aerodynamic performance can be obtained from the distribution of lift, drag and moment coefficients (c_l , c_d , c_m) at each infinitesimally thin section.

$$L_0 = \frac{1}{2} \rho V_\infty^2 S_{\text{ref}} \int_0^1 c_l(\bar{y}) \bar{c}(\bar{y}) d\bar{y} \quad (4.40)$$

$$D_0 = \frac{1}{2} \rho V_\infty^2 S_{\text{ref}} \int_0^1 c_d(\bar{y}) \bar{c}(\bar{y}) d\bar{y} \quad (4.41)$$

$$M_{0,0.25c} = \frac{1}{2} \rho V_\infty^2 S_{\text{ref}} \text{MAC} \int_0^1 c_{m_{0.25c}}(\bar{y}) \bar{c}(\bar{y})^2 d\bar{y} \quad (4.42)$$

where $\text{MAC} = \int_0^1 \bar{c}(\bar{y}) c(\bar{y}) d\bar{y}$ is mean aerodynamic chord. Subscript 0 denotes that these are quantities without propeller. The expressions also assume symmetric load distribution.

There exist two effects of propeller wake on an airfoil section : the increase of flow speed and change in flow direction. These effects affect airfoil operating condition which specifically includes dynamic pressure $q = \frac{1}{2} \rho V^2$, chord-based Reynolds number $Re_c = Vc/\nu$ and angle of attack α . Dynamic pressure variation affects scaling of aerodynamic coefficients, while variations in Re_c and α alter directly the coefficients.

The influences of propeller wake are thus considered as increased dynamic pressure $\frac{1}{2} \rho (V_\infty + V_w)^2$ and modified aerodynamic coefficients $c_l + \Delta c_l$, $c_d + \Delta c_d$ and $c_m + \Delta c_m$. These influences only apply to sections immediately after the propeller, denoted by $\bar{y}_{bl} = [\bar{y}_{p,1}, \bar{y}_{p,1} + 2D_{w,1}/B] \cup [\bar{y}_{p,2}, \bar{y}_{p,2} + 2D_{w,2}/B] \cup \dots \cup [\bar{y}_{p,n}, \bar{y}_{p,n} + 2D_{w,n}/B]$, where $\bar{y}_{p,i}$ and $D_{w,i}$ are the inboard position and diameter of i -th propeller ultimate wake.

The expression for wing lift with propeller influence can be derived. For simplicity, the functional dependencies on \bar{y} are omitted where no confusion exists.

$$L = \frac{1}{2} \rho S_{\text{ref}} \left[V_\infty^2 \int_{[0,1]-\bar{y}_{bl}} c_l \bar{c} d\bar{y} + \int_{\bar{y}_{bl}} (V_\infty + V_w)^2 (c_l + \Delta c_l) \bar{c} d\bar{y} \right] \quad (4.43)$$

After arithmetic manipulations, the base wing lift L_0 can be recovered.

$$L = L_0 + \rho S_{\text{ref}} \int_{\bar{y}_{bl}} V_w (V_\infty + V_w/2) (c_l + \Delta c_l) \bar{c} d\bar{y} + \frac{1}{2} \rho V_\infty^2 S_{\text{ref}} \int_{\bar{y}_{bl}} \Delta c_l \bar{c} d\bar{y} \quad (4.44)$$

$$= L_0 + \Delta L_T + \Delta L_\Gamma \quad (4.45)$$

Total lift is thus decomposed into three components : 1. base lift L_0 ; 2. thrust-augmented lift ΔL_T and 3. circulation-augmented lift ΔL_Γ . It's worth noting that the decomposition of ΔL_T and ΔL_Γ isn't strictly clear, however as will be shown later, ΔL_T can be directly scaled with thrust while ΔL_Γ don't explicitly contain influence of speed variation.

For ΔL_T , by assuming uniform wake speed distribution and using integration by parts, the expression can be further derived.

$$\Delta L_T = \rho S_w V_w (V_\infty + V_w/2) (\bar{C}_L + \Delta \bar{C}_L) \quad (4.46)$$

where $S_w = S_{\text{ref}} \int_{\bar{y}_{bl}} \bar{c} d\bar{y}$ is wing surface area blown by the propeller wake and \bar{C}_L is mean lift coefficient within blown sections $\bar{C}_L = \int_{\bar{y}_{bl}} c_l \bar{c} d\bar{y}$.

Recall the momentum relations Eq. 4.36 and Eq. 4.37, the thrust-augmented lift is finally obtained by relating the dynamic pressure terms to momentum thrust.

$$\Delta L_T = T (S_w/S_p) (\bar{C}_L + \Delta \bar{C}_L) \quad (4.47)$$

Circulation-augmented lift can be re-written by using the mean lift coefficient variation within blown surface.

$$\Delta L_\Gamma = \frac{1}{2} \rho V_\infty^2 \Delta \bar{C}_L S_w \quad (4.48)$$

To allow comparison of lift augmentation effects at different thrust conditions, an augmented lift coefficient (ALC) is defined.

$$ALC = \frac{L - L_0}{T (S_w/S_p)} \quad (4.49)$$

Substitute Eqs. 4.47 and 4.48, ALC can be related to the two mean lift coefficients in blown area.

$$ALC = \bar{C}_L + \left(1 + \frac{\lambda_\infty^2}{2C_T}\right) \Delta \bar{C}_L \quad (4.50)$$

where $\lambda_\infty = \frac{V_\infty}{\Omega R}$ is tip speed ratio and C_T is thrust coefficient defined in Eq. 4.51.

$$C_T = \frac{T}{\rho (\Omega R)^2 S_p} \quad (4.51)$$

Eq. 4.50 provides a detailed insight into the mechanisms of thrust augmented lift. The base mean lift scales with propeller thrust and the blown surface area relative to disk area, and this augmentation comes solely from the increased dynamic pressure after propeller.

Variations in Reynolds number and local angle of attack cause $\Delta \bar{C}_L$, and this effect depends simultaneously on propeller thrust and freestream condition. In Eq. 4.50, the coefficient in front of $\Delta \bar{C}_L$ is the ratio between the energy flux in ultimate wake and the power added in the streamtube for flow acceleration. A wake energy ratio η_w is defined in Eq. 4.52, where P_{Froude} is the power added in the wake.

$$\eta_w = \frac{P_{\text{Froude}}}{\dot{E}_{k,wake}} = \frac{2C_T}{2C_T + \lambda_\infty^2} \quad (4.52)$$

The range of η_w generally is $[0,1]$, where $\eta_w = 0$ represents zero thrust condition and $\eta_w = 1$ during hover. The wake energy ratio is a weighted measure of propeller thrust effect and freestream.

Augmented drag and pitch moment coefficients (ADC, AMC) could be treated in a similar fashion.

$$ALC = \bar{C}_L + \Delta\bar{C}_L/\eta_w \quad (4.53)$$

$$ADC = \bar{C}_D + \Delta\bar{C}_D/\eta_w \quad (4.54)$$

$$AMC_{0.25c} = \frac{M_{0.25c} - M_{0,0.25c}}{TMAC(S_w/S_p)} = \bar{C}_M + \Delta\bar{C}_M/\eta_w \quad (4.55)$$

For straight wing at small angle of attack, a further simplification could be made for augmented moment coefficient, as the local aerodynamic centre is situated at $0.25c$. Therefore, the augmented moment coefficient is simply zero-lift moment coefficient.

$$AMC_{0.25c} = C_{M0,0.25c}, \text{ for small } \alpha \quad (4.56)$$

This suggests that propeller effect doesn't directly change airfoil pitching behaviour but rather amplifies the original $C_{M0,0.25c}$.

4.6 Results and Discussions

Experimental data from low speed wind tunnel test are presented in this chapter. Discussion starts with an explanation of different effects contained in measured data. This discussion put emphasis on the interpretation of thrust-augmented aerodynamic loads, especially in relation to the current experiment.

Results for two typical angle of attack $\alpha = 10^\circ$ and 40° are introduced to illustrate the effects of wing flap δ_f , propeller install angle δ_i and vertical displacement z_p .

4.6.1 Measurement of Aerodynamic Loads

During the measurement, various configurations and test conditions have been investigated. There are multiple ways to compare and interpret obtained data. In this study, only propeller wake effects on a given aerodynamic configuration will be looked at. This means that the

effect of changing aerodynamic profile, specifically the flap deflection, isn't the focus.

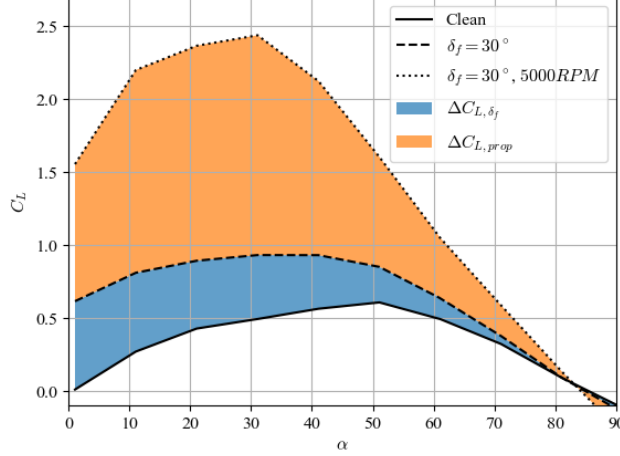


Figure 4.21: Lift coefficient for various configurations at $V_\infty = 5m/s$

To better understand the analysis, a set of measurement at $V_\infty = 5m/s$ is plotted in Fig. 4.21. The solid line represents lift coefficients obtained without propeller assembly and with flap at neutral position. For the symmetrical airfoil used during test, C_L is null at zero angle of attack and it reaches a maximum of 0.6 at around $\alpha = 50^\circ$ in post-stall region. Due to the large interval between measured α , stall region cannot be observed.

When the flap is deflected by 30° , the measured lift coefficient follows the dashed line. Deflection of flap increases positive camber, and thus C_L at $\alpha = 0$ is increased by 0.6. Maximum C_L reaches to a higher value of 0.8 in post-stall region. The blue shaded area between two curves represents the effect of flap on lift coefficient $\Delta C_{L,\delta_f}$.

If propeller assembly is installed and is running at $5000RPM$, the measured C_L on the wing surface is further increased. The effect of propeller is represented by the orange shaded area $\Delta C_{L,prop}$. This variation in lift coefficient is based on an already established 30° flap deflection, and thus is purely propeller effect on the wing surface, whereas the combined area of orange and blue region contains both the effect of aerodynamic profile (δ_f), and the effect of propeller wake.

As mentioned before, only propeller wake effect is analysed in the current study, hence the variation represented by the orange shade in Fig. 4.21. The definition of aforementioned aerodynamic coefficients conforms with this objective.

4.6.2 Propeller wake effect on wing flap

Figure. 4.22 and Fig. 4.23 present augmented lift and moment coefficients at $\alpha = 10^\circ$. On the left is ALC plotted against wake energy ratio η_w , with high-thrust regime towards the

right. Results for five different flap settings are included as shown in the legend. A trend line corresponding to the neutral flap case has been included, assuming $\Delta\bar{C}_L \approx const$ in Eq. 4.50. At this small α , the corresponding experimental data match closely to the derived trend. This suggests that circulation induced lift component is inversely proportional respect to η_w . It should be noted that even the wing is made of symmetrical airfoil sections, $\Delta\bar{C}_L \neq 0$.

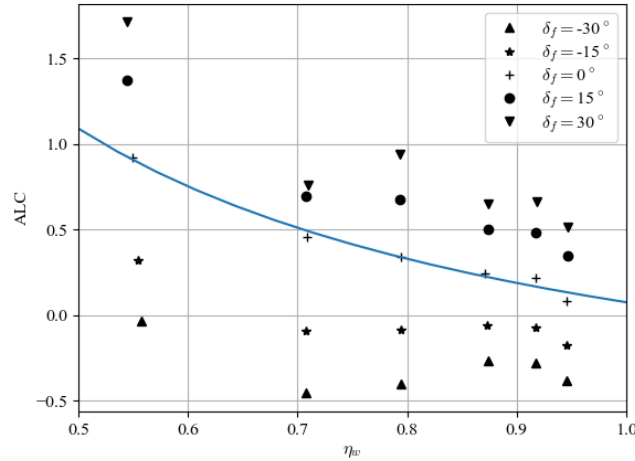


Figure 4.22: Augmented Lift Coefficient at $\alpha = 10^\circ$ for various δ_f

For cases with flap deflections, the results suggest that propeller wake effects have different influences. It tends to augment the lift production at positive flap angle while the augmentation effect is diminished or reversed for negative flap deflection. This is because at these conditions, thrust induced lift component \bar{C}_L is most likely negative while the circulation induced lift component takes opposite sign.

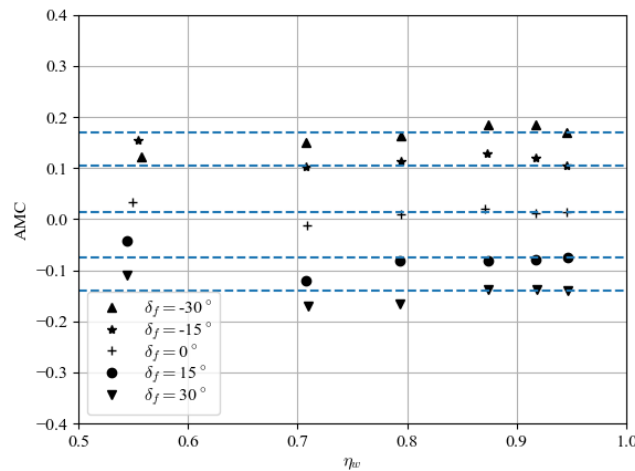


Figure 4.23: Augmented Moment Coefficient at $\alpha = 10^\circ$ for various δ_f

AMC is plotted on the right hand side against η_w for different flap settings. Constant lines are plotted, and their values are the AMC reached at the largest η_w for corresponding flap settings. The trend confirms for small α , AMC is approximately constant as in Eq. 4.56. Due to the symmetrical profile, pitch moment is close to zero for neutral flap position. Positive flap deflection induces pitch down moment. The dimensional augmented thrust is thus proportional to the propeller thrust loading.

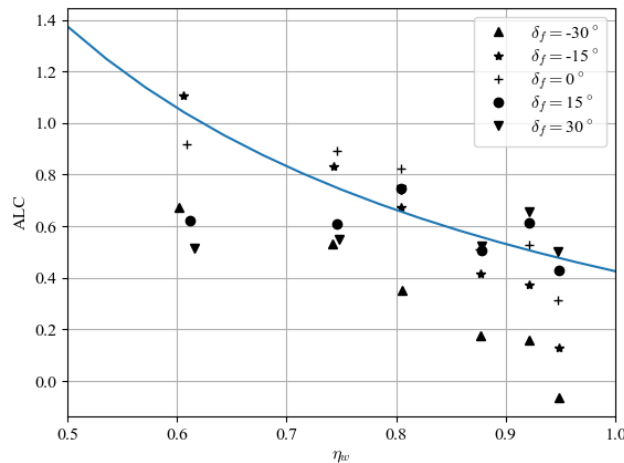


Figure 4.24: Augmented Lift Coefficient at $\alpha = 40^\circ$ for various δ_f

Results for higher $\alpha = 40^\circ$ are presented in Fig. 4.24 and 4.25 in a similar fashion. At neutral flap deflection the high α condition gives larger ALC values, this is expected as \bar{C}_L should increase for higher α . However the scatter around the trend line becomes more significant suggesting circulation induced lift coefficient $\Delta\bar{C}_L$ is no longer a constant function of η_w .

ALC relationship at non-zero flap deflection also becomes more complicated. At hover condition, a slightly larger augmentation effect can still be observed for positive flap deflection over $\delta_f = 0$ case. As η_w decreases, or increasing V_∞ , ALC for both positive deflection stays constant at around $\eta_w = 0.6$, suggesting a control surface saturation. In fact, since at higher airspeed, thrust loading decreases, and thus dimensional augmented lift is reduced. For negative flap angle, ALC increases with decreasing η_w , and could possibly reach a higher value than that for neutral flap.

Moment augmentation at higher α differs from the previous low α case. In Fig. 4.25, it can be clearly observed that AMC for all flap settings is no longer constant in η_w . At high-thrust condition, propeller wake effect depends on flap deflection direction. Augmented pitch up tendency is observed for negative flap deflection. As η_w decreases, AMC for different flap settings starts to converge and eventually reaches to a similar negative value at around $\eta_w = 0.6$. This suggests that propeller wake no longer has an augmentation effect on flight control through trailing edge flap.

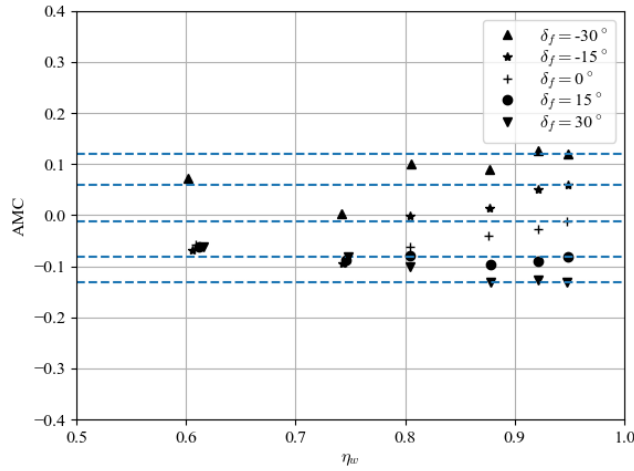


Figure 4.25: Augmented Moment Coefficient at $\alpha = 40^\circ$ for various δ_f

4.6.3 Effect of propeller install angle

The effect of δ_i on ALC and AMC is presented in Fig. 4.26 and Fig. 4.27 for $\alpha = 10^\circ$. Three different δ_i have been tested towards either side of the wing surface. The data concentrate closely with experimental data of $\delta_i = 0$. The scatter is most obvious at high thrust condition (maximum η_w). As the propeller install angle changes orientation of propeller wake, the effect takes most of its contribution from circulation induced lift $\Delta\bar{C}_L$. At lower η_w , the induced velocity has less influence on flow direction for downstream sections, the data start to cluster closer together.

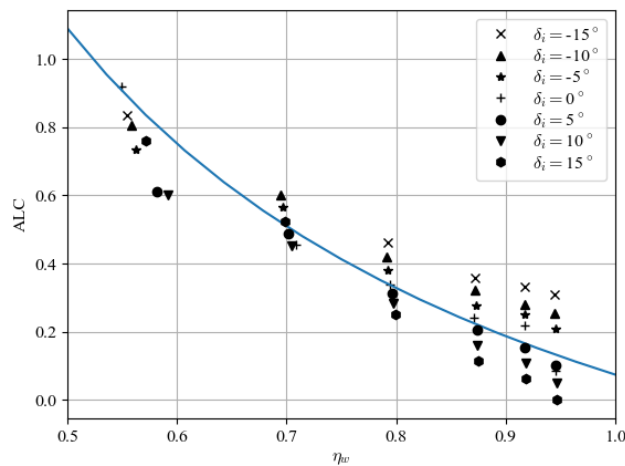


Figure 4.26: Augmented Lift Coefficient at $\alpha = 10^\circ$ for various δ_i

In Fig. 4.27, the measured augmented moment coefficients fall in a close region between

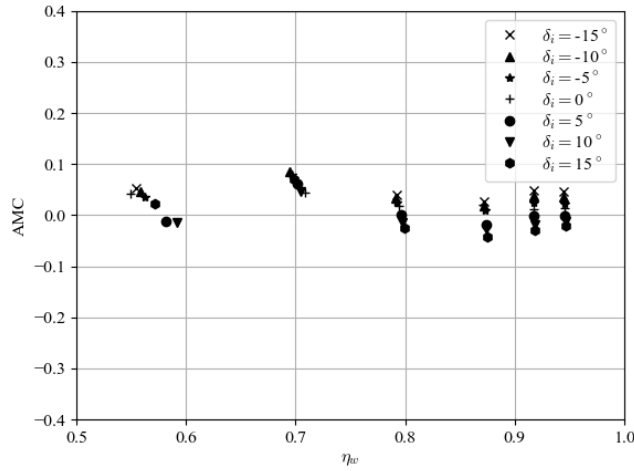


Figure 4.27: Augmented Moment Coefficient at $\alpha = 10^\circ$ for various δ_i

± 0.05 for $\eta_w > 0.85$. For lower wake energy ratio, the measured AMC increases slightly, but still falls close to each other for different propeller angle at the same η_w . This indicates that different propeller install angle does not significantly change wing pressure distribution to provide pitch moment augmentation in either direction.

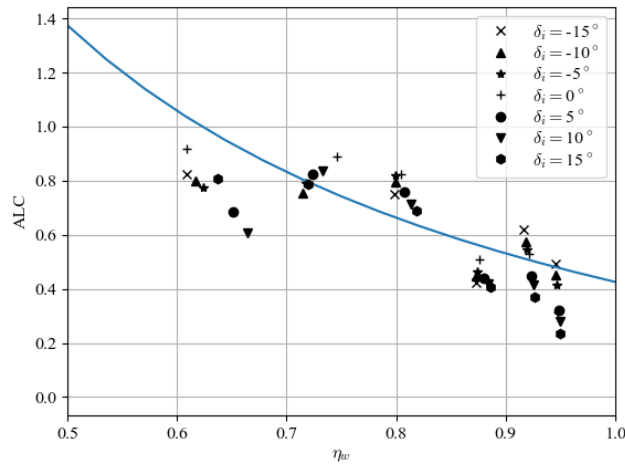


Figure 4.28: Augmented Lift Coefficient at $\alpha = 40^\circ$ for various δ_i

Figure 4.28 and Fig. 4.29 presents results for $\alpha = 40^\circ$. As observed before, the experimental data don't follow closely the theoretical trend line, although data points at different δ_i fall in a concentrated area. For $\eta_w \leq 0.85$ ALC falls within a range of $[0.6, 0.9]$.

On the right, in Fig. 4.29, the measured AMC again fall closely to each other, suggesting little influence of propeller install angle on moment augmentation. The overall trend however becomes a slight augmentation in pitch down direction at lower η_w .

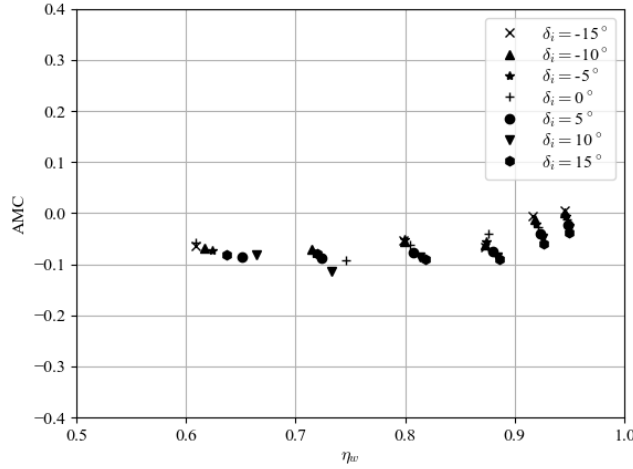


Figure 4.29: Augmented Moment Coefficient at $\alpha = 40^\circ$ for various δ_i

The lack of propeller install angle influence on the pitch moment augmentation effects doesn't mean that aircraft pitch characteristics stay the same at different δ_i . As thrust line changes with propeller orientation, a moment arm could exist between thrust line and centre of mass. Therefore propeller install angle has a direct effect through thrust on aircraft pitch characteristics despite having little influence on propeller-wing interactions.

4.6.4 Effect of vertical displacement

Another parameter that was investigated is the vertical position of propeller relative to the wing. Figure. 4.30 and Fig. 4.31 present augmented lift and moment coefficients at $\alpha = 10^\circ$ for various z_p . Small scatter appears around the theoretical trend line, particularly for all lower propeller positions and positive $z_p = 0.109D_p$, with the higher position reaching slightly larger ALC. Large difference exists between $z_p = 0$ and $z_p = 0.218D_p$. The highest propeller positions gives significantly lower ALC at $\eta_w = 0.86$ and 0.52 . The weaker augmentation effect might suggest that the lifting surface falls out of the influence region of propeller wake.

Moment characteristics isn't significantly changed by propeller wake effect, as indicated by the close scatter of points around $AMC = 0$ in Fig. 4.31.

Figure. 4.32 and 4.33 demonstrate the situation at $\alpha = 40^\circ$. The reduction in ALC is more prominent for the highest propeller position $z_p = 0.218D_p$. The value stays low for the entire η_w range. For the lower $z_p = 0.109D_p$, ALC is able to stay at high value until $\eta_w < 0.7$, where it falls from around 0.73 at $\eta_w = 0.72$ to 0.41 at $\eta_w = 0.6$. The increased freestream convection from higher V_∞ forces the propeller wake to follow closer with upstream flow, and thus it starts to depart the wing surface.

AMC in Fig. 4.33 falls closely to a slight negative value, which indicates that z_p doesn't

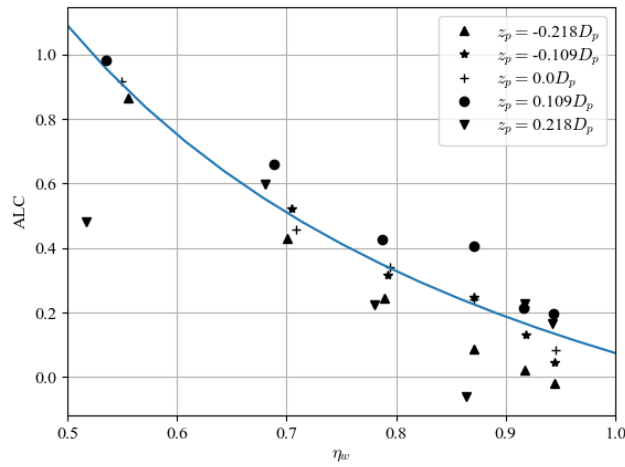


Figure 4.30: Augmented Lift Coefficient at $\alpha = 10^\circ$ for various z_p

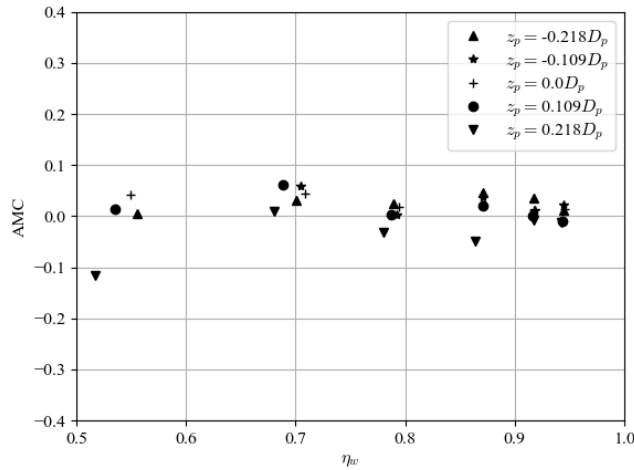


Figure 4.31: Augmented Moment Coefficient at $\alpha = 10^\circ$ for various z_p

have strong influence on wing pitch moment augmentation at this high α case. Hence propeller vertical displacement z_p principally influence aircraft pitch characteristics through thrust line offset, which changes moment arm to the centre of mass.

4.7 Conclusion

A comprehensive experimental study on aerodynamic lift and moment performance on a blown wing configuration has been presented. The design of experiment allows for easy modification of configuration parameters : flap deflection, propeller install angle and vertical

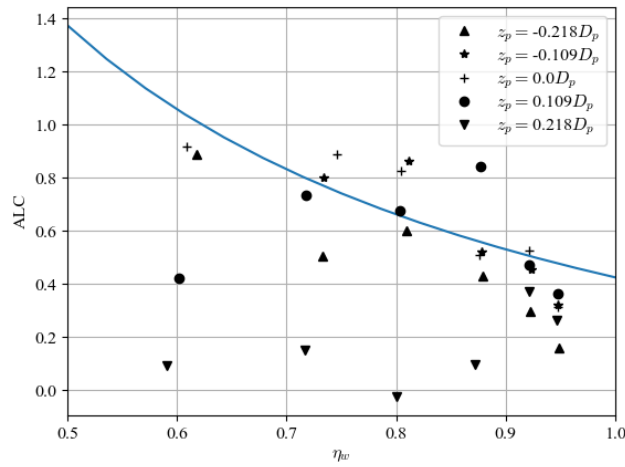


Figure 4.32: Augmented Lift Coefficient at $\alpha = 40^\circ$ for various z_p

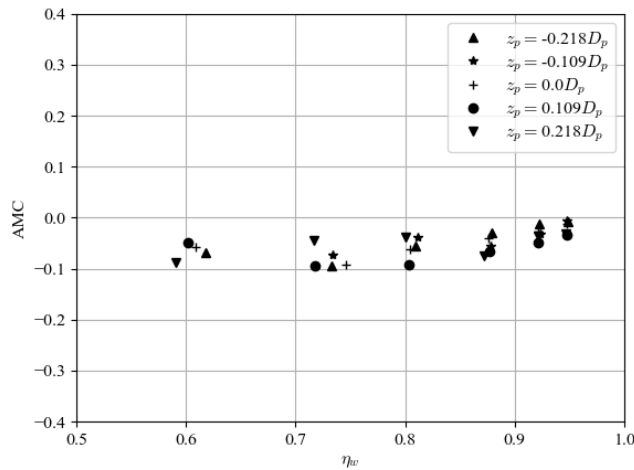


Figure 4.33: Augmented Moment Coefficient at $\alpha = 40^\circ$ for various z_p

position. Separate balance measurements allows for comparison of propeller augmentation effects based on measured thrust condition.

A new set of augmented aerodynamic coefficients is defined for comparison of propeller wake effects at different freestream and thrust conditions. Lift augmentation effect is thus related to a wake energy ratio.

The results revealed significant lift augmentation for a lifting surface. The effect is angle of attack dependent. At lower angle of attack, circulation induced lift component appears to be constant for high wake energy ratio, whereas this component becomes variable at higher angle of attack. Negative propeller install angle or higher propeller positions tend to slightly

increase this augmentation effect, although mounting the propeller too high ($\approx 0.2D_p$) may cause wing surface move out of propeller wake.

Augmentation in pitch moment was also observed. At low angle of attack, propeller wake effect only amplifies zero-lift pitch moment through thrust loading. At higher angle of attack, there exists a critical wake energy ratio, below which the propeller wake can no longer augment wing pitch moment. Propeller install angle and vertical position don't appear to have a significant influence on wing pitch moment, although the offset of propeller thrust line may create additional pitch moment.

Propeller-Wing Aerodynamic Interaction Model

Contents

5.1 Numerical Formulation	97
5.1.1 Non-linear lifting line model	98
5.1.2 Wake deformation model	100
5.1.3 Swirl reduction model	101
5.2 Comparison with experimental results	102
5.2.1 Clean configuration	102
5.2.2 Effect of different angles of attack	104
5.3 Conclusion	105

Author's Contributions

Publication in progress

Y. Leng, T. Jardin, M. Bronz, J.-Marc Moschetta, "Experimental Analysis of a Blown-wing Configuration during Transition Flight", *ICAS 2021 Congress*, Shanghai, China, Sept. 6-10, 2021.

5.1 Numerical Formulation

The results were further compared with a modified version of non-linear lifting line model MachUp [Goa18] developed by the aeronautics department in University of State Utah to identify the potential application of such method in convertible UAV designs. Non-linear lifting line model has shown great potential in predicting near and post stall behaviour in recent year [PSL18]. Instead of linearised coefficients, these newer methods utilise tabulated 2D airfoil polar. These data can be obtained from either experimental or computational method.

Although detailed implementation of the lifting line model was well documented in [Goa18], a brief introduction of the algorithm and descriptions of the major modifications are presented in this section, followed by comparisons with experimental results.

5.1.1 Non-linear lifting line model

The MachUp library was developed based on derivation of linear lifting line theory in [Phi04] to calculate lift, drag and moment. The formulation allows multiple lifting surfaces definition. Each lifting surface is made up of several trapezoidal wing segments, which are further discretised to individual panels, as shown in Fig. 5.1.

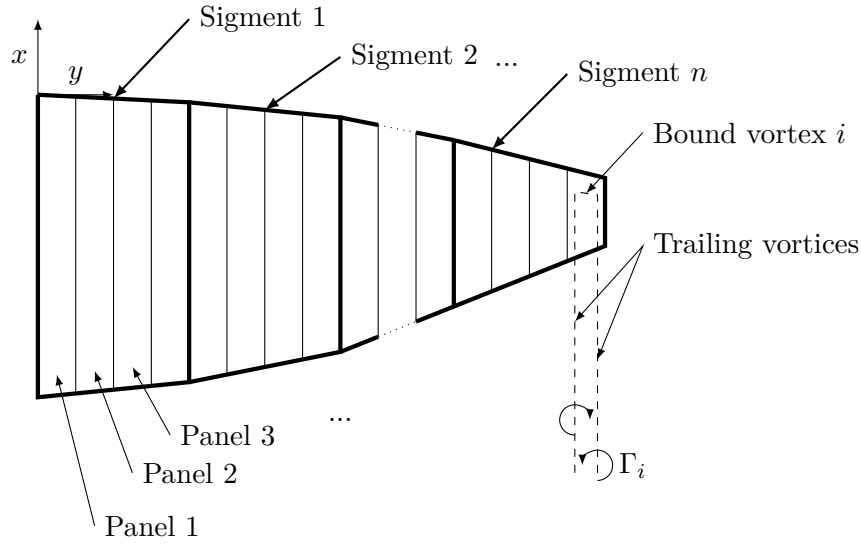


Figure 5.1: Lifting surface panels

At each panel i , a horseshoe vortex system is modelled with constant circulation Γ_i . The bound vortex segment aligns itself with the panel's quarter chord line; semi-infinite trailing vortices stretch downstream in the freestream direction.

The vortex system is solved from Kutta-Jukowsky theory at control point i of each panel, which is designated at the quarter chord position. The boundary condition at control point i is shown in Eq. 5.1.

$$2 \left| \left(\vec{V}_\infty + \sum_{j=1}^N \vec{v}_{ji} \Gamma_j \right) \times \vec{\zeta}_i \right| \Gamma_i - V_\infty^2 \tilde{C}_{L,i}(\alpha_i, \delta_i) = 0 \quad (5.1)$$

where $\tilde{C}_{L,i}$ is the sectional lift coefficient as a function of angle of attack α_i and flap deflection δ_i , $\vec{\zeta}_i \equiv \frac{\Delta \vec{l}_i}{\Delta S_i}$ is the ratio between the bound vortex segment vector and the panel surface area.

Further \vec{v}_{ji} is the elementary velocity induced at point i from horseshoe vortex at panel j , as shown in Fig. 5.2. The elementary induced velocity is calculated from Biot-Savart law in Eq. 5.2.

$$\vec{v}_{ji} = \begin{cases} \frac{1}{4\pi} \left[\frac{\vec{u}_\infty \times \vec{r}_{j2i}}{r_{j2i}(r_{j2i} - \vec{u}_\infty \cdot \vec{r}_{j2i})} + \frac{(r_{j1i} + \vec{r}_{j1i} \times \vec{r}_{j2i})}{r_{j1i}r_{j2i}(r_{j1i}r_{j2i} + \vec{r}_{j1i} \cdot \vec{r}_{j2i})} - \frac{\vec{u}_\infty \times \vec{r}_{j1i}}{r_{j1i}(r_{j1i} - \vec{u}_\infty \cdot \vec{r}_{j1i})} \right], j \neq i \\ \frac{1}{4\pi} \left[\frac{\vec{u}_\infty \times \vec{r}_{j2i}}{r_{j2i}(r_{j2i} - \vec{u}_\infty \cdot \vec{r}_{j2i})} - \frac{\vec{u}_\infty \times \vec{r}_{j1i}}{r_{j1i}(r_{j1i} - \vec{u}_\infty \cdot \vec{r}_{j1i})} \right], j = i \end{cases} \quad (5.2)$$

When $j \neq i$, the elementary velocity consists three terms : the first and third terms are influences from the trailing vortices and the middle term is induced from the bound vortex. When $i = j$, the middle term is zero since the control point lies on the bound vortex.

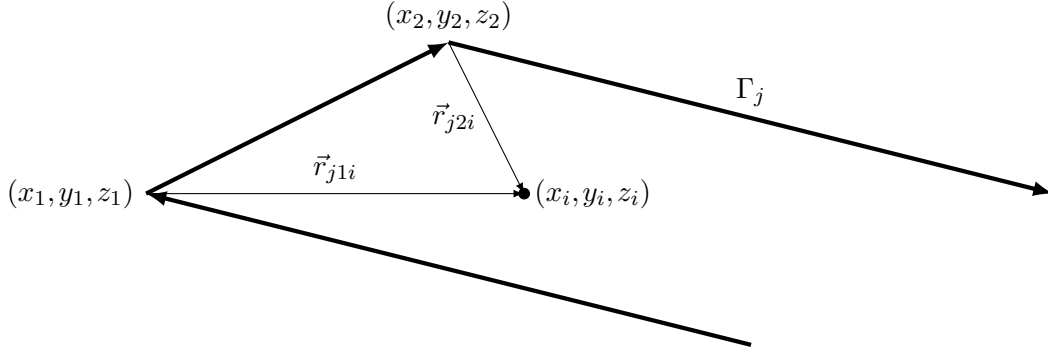


Figure 5.2: Horseshoe vortex

Equation 5.1 can be further simplified by assuming small angle of attack and neglecting higher order terms. These assumptions helped with rapid calculation and robust convergence. A linear system of the bound circulation is derived in Eq. 5.3.

$$2|\vec{V}_\infty \times \vec{\zeta}_i| \Gamma_i - V_\infty \tilde{C}_{L,i\alpha} \sum_{j=1}^N \vec{v}_{ji} \cdot \vec{u}_{ni} \Gamma_j = V_\infty^2 \tilde{C}_{L,i\alpha} (\vec{u}_\infty \cdot \vec{u}_{ni} - \alpha_{0i} + \epsilon_i \delta_i) \quad (5.3)$$

where $\tilde{C}_{L,i\alpha}$ is the sectional lift line slope of airfoil at panel i , \vec{u}_∞ and \vec{u}_n is the unit vector in freestream and normal direction, α_{0i} is zero-lift angle of attack at panel i and ϵ is flap efficiency.

However, for the flight conditions encountered by VTOL aircraft, elevated angle of attack is expected. Therefore a modification has to be made to use the non-linear implementation of lifting line model in Eq. 5.1. The modification was necessary to overcome small angle assumptions associated with the original linear version.

The non-linear lifting line model was implemented with Newton-Raphson iteration. The solution time depends heavily on initial solution, but still fast enough for preliminary design purposes. However a relaxation factor is necessary to ensure convergence. Most successful results were obtained for relaxation factor around 0.8, but divergence can still occur in near-stall and stall condition.

Furthermore, to truly overcome the small angle of attack assumption, airfoil characteristics at high angle of attack must be taken into consideration. These data are usually obtained from

wind tunnel test as numerical solutions for separated flow involves expensive methods such as detached eddy simulation (DES) or large eddy simulation (LES), and thus the data aren't easily available except for a selected studied airfoils ([SK81]). For these airfoils, an option was created to allow reading tabulated data to interpolate lift, drag and moment coefficients according to effective angle of attack and sectional Reynolds number. The other option is to use empirical formulae such as in [Hoe01] or [Bia+16], which is rather practical as post-stall airfoil characteristics are less dependant on airfoil geometry.

Results obtained from the non-linear lifting line model and the new airfoil characteristics routine were compared over a clean wing configuration with experimental data and lifting line model from XFLR5 in section 5.2.1.

With the aerodynamic model capable to calculate high angle of attack condition, two further modifications were made to correctly present boundary condition for resolving sectional aerodynamic load. These modifications are presented in the following sections.

5.1.2 Wake deformation model

Original propeller wake was extended downstream along rotation axis as a straight cylinder. The wake model was then used to calculate immersed wing control points where propeller induced velocity needed to be included in lifting line model. Therefore, the accuracy of lifting line calculation depends on correct wake position.

The earlier model however fails to take freestream convection into consideration. In reality, as forward flight speed increases, the wake streamtube will be "skewed" or displaced in direction perpendicular to rotation axis. This phenomenon is illustrated in Fig. 5.3, as tip blade vortices of a forward flying helicopter were visualised by background-oriented schlieren (BOS) method.

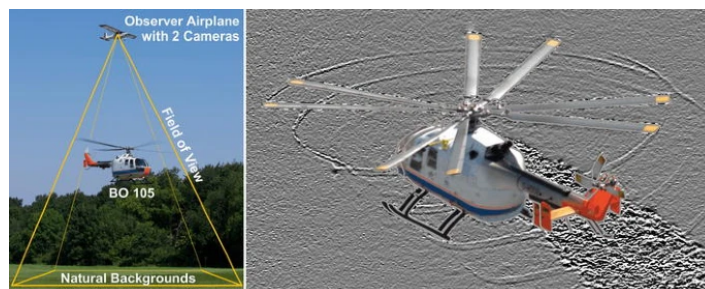


Figure 5.3: Blad tip vortices visualised from background-oriented schlieren (BOS) method

The angle between ultimate slipstream axis and the rotational axis is referred to as wake skew angle χ . χ can be accurately estimated from momentum theory [Lei06]; [Joh12].

In Fig. 5.4, a side-view illustration of the wake displacement is presented.

Downstream of the propeller disk, the flow component constitutes two components :

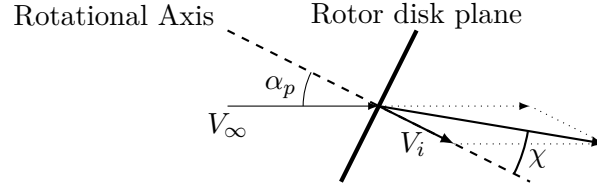


Figure 5.4: Wake Skew Angle

1. Freestream V_∞
2. Induced velocity V_i

V_i is supposed to be aligned with rotation axis since the normal force on disk plane is usually one order of magnitude smaller than thrust. The skew angle χ is thus originated from the freestream component perpendicular to rotation axis. Thus the ultimate wake skew angle is found

$$\chi = \arctan \frac{V_\infty \sin \alpha_p}{V_\infty \cos \alpha_p + V_i}$$

The wake skew angle is assumed to be established immediately downstream disk plane, and its direction \hat{i}_w is used to determine wing immersed points, where for a given point A

$$|\vec{r}_{w,A}| = |(\vec{r}_A - \vec{r}_{O_p}) \times \hat{i}_w| \leq R_p$$

where O_p is the center of propeller, R_p is propeller radius and \vec{r} is the position vector to respective point.

5.1.3 Swirl reduction model

Once identified as immersed wing points, the boundary condition for solving the non-linear lifting line method is altered at these control points. The original implementation of lifting line theory follows its form in chapter 1.9 of [Phi04] as Eq. 5.4.

$$2 \left| \left(\mathbf{u}_\infty + \sum_{j=1}^N \mathbf{v}_{ji} G_j \right) \times \zeta_i \right| G_i - \tilde{C}_{Li}(\alpha_i, \delta_i) = 0 \quad (5.4)$$

$$\mathbf{u}_\infty \equiv \frac{\mathbf{V}_\infty}{V_\infty}, \quad \zeta_i \equiv \bar{c}_i \frac{d\mathbf{l}_i}{dS_i}, \quad G_i \equiv \frac{\Gamma_i}{\bar{c}_i V_\infty}$$

where \mathbf{v}_{ji} is the induced velocity at point i induced by a unit circulation at point j , G_j is normalised circulation, ζ_i is normalised spanwise length vector and \tilde{C}_{Li} is sectional lift coefficient at section i .

For immersed wing points, the velocity term needs to include the propeller induced velocity, thus :

$$2 \left| \left(\mathbf{u}_\infty + \sum_{j=1}^N \mathbf{v}_{ji} G_j \right) \times \zeta_i + \mathbf{u}_{wi} \right| G_i - \tilde{C}_{Li}(\alpha_i, \delta_i) = 0 \quad (5.5)$$

$$\mathbf{u}_{wi} \equiv \frac{\mathbf{V}_{i,i}}{V_\infty}$$

where $\mathbf{V}_{i,i}$ is the propeller induced velocity at section i . The induced velocity is composed of two terms : the tangential and axial components, written in general form in Eq. 5.6.

$$\mathbf{V}_{i,i} = \epsilon_t \mathbf{V}_{it,i} \hat{i}_t + \epsilon_a \mathbf{V}_{ia,i} \hat{i}_w \quad (5.6)$$

where ϵ_t, ϵ_a are tangential and axial swirl reduction factors; \hat{i}_t and \hat{i}_w are tangential and axial unit vector in propeller wake at control point of section i .

The tangential and axial velocities \mathbf{V}_{it} and \mathbf{V}_{ia} are calculated from a propeller wake model derived from turbulent jet solutions [Goa18]. Direct application of the tangential velocity however would cause significant stability issues. After testing, the spanwise component of tangential velocity was ignored and the reduction factors were fixed to be :

$$\epsilon_t = 0.075; \quad \epsilon_a = 1. \quad (5.7)$$

5.2 Comparison with experimental results

The non-linear lifting wing method was compared with experimental results over the identical propeller wing configuration.

The lifting line model could include the main wing and propeller panels. The main wing was discretised into 40 panels distributed in cosine law per semi-span and propeller contained 35 panels per blade, as shown from the generated STereoLithography file in Fig. 5.5.

The propeller model may be removed to simulate a clean wing. Trailing edge flap can be added on the main wing but wasn't studied in the current research.

5.2.1 Clean configuration

According to previous discussion, an accurate estimation of aerodynamic augmentation effect is based on a good knowledge of power-off conditions (the base \tilde{C}_L, \tilde{C}_D and \tilde{C}_M). To better understand the capability of the modified MachUp code, calculations were performed for the experimental model over wide range of angles of attack and were compared with measured aerodynamic loads.

The experimental data of clean configuration at 10m/s windtunnel speed were extracted

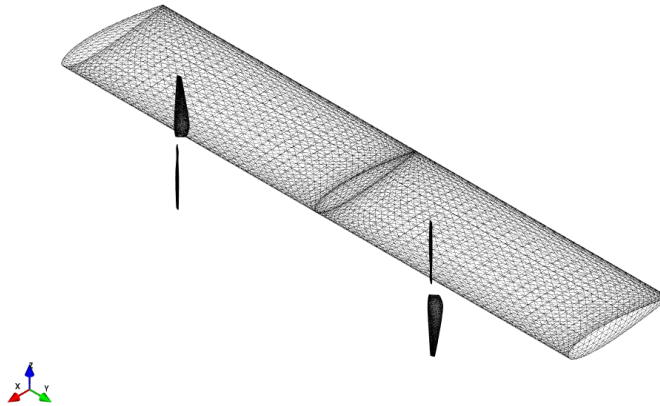


Figure 5.5: Non-linear Lifting Line Model for Propeller and Wing Configuration

and used for comparison. The maximum angle of attack tested was at 40° . Two cases were performed without rotating the propeller and the entire propeller assembly was removed in one of them. The results were presented in Fig. 5.6 and Fig. 5.7, where black dots mark the case with idle propeller and blue marks represent the case without propeller. The angle of attack range allows observation of pre-stall linear regime ($\alpha \leq 10^\circ$), stall regime ($10^\circ < \alpha < 25^\circ$) and post-stall regime ($\alpha \leq 25^\circ$).

According to Fig. 5.6 and Fig. 5.7, the presence of propeller doesn't have significant impact in linear regime and post-stall regime, where the data points fall close by. The difference in stall regime is difficult to conclude due to the sensitivity of flow separation to external disturbances, but in application the aircraft should stay minimum time in this phase and thus the impact on performance estimation is negligible.

Results from two numerical models were presented. The solid line is calculated from the linear lifting line model in XFLR5. The calculations were performed up to 15° where the model had difficulty to converge. The dashed line is obtained from the current non-linear lifting line model. Both models performed well in the pre-stall domain, with accurate prediction of lift and pitch moment coefficients and sufficient estimation of drag coefficient.

In Fig. 5.6, it can be observed that the models have different behaviour in stall regime. The linear model tends to continue at the same lift line slope and thus fails to capture stall onset, which is the expected behaviour of linear model. The non-linear lifting line model however does capture the sudden decrease in lift coefficient but with a more gentle behaviour than the experimental case. The minimum lift coefficient of 0.58 was calculated at 27° during stall, while the measured value was about 0.45 at 15° . The lift coefficient calculation seems to be close to experimental data above 30° and predicted a second local maximum between 40° and 50° angle of attack.

The drag polar in Fig. 5.7 confirms a similar trend in model behaviour, where quasi-

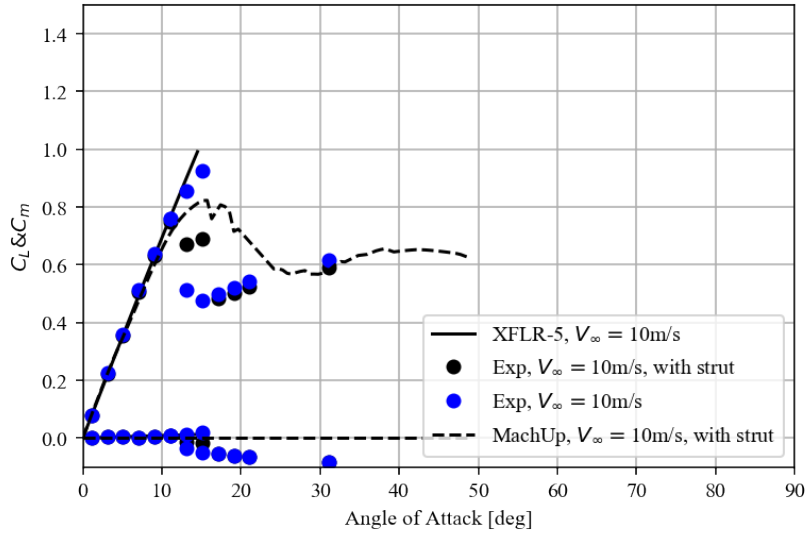


Figure 5.6: Clean Configuration Lift and Pitch Moment Coefficient

quadratic growth of drag coefficient as a function of lift coefficient was predicted by both linear and non-linear models. The linear model underestimate drag coefficient prior to stall onset, while the non-linear model gives better estimation. In the stall regime, the discrepancy between non-linear calculation and experimental data are mainly due to the overestimated lift coefficient.

Comparison with experimental data in clean configuration has demonstrated the accuracy of the modified non-linear lifting line method. The method is capable to predict accurately the model's aerodynamic performance in linear regime. While stall behaviour remains difficult to be captured accurately, the degraded performance and post-stall regime are intrinsically included in the calculation, which alleviates numerical convergence issues in these conditions. Caution should be taken while examining vehicle performance using the current method.

5.2.2 Effect of different angles of attack

When the propeller model is introduced, the lift distribution varies significantly around the slipstream immersed area. Its global effect can be characterised through the aforementioned augmented aerodynamic coefficients.

The augmented lift coefficient calculated for 0° , 10° and 30° angles of attack is presented in Fig. 5.8. Different color differentiates angle of attack. The calculations were performed over different tip speed ratios in $[0.1, 0.15]$ with fixed propeller speed at 6000rpm .

The angles of attack were selected to represent low to moderate and post-stall angle of attack ranges. By comparing the number of successfully convergence, the code is observed to be more robust at lower to moderate angles of attack while several post-stall flight conditions cannot reach convergence.

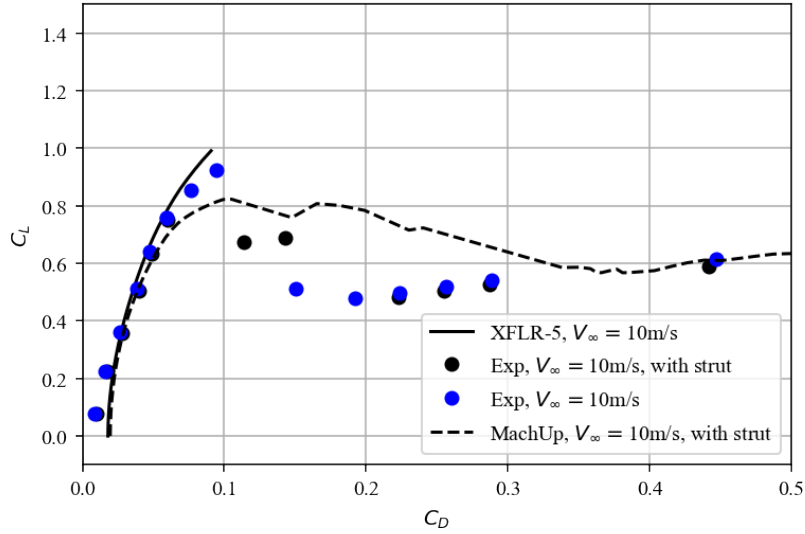


Figure 5.7: Clean Configuration Drag Polar

For the obtained results, the low angle of attack result predicted limited lift augmentation, as the flow condition over the wing is completely symmetrical.

At $\alpha = 10^\circ$, lift augmentation effect is more pronounced. Near hover condition where $\eta \approx 1$ is numerically unstable due to low Reynolds number over large part of the wing and significant angle of attack variations within immersed wake region.

The converged results generally follows the inversely proportional trend suggested before but has a noticeable drop for $\eta < 0.55$. This likely caused by the alignment of slipstream axis with freestream direction as discussed in section 5.1.2. The deformation model didn't take the influence of wing in calculating the displacement of slipstream longitudinal position and thus the slipstream probably rises relative to the wing at a greater rate respective to freestream speed than the actual case. Therefore the wing encounters the bottom half of slipstream at smaller wake energy ratio.

The maximum lift augmentation effect is observed near $\eta = 0.6$.

The algorithm is highly unstable near stall angle of attack, and thus no credible results were obtained at $\alpha = 20^\circ$.

However the post-stall results at $\alpha = 30^\circ$ lie closely with experimental results.

5.3 Conclusion

A numerical lifting line method based on MachUp library was selected to model the interaction between lifting surface and propeller. The original model was formulated as a linear system of equations for bound circulations. However, the model had to be expanded in order to be

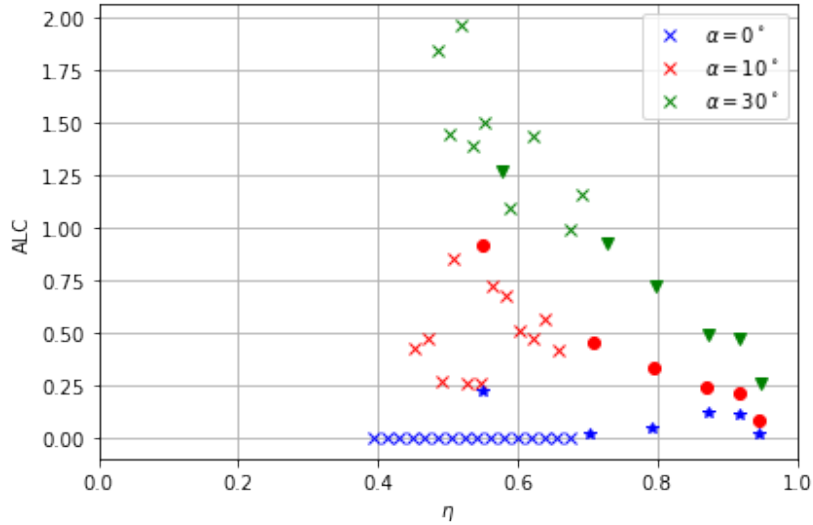


Figure 5.8: Calculated ALC for various angles of attack

used for transition flight condition. High angle of attack invalidates the assumptions of a straight propeller slipstream, linearised 2D aerodynamics and horseshoe vortex system.

To estimate the slipstream deflection, momentum method was applied to the slipstream centreline. The wing immersed points were identified accordingly using the deflected centreline direction. The propeller performance was also further modified using the high incidence correction developed in chapter 3.

The aerodynamic coefficients C_L , C_D and C_m of a 2D airfoil can be defined using table lookup method. The major limitation of this method is its dependence on the availability of experimental data of chosen airfoil. An alternative method could be a transition into flat plate empirical formulae.

The equation system for bound vortices were taken in the original non-linear form and a Newton-Raphson method was used to solve the system.

The revised aerodynamic model was validated against clean configuration data and found to be equally robust and slightly more accurate.

When propeller slipstream was included, it was observed that the tangential velocity could create numerical instability, and a swirl reduction factor must be applied, and was fixed to be $\epsilon_t = 0.075$. This was determined likely to be a combination of slipstream deformation observed in chapter 4 and the specific tangential velocity profile within slipstream. The model was found to be in agreement with experimental data for angle of attack under 10° or above stall angle of attack 20° at moderate wake energy ratio.

Mission-based Long Endurance Convertible UAV Design

Contents

6.1	Introduction	107
6.1.1	Background	107
6.1.2	State of the Art	108
6.2	Development of Optimization Tool and Disciplines	112
6.2.1	Aircraft definition module	112
6.2.2	Mass and balance module	113
6.2.3	Structural module	116
6.2.4	Flight phase analysis	118
6.3	Optimization Problem	120
6.3.1	Problem Setup	120
6.3.2	Test Cases Setup	127
6.3.3	Results and discussions	128

Author's Contributions

Publication in preparation

K. Fayez, Y. Leng, T. Jardin, M. Bronz, J.-Marc Moschetta, "Conceptual Design for Long-Endurance Convertible Unmanned Aerial System", *AIAA Applied Aerodynamics Conference, AIAA SciTech Forum*, virtually, United States, Jan. 11-15, 2021.

6.1 Introduction

6.1.1 Background

Based on the development of aerodynamic models in previous chapters, a rigorous assessment on different convertible UAV configurations over different mission profiles is conducted. Past

studies typically emphasize characteristics on a specific design, but a comprehensive study discussing how mission profile affects design choices is lacking.

Unlike large-scale aircraft design, UAV aerodynamic configuration is very much diversified and thus a clear way to match aircraft configuration with mission specifications is desired in view of past studies. To address the issue, a multidisciplinary optimization tool is developed based on OpenMDAO library to perform the preliminary aerodynamic design of a convertible drone.

The final methodology should be able to optimize several configurations of convertible UAVs and then compare them in terms of energy requirements for different flight phases. The tool performs a series of optimization loops taking into account important parameters such as the lifting surfaces and propulsive elements to ultimately design the most energy efficient configuration. This is to allow objective and quantifiable comparison between configurations, and thus promote further understanding on flight physics involved in VTOL aircraft.

6.1.2 State of the Art

This literature review attempts to identify, among the past significant studies on convertible UAV, the scope of possible configurations, the involved disciplines in design optimization and their level of fidelity, and finally the formulation of the optimization problem.

6.1.2.1 Mass and Balance

In a review conducted by Papageorgiou et al. on the advancements in MDO of aerial vehicles [Pap+18] it has been shown that the mass estimation discipline is the second most common discipline when it comes to aerial vehicles design. This is evident since vehicle mass is pivotal to the aerodynamic and performance calculations, which will ultimately be one of the most influential variables in the optimization [AGS18].

For a preliminary design, it is acceptable to use a low-fidelity mass model for the optimization using empirical formulas, statistical data and mass models whenever possible. This reduces time during mass estimation instead of using costly high-fidelity models such as data from CAD. Moreover review from Papageorgiou has shown that 77% of the aerial vehicle MDO use low fidelity mass models [Pap+18].

The mass estimation will be done by breaking down the UAV into components and estimating each of their mass. We define the total mass of the vehicle as follows:

$$m_{\text{total}} = m_{\text{payload}} + m_{\text{structure}} + m_{\text{energy}} + m_{\text{propulsion}} \quad (6.1)$$

The detailed mass breakdown is as follows:

- m_{payload} : avionics and/or miscellaneous payload.
- $m_{\text{structure}}$: lifting surfaces and fuselage structure.
- m_{energy} : battery or fuel cell system mass.
- $m_{\text{propulsion}}$: propulsive group containing electric motors, electronic speed controllers and propellers.

As will be specified in section 6.2.2, empirical formulae are used for the propeller based on the diameter, chord of and material density of the propeller. For the ESC and motors a linear model based on certain parameters of the components such as amperage rating or dimensions is developed. For the batteries an empirical formula based on the specific energy consumption of the battery. For the non-lifting surfaces such as fuselage or nacelle, a volumetric approach with the density of the material is used to estimate the weight. For the lifting surfaces such as the wings, a formula based on a volumetric approach of the components of the wing is used.

6.1.2.2 Structural Analysis

Papageorgiou et al. also found that the structural analysis was present in 66% of the studies and was the third most common discipline [Pap+18]. In the context of the current optimization problem, the structural analysis is chosen to be applied only to the wing spars, to ensure the structural integrity of the wing in the most severe flight conditions defined by maximal normal load factor. This is done by sizing the spar to withstand the required constraints. Moreover it allows increases mass estimation fidelity, since the mass of spar is fed back to mass model. The structural model is simplified to a low fidelity model, consisting a cantilever beam under elliptical load distribution. The details of the model are presented in Section 6.2.3. In future applications the outputs of this simple structural model could be used to allow more complex dynamic aeroelastic computations.

6.1.2.3 Aerodynamics and Stability

In the same review done by Papageorgiou et al. [Pap+18], they found that 52% of the aerodynamics models used in MDO were reduced order models (Panel codes), 11% medium resolution (Euler Solvers or coarse CFD simulations) and 37% high resolution (Full CFD simulation).

The wide use of reduced order models is a practical choice. In the preliminary design phase, large combination of design variables is necessary, which requires robust and efficient algorithms. On the other hand, the goal of preliminary design is to obtain general aircraft size while neglecting configuration details and thus the requirement on accuracy can be relaxed. Furthermore when considering the aerodynamics of a convertible UAV, there are very different flight conditions that the aircraft will encounter from the VTOL phase, through transition, to horizontal flight. As mentioned before, such aerodynamic tool box must be able to handle unusual attitude and different combinations of propulsion and lifting surface combinations.

Computational cost and time required for high resolution model to analyse these conditions are usually undesired in this design stage. In conclusion, the choice of using reduced order models is a compromise of computational cost, robustness and the requirement of precision.

The enhanced Machup library [Goa18] is such a suitable low-fidelity aerodynamic model. The model has been validated at ISAE [Len+20], and it has been improved to take into account high-angle of attack computations, based on findings from the dedicated wind tunnel experiment. This allows more accurate aerodynamic estimation at a still affordable computational cost.

6.1.2.4 Electric Propulsion

For the current application, electric propulsion is the selected method of propulsion. In most applications of UAVs above 100g brushless DC motors are used [Bic+20]. A propulsion group is defined to consist of: a propeller, a motor, an electric speed controller (ESC). The propulsion group is presented in Fig. 6.1, where the set point from the flight controller is the input to the group, and thrust is the output.

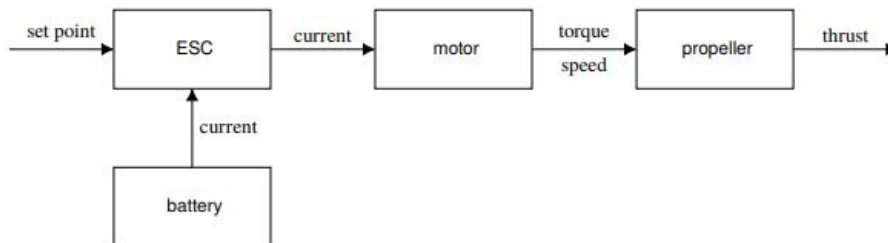


Figure 6.1: Multirotor Propulsion Group [Bic+20]

In the context of this optimization, the electric propulsion optimization would be advantageous to have since there exists a multitude of propulsion groups in VTOL UAVs. This optimization can be achieved by performing propeller-motor matching. This concept revolves around finding the optimal efficiency for a combination of a motor and propeller for a given flight mission. QOPTIMIZER is a tool developed for this specific purpose [BMH12]. It has two main capabilities. The first one is matching the most appropriate motor and propeller combination for defined mission requirements. This is based on a database of propellers and motors. The second capability is designing the best propeller using a match from the motor database. The workflow of QOPTIMIZER is presented in Figure 6.2.

However for the current optimization problem, QOPTIMIZER has not been implemented yet and is planned for in future work.

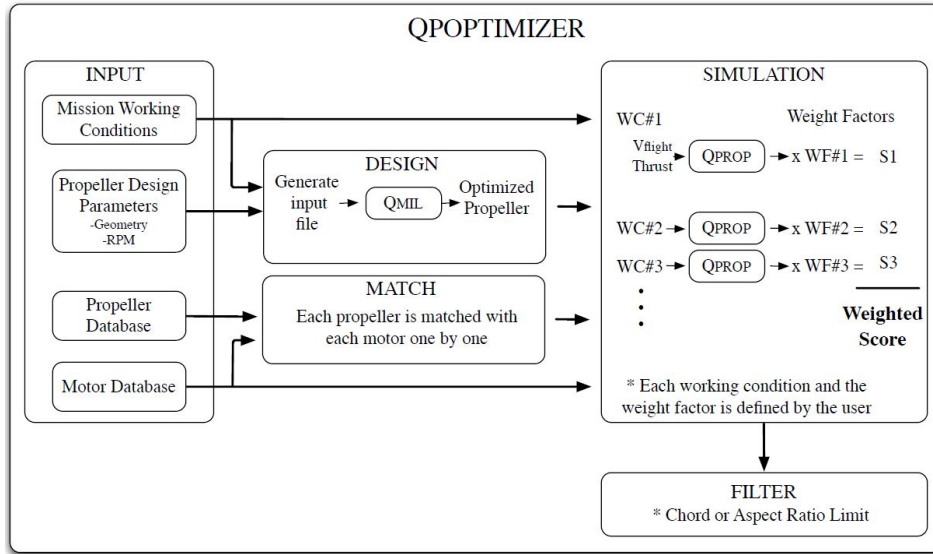


Figure 6.2: Main Flow chart of QOPTIMIZER program [BMH12]

6.1.2.5 Optimization Algorithm

Among current multi-disciplinary optimization researches, OpenMDAO is typically used to formulate problem and manage data exchange [Gra+19]. It is an open source, high performance platform that manages model hierarchy and assembles optimisation problems. It interacts with the Scipy optimisation module which provides the optimisation algorithms. For the type of problem presented in this paper, a constrained minimization or maximization of multivariate scalar function, the following optimisation algorithms are available to use:

1. Trust-region constrained algorithm (trust-constr) : must provide either Jacobian or Hessian matrix, the other could be approximated using finite differentiation.
2. Sequential least squares programming (SLSQP) : uses quadratic programming to determine search direction, supports equality / inequality constraints.
3. Constrained optimization by linear approximation (COBYLA) : solving approximated linear programming problems, no gradient required, only supports inequality constraints.
4. Genetic algorithm : gradient free method, supports both equality and inequality constraints.

Since the inputs to the optimization are user selected parameters (range, duration etc) of the different flight phases, it is highly likely that equality and inequality constraints are needed. The SLSQP algorithm in OpenMDAO was thus chosen to be an initial driver to construct the optimisation structure. In the future, other optimisation drivers such as genetic algorithm could be used to further study the different methodologies.

6.2 Development of Optimization Tool and Disciplines

6.2.1 Aircraft definition module

The design parameters available for aircraft definition are listed in Table 6.1.

Symbol	Description	Unit
S	Wing surface area	$[m^2]$
AR	Wing Aspect Ratio	$[-]$
λ	Wing taper ratio	$[-]$
Φ	Wing sweep angle	$[^\circ]$
R_{cruise}	Cruise propeller radius	$[m]$
R_{VTOL}	VTOL propeller radius	$[m]$
β_{cruise}	Cruise propeller pitch	$[^\circ]$
β_{VTOL}	VTOL propeller pitch	$[^\circ]$
E_{bat}	Battery capacity	$[Wh]$

Table 6.1: Design Parameters

Depending on the selected configuration, the aircraft definition module is set up accordingly with initial default values of component locations and dimensions to build the configuration. The different possible configuration are shown as a reference in Fig. 6.9. The aircraft definition comprises four sub-dictionaries:

1. Lifting surfaces : for each lifting surface only one segment is allowed at the moment and the following properties are specified.
 - location of root section leading edge.
 - span.
 - root chord.
 - tip chord.
 - dihedral angle.
 - sweep angle.
 - airfoil or airfoil sets.
 - spanwise panel number.
2. Bodies : the current module allows only streamlined body with cylindrical mid-section.
 - location of centre.
 - length.
 - diameter.
 - material density.

3. Payloads : point mass that does not have aerodynamic effect.

- mass.
- location of centre of gravity.
- constant electrical power consumption.

4. Propulsion groups : each propulsion group consists a motor, an ESC and a propeller.

- location of propulsion group (propeller centre).
- orientation of propeller.
- flight phase that the propulsion group is used (either VTOL, cruise or both).
- propeller diameter.
- propeller pitch and chord laws.
- propeller airfoil.
- propeller blade number.
- brushless motor mass or rating.
- ESC mass or rating.

The aircraft definition parameters are used by the mass and balance module to determine the center of gravity of the aircraft as well as the mass of all the components of the aircraft.

6.2.2 Mass and balance module

From Equation 6.1, the aircraft mass is decomposed into four terms : 1) structural ; 2) propulsion ; 3) battery and 4) payload. Each defined element allows for mass information definition. These elements are typically treated as point mass defined by specifying mass and the location of centre of gravity. Depending on application, some of these entries are calculated automatically.

The payload mass is expected to be given by the user, and was fixed to be $2.0kg$ in the current study.

The structural mass differs between lifting surface and bodies. Mass information of lifting surfaces is implied from its MachUp wing segment specification which contains its span, root chord, tip chord and relative thickness. The wing segment is considered to be a trapezoid plate with the same thickness. A global density is specified for all lifting surfaces. The mass of wing segment i is thus found to be the following.

$$m_{w,i} = \frac{\rho_w}{2} (c_{\text{root},i} + c_{\text{tip},i}) \tau b_i \quad (6.2)$$

For non-lifting bodies, only cylindrical shell is considered. Each body object is defined by its length L_b , outer radius R_b and thickness τ_b . Density is also allowed to be specified

individually, otherwise a default global value is used. The mass of body i is found to be the following.

$$m_{b,i} = \rho_{b,i} \pi R_{b,i} \tau_{b,i} L_{b,i} \quad (6.3)$$

Propulsion mass contains propeller, ESC and motor mass. Currently, the ESC and motor weight model has been implemented by taking the specifications of 26 off-the-shelf Turnigy models from Hobbyking catalogue. Estimation of motor and ESC mass could be made [Gat17]; [BHJ16]. A linear regression was performed for ESC mass over the rated constant current with with $R^2 = 0.81$. The results are presented in Fig. 6.3. The coefficient of determination value is not a perfect fit, but without specific information, it significant enough to be used as initial guess for a low fidelity model. Further, the models were compared with the linear model in [Gat17], represented by the orange line in Fig. 6.3, and is shown in good agreement from the previous study. There is also the option to specify the specific mass of the ESCs if the user has a good idea of the weight of the ESCs needed for the preliminary design of the UAV. In the future this model could be further improved by determining the required current draw of the motor and sizing the ESCs accordingly.

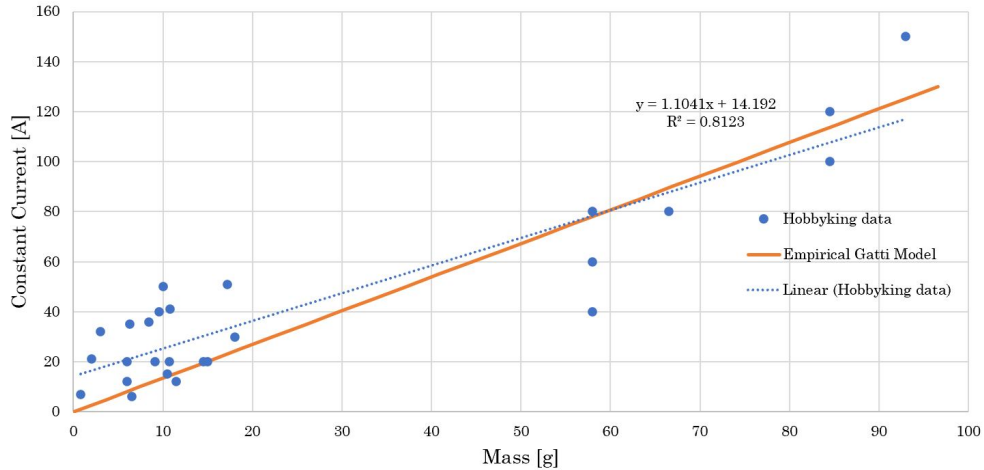


Figure 6.3: ESC Constant Current vs Mass Model

The regression model for the motor mass as a function of max current rating could not be valbut idated with reference due to limited data, however for a low fidelity mass model, the obtained power regression shown in Fig 6.4 was retained. As an alternative, the motor mass could also be estimated using K_V specification, as in [Gat17] shown in Fig. 6.5. As the case for the ESCs if a specific motor model is known, its mass can be set as constant in the optimisation. Similarly to further improve the fidelity of the motor mass model, the max current rating can be directly driven from the motor requirements derived from the aerodynamic module.

Propeller mass is estimated using empirical formula derived from available commercial catalogue of Aeronaut propellers [Pro]. For each propeller i ,

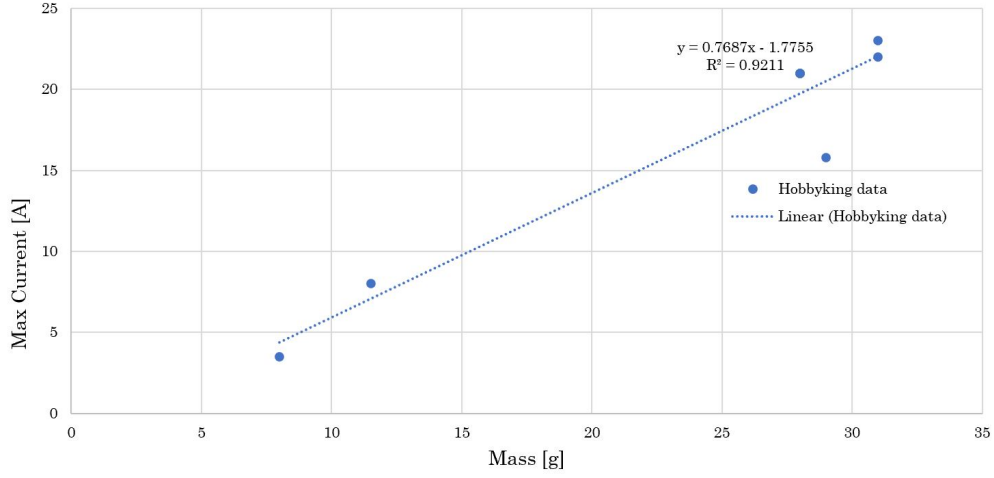


Figure 6.4: Motor Max Current vs Mass Model

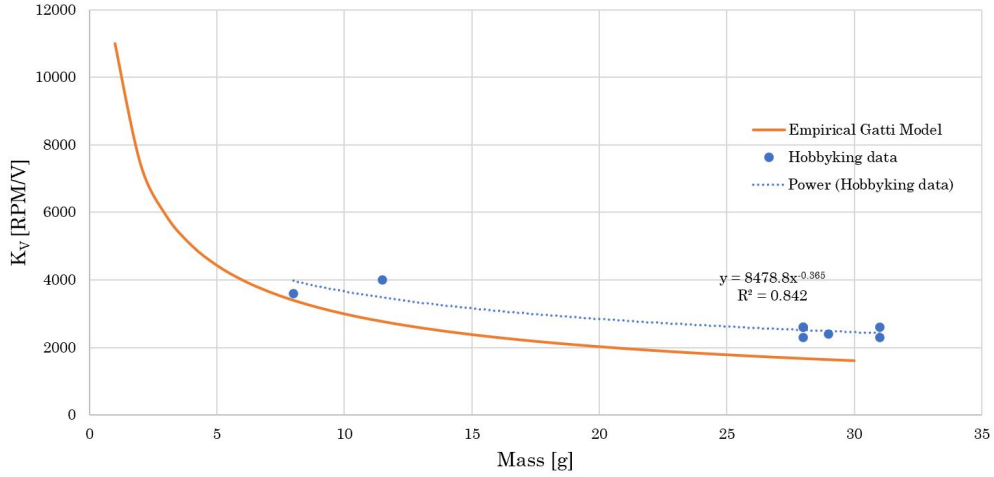


Figure 6.5: Motor Kv Rating vs Mass Model

$$m_{\text{prop},i} = 1.135B_i R_i^3 + m_{\text{hub}} \quad (6.4)$$

where B_i is number of blades and $m_{\text{hub}} = 0.0283kg$.

The battery mass is estimated using specific energy assumption of $k_{\text{bat}} = 170Wh/kg$. In optimization routine, battery capacity E_{bat} is always a design parameter and is updated in each optimisation loop. Thus battery mass can be found after each iteration. The location of battery is specified by the user.

$$m_{\text{bat}} = \frac{E_{\text{bat}}}{k_{\text{bat}}} \quad (6.5)$$

After each component mass is obtained, the total mass m_{total} is calculated using Eq. 6.1 and is passed on to the structural module.

6.2.3 Structural module

Currently the structural module only concerns the wing spar calculation, which computes maximal bending stress σ_{max} , deflection δ and spar mass m_{spar} . Spar dimension ξ is the design parameter that defines cross-section shape. Two cross-sections are available for the analysis as shown in Fig. 6.6 : circular shell or I-shaped section. In the case of the circular shell, ξ specifies the outer diameter of the tube while for the I-shaped cross section it corresponds to the beam height. The iteration of the outer dimension ξ acts as a loop to find the optimal size of the spar while minimizing its mass considering the aerodynamic loads on the wing.

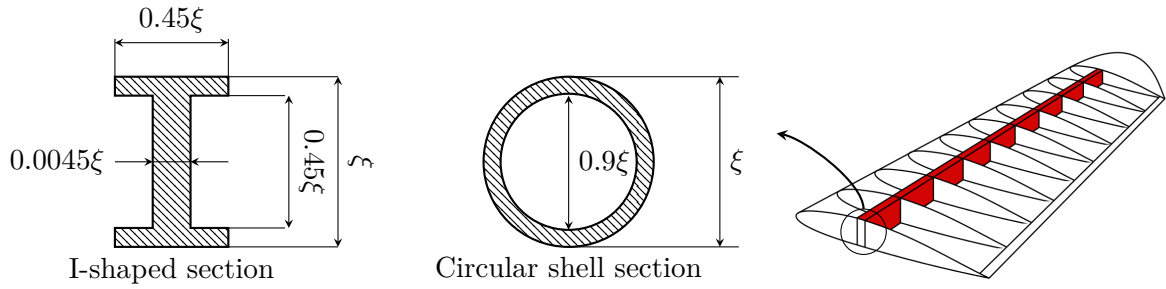


Figure 6.6: Wing Spar Cross Sections

As previously introduced the structural model representing the spar is a cantilever beam subjected to elliptical lift distribution. The force F acting on the beam is derived from the total mass m_{total} of the aircraft computed from the mass and balance module while taking into account a maximum load factor of $n_z = 3.5$. For symmetrical flight conditions, we only consider loading over semi-span as shown in Fig. 6.7.

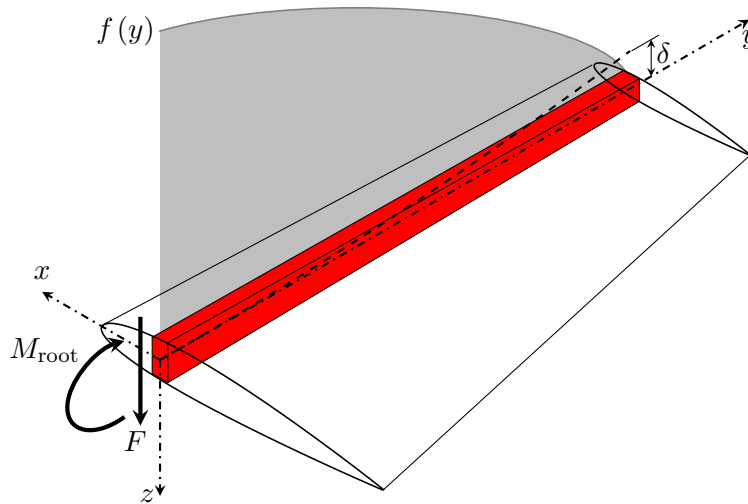


Figure 6.7: Wing spar under elliptical load distribution

$$F = \frac{m_{total}}{2} n_z g \quad (6.6)$$

The moment at the root M_{root} is derived by integrating the elliptical load distribution along the semi-span b .

$$M_{\text{root}} = \frac{2Fb}{3\pi} \quad (6.7)$$

Similarly the maximum deflection at the tip δ_{max} is derived from Equation 6.7. The centroidal moment of inertia I_c is calculated based on the cross-section of the spar and is the only difference in calculations between the two types of spars.

$$\delta_{\text{max}} = \frac{2Fb}{3\pi EI_c} \quad (6.8)$$

The maximum bending stress σ_{max} in critical section is reached at the upper and lower edges.

$$\sigma_{\text{max}} = \frac{M_{\text{root}}}{I_c} \frac{\xi}{2} \quad (6.9)$$

Structural constraints are presented below. The optimizer will solve the problem while observing the following constraints:

- Allowable normal stress: based on the properties of the material of the spar

$$\sigma_{\text{max}} \leq \sigma_{\text{allowable}} \quad (6.10)$$

- Tip deflection $\bar{\delta}$: the ratio between the deflection at the tip and the half span b

$$\frac{\delta_{\text{max}}}{b/2} = \bar{\delta}_{\text{max}} \leq \bar{\delta}_{\text{allowable}} \quad (6.11)$$

- Thickness ratio τ : the ration between the height of the spar and the minimal thickness of the wing

$$\bar{\tau} = \frac{\tau}{\xi} \quad (6.12)$$

Once the aircraft mass and the mass of the spar have converged, the total mass m_{total} is passed on to the aerodynamic module where it is used as a lift target for trim point calculation.

$$L_{\text{target}} = m_{\text{total}}g \quad (6.13)$$

6.2.3.1 Aerodynamic module

The aerodynamic module takes the aircraft configuration and given mission profile as inputs. The geometric specifications are compiled into .json file which MachUp has access to. For each given aircraft, it is possible to have two .json files as geometry input : VTOL and cruise configurations. The VTOL version contains lifting propellers used during VTOL phase and any relevant lifting surfaces while other propulsion groups or lifting surfaces were ignored in the aerodynamic model (but their mass impact is kept). According to [Hoe01], a slender wing at 90° angle of attack generates drag coefficients between 0.7 to 1.0. At extreme climb speed of $3m/s$ for a long endurance aircraft, this usually constitutes 5% of aircraft total gravity, and thus is ignored in the current study.

Similarly the cruise configuration eliminates any propulsion groups or lifting surfaces to be ignored in cruise analysis. The mass and balance module generates desired lift and moment for equilibrium flight.

For each flight segments defined in mission profile, the aerodynamic module performs a separate calculation. Each flight segment is identified as either a VTOL or cruise phase, for which the respective geometry input is used. Flight condition is also provided from the flight segment definition.

MachUp trim analysis is then executed to obtain aircraft state and control surface state. These are then fed back to MachUp force analysis to obtain aircraft force and moment information, as well as propeller shaft power.

6.2.4 Flight phase analysis

For a given candidate configuration, the performance and structural parameters are analysed and computed for each designated flight condition. These calculates results from the coupling between the aforementioned three modules : mass and balance, structure and aerodynamics. The aerodynamics discipline yields performance in flight, while the weight discipline will estimate required initial structural mass and will iterate within the structural discipline to size the spar according to the constraints and finally update the total mass. The aerodynamics optimization will revolve around finding the best wing planform for the mission profile.

Figure 6.8 outlines the data flow in the optimisation algorithm for a single flight phase. At the top is the optimisation component which manages the iteration loop by evaluating cost function and changing design parameters accordingly using the SLSQP algorithm. For current study, only mission energy E and endurance t_E are considered as cost function.

The respective design parameters are propagated into geometry and mass calculation modules. The geometry module takes the geometric design parameters and completes the aircraft definition with further assumptions, which are to be introduced for specific aircraft configurations.

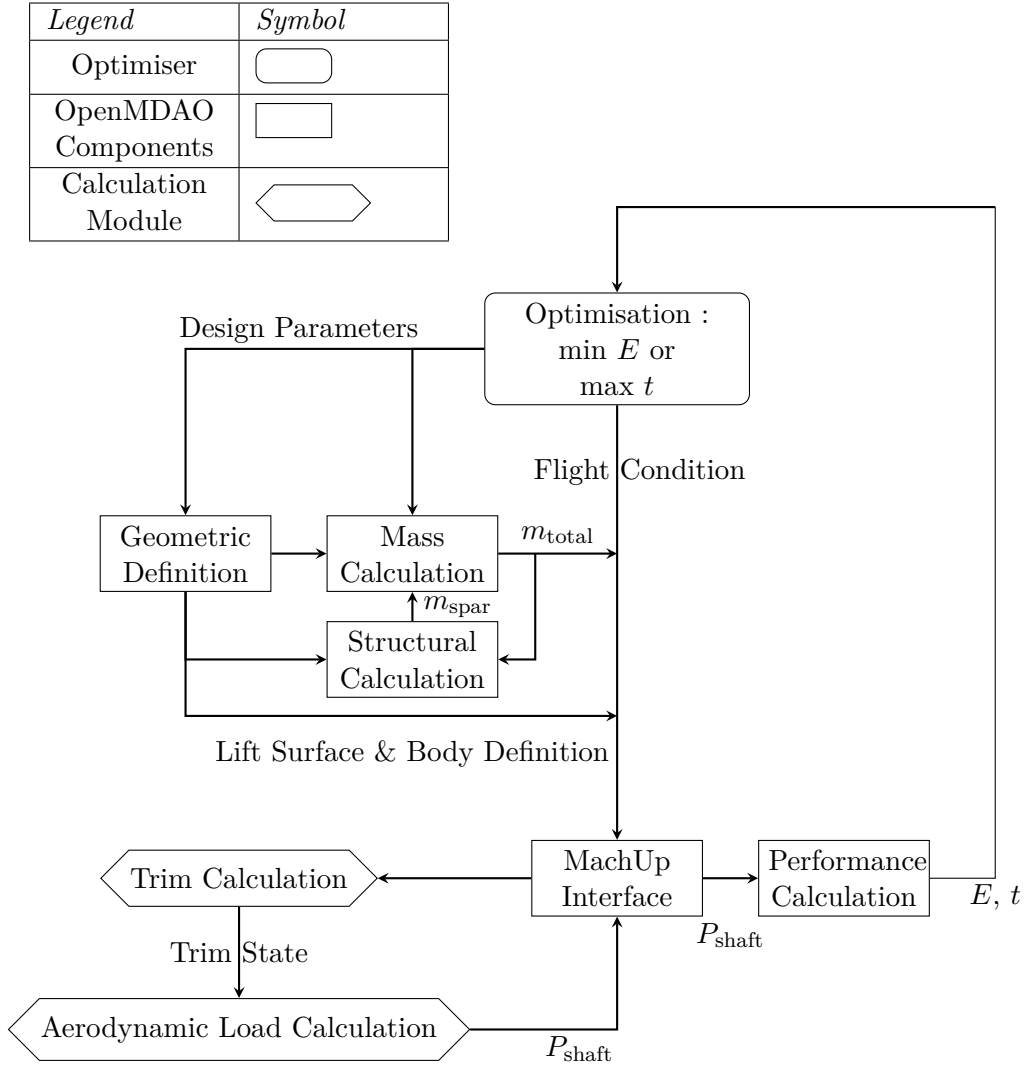


Figure 6.8: Design Flow Chart for a Single Flight Phase

The performance calculation takes input from the results from MachUp calculations and propulsion group definition to assess the flight performance.

For all N flight segments, only one segment n is allowed to have unspecified flight time, and in this case the algorithm maximises flight endurance of flight phase n .

Shaft power for each flight segment is provided from aerodynamic module for each propulsion group. The performance module then calculates total electric power consumption from Eq. 6.14.

$$P_{\text{elec}} = \frac{P_{\text{shaft}}}{\eta_m \eta_{\text{ESC}}} = \frac{P_{\text{shaft}}}{\eta_{\text{elec}}} \quad (6.14)$$

where η_{elec} is the electrical efficiency in the propulsion group.

The total power consumption is the sum of consumption from each propulsion group i and an additional constant avionic consumption, which is set to zero for the current study in order to highlight aerodynamic aspects.

$$P_{\text{total}} = \sum_{i=1}^N P_{\text{elec},i} + P_{\text{misc}} \quad (6.15)$$

Once total power consumption is known for each flight segment j , the remaining flight time for segment m is trivial to find.

$$t_n = \frac{\eta_{\text{bat}} E_{\text{bat}} - \sum_{j=1, j \neq n}^N P_{\text{total},j} t_j}{P_{\text{total},n}} \quad (6.16)$$

and is passed on as cost function.

The total endurance could then be found to be

$$t_E = \sum_{j=1}^N t_j \quad (6.17)$$

In the case that flight time and velocity are specified for all flight segments, the algorithm will try to minimise full mission energy consumption as can be found in Eq. 6.18.

$$E_{\text{total}} = \sum_{j=1}^N P_{\text{total},j} t_j \quad (6.18)$$

6.3 Optimization Problem

6.3.1 Problem Setup

The problem definition is done using the methods and structure available from OpenMDAO. The *Problem* class is used to define the top level container holding all the other objects. It contains all the system and its subsystems that build the model hierarchy. The *Component* class represents the lowest-level functionality and performs the mapping between input and output values which can be based on basic calculations or more complex functions. The *Group* class contains components or other groups or a combination of both. The main purpose of groups is to manage the data dependency between the subsystems but also to package components together that fall under the same discipline.

There are two major ways to analyze the mission, the optimization can be done for a single flight phase or for a combination of flight phases. For the latter method, there are two options available: minimize the overall mission energy consumption or maximize the endurance of a single phase based on the analysis of the other phases. The distinction between a single phase or several phases is done using the *flight_phase* variable. While the distinction between minimizing energy and maximizing endurance is done with the flight phase definition dictionary and is further explained in the following section.

During the initial development, the focus was on setting up the problem to optimize the UAV for a single flight phase as per Figure 6.8. Once the single phase optimization was validated, the overall flight phase optimization was developed with every flight phase now becoming a component of the problem. The sub-structure of each of the flight phases was maintained, so that the aerodynamics, structural integrity and mass estimation are calculated for each of the flight phases. Since the flight phases are connected with the same design variables we obtain a coupled model that needs to be converged in order for the outputs to be valid. This circular dependency between the phases requires a non-linear solver so that they can be converged by iterations. The chosen non-linear solver is the Newton solver. It is well suited for closely coupled problems. [Gra+19]. In the context of OpenMDAO, this type of problem is called a multidisciplinary analysis (MDA), which is an iterative process that will compute a set of coupling variables that will satisfy the consistency constraints between the coupled model, in this case the coupled flight phases.[LM12]

6.3.1.1 Flight Phases, Configuration and Independent Variables Definition

The flight mission is split up into several flight phases defined by the user in the *flight_phases* dictionary, such as : VTOL, climb, cruise, loiter, descent and landing. Each flight phase has the following keys: name, nature, elevation, V_x , V_z and duration. The duration is particularly important since it governs the setup of the problem: all flight phase duration can be defined or a single flight phase can have its duration set to zero. The first option sets the optimisation objective to be the minimisation of overall mission energy consumption while the second option sets it to the maximisation of a particular flight phase endurance. The speeds specified are in terms of calibrated airspeed $V_{CAS} = V_\infty \sqrt{\rho_\infty / \rho_0}$, where ρ_0 is air density in standard sea level condition. The flight phases are categorised into two families: *VTOL* nature and *cruise* nature. This defines the aircraft configuration as seen by the aerodynamic module in the particular flight phase.

The incorporated MachUp library allows for various combinations of lifting surfaces and propulsion systems representative to convertible UAVs, and the current study concentrates on three types of UAV configurations: quadcopter, quadplane and tilt-rotor when performing the optimization. The different configuration baselines are set up using a .json file and can be modified to meet specific requirements or geometries.

1. Quadcopter (Fig. ??): The rotor aircraft employs four lifting propellers having elliptical chord and ideal pitch distribution, defined by the radius R_{VTOL} and pitch angle β_{VTOL}

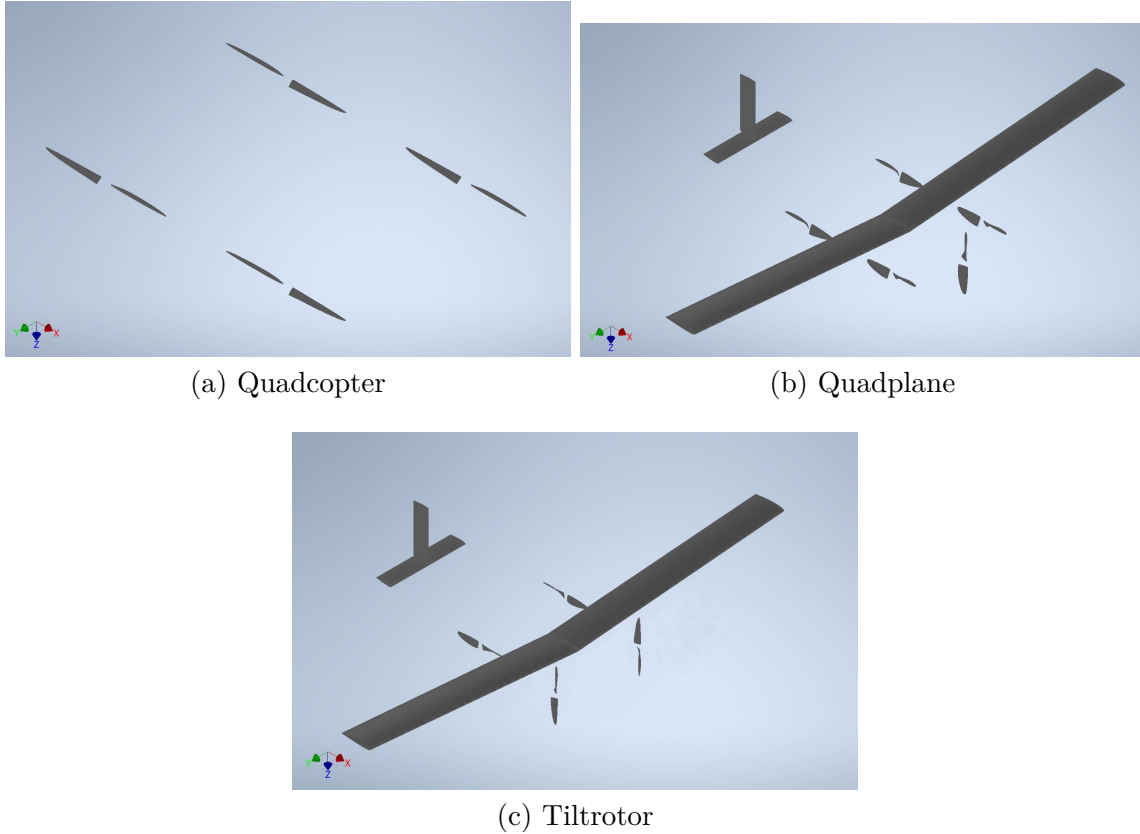


Figure 6.9: Studied VTOL aircraft configurations

at $75\%R_{VTOL}$. An X-shaped fuselage frame is calculated linking all four propellers with payload mass situated in the centre. No wing surface or structure is equipped for this configuration.

2. Quadplane (Fig. ??): This is a combination of quadcopter and a traditional aircraft. It has four lifting propellers and a cruise propeller which is defined independently by R_{cruise} and β_{cruise} . The lifting propellers are only used in VTOL configuration and cruise propeller operates only in cruise configuration. The aircraft has a main wing in the middle of front and rear lifting propeller pairs, its planform shape subjects to the definition of design parameters. A main spar is considered to support the lift load in cruise configuration. A tail section is sized with horizontal tail volume coefficient $V_H = 0.45$ and vertical tail volume coefficient $V_v = 0.02$. The aircraft has three extra streamlined bodies : fuselage between cruise propeller and horizontal tail ; two booms connecting each front and rear propeller through the wing.
3. Tiltrotor (Fig. ??): This configuration is similar to quadplane definition without the cruise propulsion group. The front propeller pairs operate in both VTOL and cruise configurations but it rotates from upward facing orientation in VTOL configuration to forward facing in cruise configuration. It is possible to use different propeller geometries

for front and rear propeller pairs, however it is rarely seen in practical design due to spar part requirements from frequent propeller damages.

There are several variables that need to be defined for the optimization and are grouped as follows: wing structure, flight condition, propulsion group parameters and are specified in Table. 6.2.

Group	Variable	Value	Unit	Comment
Wing structure	$\bar{\delta}$	0.05	-	Tip deflection
	E	150	GPa	Spar Young's modulus
	$\sigma_{\text{allowable}}$	3	GPa	Yield stress
	ρ_{spar}	1600	$kg \cdot m^{-3}$	Material density
	n_z	3.5	-	Maximal normal load factor
Flight condition	Beam Type	2	-	1 for I-shaped section ; 2 for circular shell section
	ρ_{air}	1.225	$kg \cdot m^{-3}$	Air density
	ν_{air}	1.5×10^{-5}	$m^2 \cdot s^{-1}$	Air kinematic viscosity
Propulsion group	g	9.81	$m \cdot s^{-2}$	Gravitational acceleration
	η_{elec}	0.75	-	Electrical efficiency
	η_{bat}	0.90	-	Usable battery capacity
	k_{bat}	170	$Wh \cdot kg^{-1}$	Battery specific energy

Table 6.2: Independent Variables

6.3.1.2 Design Variables

The previously described design variables for the different disciplines can be enabled or disabled in the current problem definition. This is done using the *add_design_var* method of the OpenMDAO library. Global design variables are applicable to all types of phases analyzed while local design variables are only applicable to one type of flight phase. The design variables along with their upper and lower bounds are listed in the table below:

Notice that the VTOL propellers could also be designated for cruise configuration, this is to accommodate configurations that do not have an independent propulsive group for cruise flight, such as quadcopter or some tiltrotor aircraft.

6.3.1.3 Constraints

The SLSQP driver allows the definition of inequality constraints using the *add_constraint* method. The constraints and their lower bound and upper bound are listed in Table 6.4.

Variable	Min	Max	Unit	Applicability
AR	8	15	-	All
S	0.2	2.0	m^2	All
E_{bat}	500	1000	Wh	All
R_{VTOL}	0.15	0.45	m	VTOL or All
β_{VTOL}	5	45	$^\circ$	VTOL or All
R_{cruise}	0.15	0.45	m	Cruise
β_{cruise}	5	45	$^\circ$	Cruise
λ	0.1	1.0	-	Cruise
ϕ	0	45	$^\circ$	Cruise
ξ	0.005	0.05	m	Cruise

Table 6.3: Design Parameters

The mean geometric chord c and wing span b constraints have been selected to match the design space of current existing commercial convertible UAVs. The battery capacity constraint ensure a reserve battery capacity of 10% following the design flight mission completion. The limit stress $\sigma_{\text{allowable}}$ value is representative of the yield strength of commercial carbon fiber reinforced polymer. The wing tip deflection ratio $\bar{\delta}$ is set at 5% of the half span of the wing based on engineering intuition. The thickness ratio $\bar{\tau}$ was chosen to be 10% meaning that the spar must not occupy more than 90% of the wing thickness.

Variable	Min	Max	Unit
c	0.05	0.30	m
b	0.00	3.50	m
E_{total}	-	$\eta_{\text{bat}} E_{\text{bat}}$	Wh
t_n	0	-	min
$C_{L_{max}}$	-	1.20	-
σ_{max}	-	3×10^9	Pa
$\bar{\delta}_{max}$	-	0.05	-
$\bar{\tau}$	1.10	-	-

Table 6.4: Constraints

6.3.1.4 Objective

As previously stated, there are two possible objectives depending on the definition of flight phases. If all flight phases are defined with non-zero flight duration, the objective is to minimise total energy consumption from all N flight phases.

$$\min(E_{\text{total}}) = \min \left(\sum_{j=1}^N P_{\text{total},j} t_j \right) \quad (6.19)$$

If one particular flight phase n has flight duration defined as zero, the objective is to maximise duration in of flight phase n , hence the flight endurance.

$$\max(t_n) = \max \frac{\eta_{\text{bat}} E_{\text{bat}} - \sum_{j=1, j \neq n}^N P_{\text{total},j} t_j}{P_{\text{total},n}} \quad (6.20)$$

6.3.1.5 XDSM diagram

The eXtended Design Structure Matrix (XDSM) is a tool used to visualize MDO processes [LM12]. It permits the visualisation of the optimization problem by representing the components, variable connections and optimization algorithms. The order in which the algorithm runs is also represented with a numbering system and lines. The XDSM is therefore a convenient way of illustrating all the data and process flow of the optimization problem. Green boxes represent generic processes, while parallelograms are used for data input and output. Components that refer to an iterative procedure are represented using rounded rectangles: purple rounded boxes represent the main driver which in this case is the SLSQP driver and the orange rounded boxes represent the non-linear solver, here the Newton solver. The circular dependency between components is illustrated with solid grey lines connecting the green boxes as shown in Figure 6.10. Table 6.5 defines the mathematical notations used in figure 6.10.

Symbol	Definition	Compositional
x	Vector of global design variables	$(AR, S, E_{\text{bat}}, R_{\text{cruise}}, \beta_{\text{cruise}}, R_{\text{VTOL}}, \beta_{\text{VTOL}}, \lambda, \phi, \xi)$
x_{VTOL}	Vector of VTOL design variables	$(AR, S, E_{\text{bat}}, R_{\text{cruise}}, \beta_{\text{cruise}}, R_{\text{VTOL}}, \beta_{\text{VTOL}})$
x_{Cruise}	Vector of Cruise design variables	$(AR, S, E_{\text{bat}}, R_{\text{cruise}}, \beta_{\text{cruise}}, \lambda, \phi, \xi)$
cst	Vector of constraints	$(c, b, E_{\text{total}} \text{ or } t_n, C_{L_{\text{max}}}, \sigma_{\text{allowable}}, \bar{\delta}, \bar{\tau})$
$()^*$	Vectors or variables at their optimal value	N/A
$()^0$	Initial value of vectors or variables	N/A

Table 6.5: Mathematical notation for MDO problem data

For the current optimization problem of maximizing the endurance of a single phase, a multidisciplinary feasible architecture (MDF) [EJ+94] was selected. The multidisciplinary design feasible architecture can be seen as a conversion from a single discipline case to multiple discipline case where the single discipline is replaced by the MDA. Here the previously introduced flow chart (Figure 6.8) becomes a single component representing each of the flight phases. The sequence of operations is shown by the black line and follows the numbering system. The MDF architecture for the current problem is presented below:

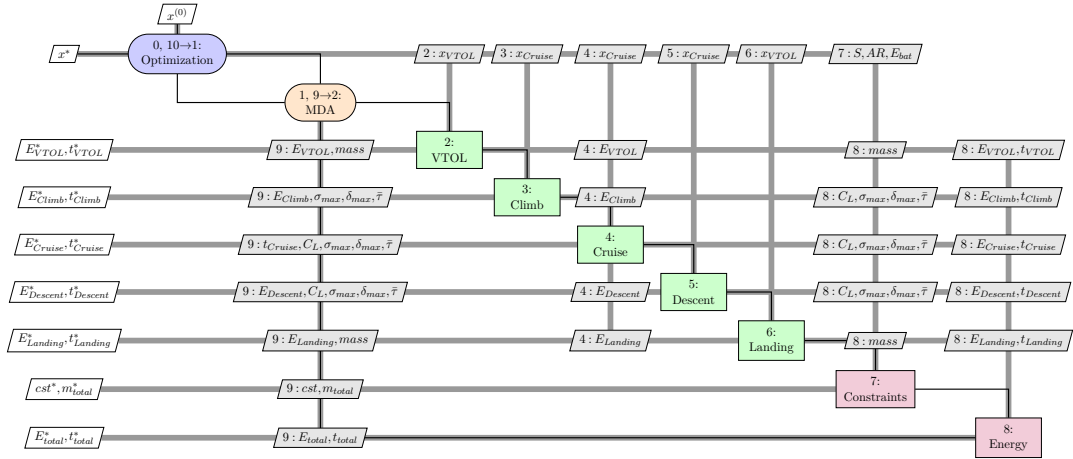


Figure 6.10: Maximize single phase endurance XDSM

The sequence of operations in the current problem is as follows:

0. Pass initial data (design variables) to Optimization and MDA drivers.
1. Initiate MDA using Newton solver.
2. Evaluate VTOL phase and return energy consumed and endurance.
3. Evaluate climb phase and return energy consumed and endurance.
4. Evaluate cruise phase using energy from other phases and determine remaining energy and endurance.
5. Evaluate descent phase and return energy consumed and endurance.
6. Evaluate landing phase and return energy consumed and endurance.
7. Compute constraint function values.
8. Compute cost function values.
9. Check MDA convergence. If it has not converged, return to 2; otherwise, continue.
10. Compute new design point. If optimization has not converged, return to 1; otherwise, return optimal solution.

The architecture above is maintained for both scenarios presented in the following section with the exception of the different flight phases based on the scenarios.

6.3.2 Test Cases Setup

The optimization algorithm is first tested on a baseline mission profile comprising vertical take-off, climb, cruise, descent and vertical landing as shown in Table. 6.6, with 60 minutes total endurance. Tiltrotor configuration is considered to allow comparison with Tron F90+[Qua], a similar vehicle from Quantum System. An additional 80W electrical power consumption was considered to better simulate the operational condition.

Parameters	TO	Climb	Cruise	Descent	Landing
Initial Elevation [m]	0	60	600	600	60
V_z [m/s]	2.0	1.5	0.0	-1.0	-1.0
V_x [m/s]	0.0	15.0	18.0	15.0	0.0
Duration [min]	0.5	6.0	43.5	9.0	1.0
Configuration	VTOL	Cruise	Cruise	Cruise	VTOL

Table 6.6: Baseline mission specifications

Commercial UAVs are optimized for one phase in which they spend the most time based on their application. It is therefore of interest to test scenarios in which the endurance of a single flight is optimized. Two typical scenarios were analyzed, without the previously mentioned 80W miscellaneous electrical power consumption.

6.3.2.1 Scenario 1: maximizing cruise endurance

In this scenario, the UAV is expected to perform a vertical take-off up to 60m, then to follow a 10% climb gradient at 15m/s no-wind ground speed up to 600m. The aircraft cruise at 18m/s for a maximal allowable time until its battery capacity reaches the final reserve level plus energy for a 6.7% descent to 60m followed by a vertical landing. This scenario is typical for long range surveillance mission or autonomous delivery flights. The goal is to choose the optimal design parameters to maximise the cruise endurance.

A detailed specification is provided in Table. 6.7.

Parameters	TO	Climb	Cruise	Descent	Landing
Initial Elevation [m]	0	60	600	600	60
V_z [m/s]	2.0	1.5	0.0	-1.0	-1.0
V_x [m/s]	0.0	15.0	18.0	15.0	0.0
Duration [min]	0.5	6.0	-	9.0	1.0
Configuration	VTOL	Cruise	Cruise	Cruise	VTOL

Table 6.7: Scenario 1 mission specifications

For quadcopter, the aircraft configuration won't change between flight phases, while for quadplane and tilt-rotor, only take-off and landing will be analysed using VTOL configuration.

6.3.2.2 Scenario 2: maximizing loiter endurance

The second scenario consists largely of the same flight phases as previous scenario, except that the cruise endurance is fixed at 70.3 minutes and an additional VTOL loiter phase is added. This scenario corresponds to local surveillance mission at remote site. The mission specification represents an action radius of $45km$ from the base and the surveillance site. The goal is thus to optimise the aircraft configuration to achieve maximal on-site loiter time.

The mission specification is detailed in Table. 6.8.

Parameters	TO	Climb	Cruise	Loiter	Descent	Landing
Initial Elevation [m]	0	60	600	600	600	60
V_z [m/s]	2.0	1.5	0.0	0.0	-1.0	-1.0
V_x [m/s]	0.0	15.0	18.0	0.0	15.0	0.0
Duration [min]	0.5	6.0	70.3	-	9.0	1.0
Configuration	VTOL	Cruise	Cruise	VTOL	Cruise	VTOL

Table 6.8: Scenario 2 mission specifications

6.3.3 Results and discussions

6.3.3.1 Baseline Mission Profile

The design parameters optimised for baseline mission profile are presented in Table. 6.9. Available data from Tron F90+ tiltrotor is displayed to allow comparison with an operational vehicle.

	Baseline Optimization	Tron F90+
AR [-]	14.2	13.7
S [m^2]	0.865	0.892
Span [m]	3.5	3.5
Taper Ratio [-]	0.942	Elliptical
R_{VTOL} [m]	0.2011	-
β_{VTOL} [$^\circ$]	24.5	-
Battery Capacity [Wh]	1000	-
Mass [kg]	14.0	13.5
Cruise L/D [-]	14.1	-
Total Endurance [min]	60.0	60.0

Table 6.9: Design parameters optimized for baseline mission and Tron F90+ specifications [Qua]

At conceptual design stage, the optimized vehicle dimensions resemble closely to those of the production aircraft. The wing surface area and total mass are within 5% of the published

specification, with the Tron F90+ having a lower wing loading. It is therefore promising that the tool is capable to simulator typical convertible mission and generate accurate initial size for conceptual design considerations.

6.3.3.2 Scenario 1

Design parameters optimised for each configuration are presented in Table. 6.10.

	Quadcopter	Quadplane	Tilt-rotor
AR [-]	-	14.1	14.6
S [m^2]	-	0.866	0.839
Taper Ratio [-]	-	0.96	1.00
R_{VTOL} [m]	0.4500	0.2044	0.1988
β_{VTOL} [$^\circ$]	6.0	8.6	29.9
R_{cruise} [m]	-	0.2064	-
β_{cruise} [$^\circ$]	-	17.6	-
Battery Capacity [Wh]	1000	1000	1000
Mass [kg]	12.0	14.7	12.2
Cruise L/D [-]	-	14.0	14.7
Cruise Endurance [min]	36.8	162.0	102.1
Total Endurance [min]	53.3	178.5	118.6
Mission Range [km]	53.2	188.4	123.8

Table 6.10: Design Parameters for scenario 1

Under scenario 1, the high speed cruise phase takes large part of airborne endurance. The respective aircraft design thus highly favors the parameters that minimise cruise power consumption. For all three configurations, the first priority in attempt to maximise endurance is to increase battery capacity. Within the given constraints, the maximal battery capacity of $1000Wh$ is reached in all three cases.

For quadcopter, both near-hover and cruise phase rely on rotary wing aerodynamics. The aircraft thus features large, fine pitch propellers which create less induced power. The propeller radius of $0.45m$ is similar to the design of helicopter whose propulsion system consists a light loaded main rotor. The maximal endurance reaches 53.3 minutes which is the smallest among the three configurations but a relatively high number among available quadcopters. Also notice that the maximal endurance is less than the 70.8 minutes required cruise endurance in scenario 2, and thus quadcopter configuration won't be considered for scenario 2.

For quadplane, the cruise phase is sustained by wing aerodynamic loads and a dedicated propulsion group. In consequence, a slender straight wing is desired, whose aspect ratio reaches 14.1. It is worth noting that the aspect ratio didn't reach its upper bound of 15. This is constrained by the minimal allowable thickness of airfoil to embed a sufficiently strong structure, where as the aspect ratio increases, the airfoil section dimension diminishes. The cruise propeller has a radius of $0.2064m$ and a higher pitch than VTOL propellers, which

is more efficient in high speed cruise. The VTOL propeller size is also much smaller than those of the quadcopter. Since near hover flight only takes 1.5 minutes, or less than 1% of total endurance, it is acceptable to install lighter but less efficient propeller to achieve VTOL capability. Overall, in the given scenario, quadplane configuration is possible to achieve the maximal endurance of 178.5 minutes among three candidates.

The tilt-rotor situates at a middle ground between quadcopter and quadplane. It features a slender wing for cruise flight but don't have a dedicated cruise propulsion group. The wing planform is very similar to the quadplane wing, however the lift to drag ratio increases by 1 due to the beneficial interaction of propeller slipstream. The propeller, or proprotor, installed is a compromise between ideal hover propeller and cruise propeller. Its radius is 56.0% smaller than that of the quadcopter but its pitch increases by almost 24° to provide required thrust in high speed condition. The cruise performance is significantly impacted by the propeller efficiency achieving an endurance 34.2% less than the quadplane endurance.

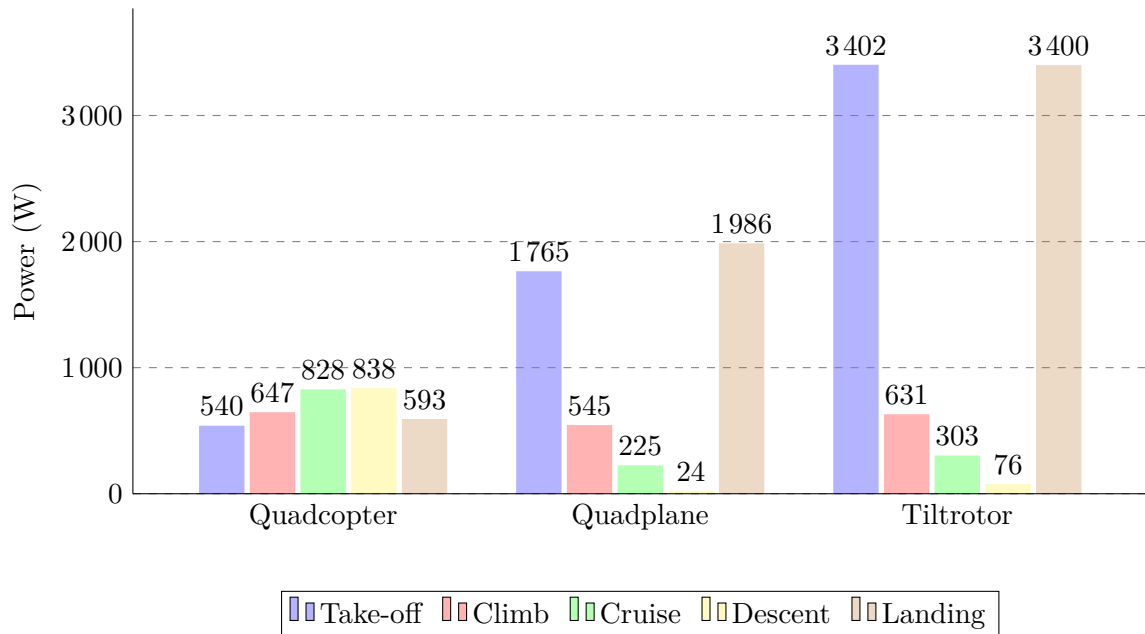


Figure 6.11: Power consumption by flight phase in scenario 1

A breakdown of electrical power consumption by flight phase is provided in Fig. 6.11. The quadcopter configuration shows lowest disparity between flight phases but its cruise power consumption remains the highest both relative to different flight phases and to the other two configurations. The quadplane consumes much higher than the quadcopter in VTOL phase, but only consumes less than a quarter in cruise phase. The tilt-rotor has the highest VTOL power consumption due to its high pitch propeller, while its cruise performance is comparable to a quadplane. Overall, power consumption demonstrates that a compromised system applied to both hover and cruise flight phase may result in lesser performance in either flight phase.

6.3.3.3 Scenario 2

Optimal design parameters to maximise loiter endurance under scenario 2 are shown in Table 6.11. Only quadplane and tilt-rotor configurations were analysed as it has been demonstrated clearly in scenario 1 analysis that quadcopter won't have the range capability to satisfy the mission profile. For tilt-rotor configuration, the optimal design was analysed again without propeller-wing interaction model, and the result is listed in the third column.

	Quadplane	Tilt-rotor	Tilt-rotor (Without Propeller Interaction)
AR [-]	13.0	14.0	14.0
S [m^2]	0.945	0.873	0.873
Taper Ratio [-]	1.00	0.93	0.93
R_{VTOL} [m]	0.4010	0.2627	0.2627
β_{VTOL} [$^\circ$]	7.9	21.0	21.0
R_{cruise} [m]	0.2101	-	-
β_{cruise} [$^\circ$]	22.8	-	-
Battery Capacity [Wh]	1000	1000	1000
Mass [kg]	16.0	14.1	14.1
Cruise L/D [-]	11.5	14.3	14.0
Loiter Endurance [min]	16.1	4.8	4.7
Total Endurance [min]	102.9	91.6	89.8

Table 6.11: Design parameters for scenario 2

The two configurations are largely similar to the previous designs but many design choices now favors more towards VTOL performances. For the quadplane, the radius of VTOL propellers doubles that calculated in scenario 1, and is only 10.8% smaller than the quadcopter. This results in an increase in aircraft mass, and in turn, a larger wing and cruise propeller are needed. Combined, the aircraft mass increased by 8.8% to achieve a maximum of 16.1 minutes for loiter.

For the tiltrotor, similar change appeared for its propeller design. Its radius increased from $0.1988m$ to $0.2627m$, a smaller magnitude compared to quadplane to keep its cruise efficiency. Propeller pitch also decreased from 29.9° to 21.0° in favor of loiter phase. The tiltrotor can sustain a 4.8 minutes loiter within a maximal flight time of 91.6 minutes.

The inclusion of propeller-wing interaction model slightly increased cruise lift to drag ratio and thus the aircraft is able to achieve 2% more endurance. However the interaction effect isn't significant at cruise advance ratio, as the change of local angle of attack due to slipstream is only slight compared to freestream convection.

The breakdown in power consumption including loiter flight is shown in Figure 6.12. Similarly as in Scenario 1, the independent propulsion architecture in quadplane design is able to achieve lower power consumption in all flight phases, and notably a 25% reduction in loiter phase compared to tiltrotor. However, the change in design objective also produced a

more balanced tiltrotor design, whose power consumption in VTOL phase reduced generally by 48% thanks to the reduced propeller disk loading.

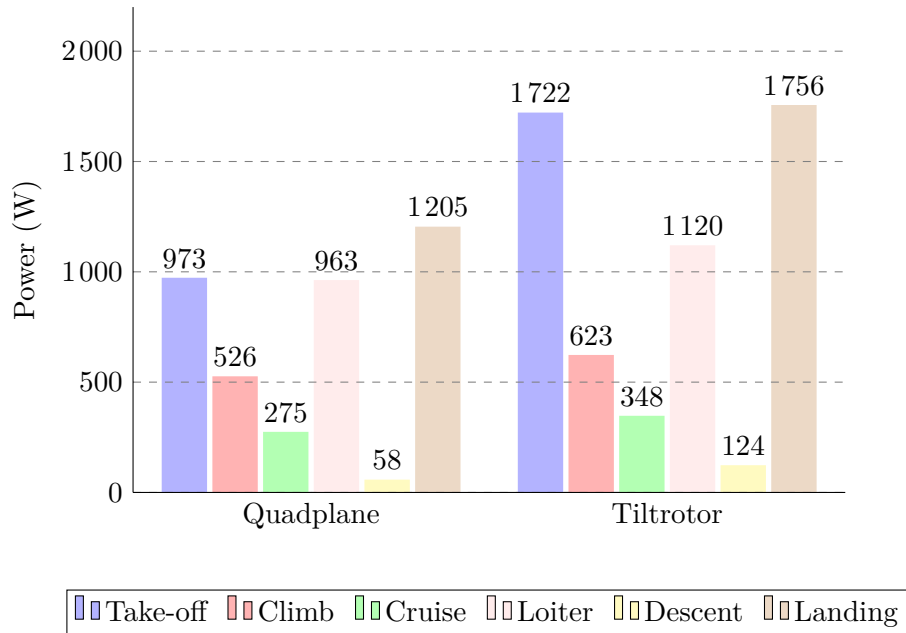


Figure 6.12: Power consumption by flight phase in scenario 2

Conclusion and perspectives

7.1 Main achievements

The work presented demonstrated a modern view of leveraging aerodynamic design to achieve vertical take-off and landing for a reduced-scale vehicle propelled by electrical system. The work reviews technical advances in aerodynamic modelling techniques needed to assess accurate flight performance in preliminary design context. It also envisioned how these tools could be assembled to evaluate impact of design choices on mission performance. The study fits well with researches on other technological fronts of electrical VTOL flight, and is expected to work in concert with other advances, such as those in aero-structure, flight control domains, to facilitate design of future long endurance autonomous flight vehicle. With these objectives in mind, the main achievements of the current work are as following.

7.1.1 Development of aerodynamic models

Major aerodynamic challenges were identified and appropriate models were provided. Among those studied effects, propeller performance at high incidence angle and its aerodynamic interaction with lifting surfaces were found to be of priority in analysing typical VTOL UAV concepts.

Increase in propeller thrust and power consumption were observed at high incidence angle encountered in VTOL transition flight condition, as well as the production of additional in-plane force and moment. A blade element analysis was performed and synthesized in a closed-form mathematical model. The model was compared with other frequently used rotary wing theories and was validated against dedicated windtunnel campaign. The model was found to be computationally efficient and required easily-accessible data to produce accurate prediction for preliminary design purposes. At certain conditions, power consumption might be over-estimated.

The study on propeller and wing interactions contained two parts : 1) deformation of propeller slipstream and 2) effect of propeller slipstream on lifting surface.

The location and form of propeller slipstream were found to be determined by freestream condition, thrust condition and the presence of immersed solid surface such as a wing. The influence of freestream condition was included in classic momentum analysis. The interaction

between slipstream and lifting surface was less studied. This effect was modelled using potential flow theory. The predicted slipstream shape was found to be in close agreement with flow survey results.

The aerodynamic augmentation effects of propeller slipstream over lifting surface was finally studied. A new analysis method was proposed using augmented aerodynamic coefficients, and such method allowed decomposition of augmentation effect into dynamic pressure terms and circulation terms. Experimental study in full-scale windtunnel campaign was performed to evaluate effective design parameters to leverage such effect. Matching of propeller thrust loading, propeller incidence angle and deflection of wing flaps were the most effective methods. Modification of vertical propeller displacement was also found useful to ensure the wing is properly immersed, especially at high angle of attack.

A modified numerical lifting line model was developed based on MachUp library to predict propeller-wing combination. Swirl reduction resulted from slipstream deformation was found critical to both numerical stability and accurate performance calculation.

7.1.2 Optimisation Methodology

An optimisation study was conducted over the basis of developed aerodynamic tools. A serial multi-disciplinary optimisation architecture was constructed in the OpenMDAO environment. The methodology fully utilises the current propeller and numerical lifting-line model, and is capable to consider diversified VTOL UAV concepts from quadcopter to tailsitter. Simplified structural and avionics models were included as different modules to complete the flight performance evaluation but these modules were designed to be expandable to allow the use of more accurate theories.

A comparison between quadcopter and hybrid airplane configuration was conducted using the proposed methodology. It demonstrated that it was capable to adapt aircraft design parameters with the specified mission profile and revealed different strategies must be taken in the optimisation of different vehicle configuration.

7.2 Future work

The current research has successfully identified the need of accurate and computationally efficient aerodynamic models in preliminary design phase. Significant advances have been made to address these need. However, in the process of development several important modifications have been uncovered to be beneficial for further improvements. They could not be incorporated in the current work due to either technological or time constraints.

The current slipstream displacement model is applicable only for wing placed along slipstream centreline. Future development could expand the theory to allow for non-symmetrical displacement and wing camber.

The numerical stability of the lifting line model can be further improved by a better modelling of induced velocity in slipstream. The current swirl velocity model is inherently rotational, and a strong swirl reduction is required to maintain stability when swirl velocity is introduced in wing boundary condition. A different assumption of swirl velocity profile should greatly improve the robustness of the solution.

The capability of optimisation routine can be enhanced using parallel computing and hence more design parameters can be considered over the same amount of time. Further cooperation of structural and flight control studies could provide more accurate model in their respective module and improve the confidence level of optimised solution.

Static Mass Error

Due to the displacement between the balance and motor-propeller centre of mass, there exists a static error in the force and moment measurement. Furthermore, small inclination of the support mast introduces a dependence on propeller incidence angle. A simplified free-body diagram is shown below for the test assembly with exaggerated inclination.

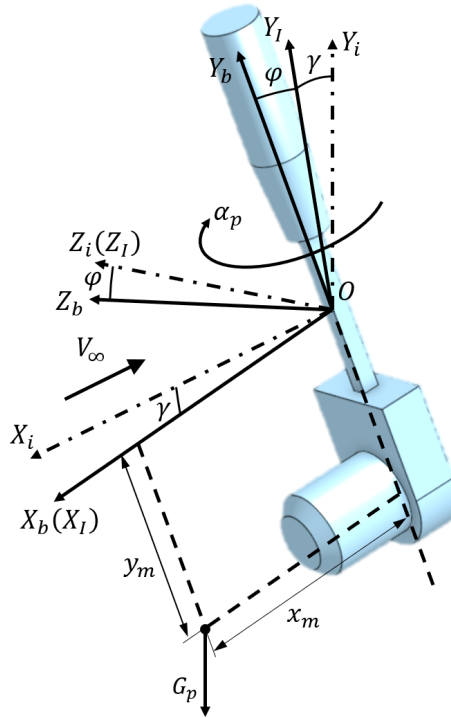


Figure A.1: Definition of Balance Inclinations

Three coordinates are depicted in the diagram: 1) ground-fixed frame $OX_i Y_i Z_i$; 2) intermediate frame $OX_I Y_I Z_I$ and 3) balance body frame $OX_b Y_b Z_b$ as introduced before. The motor-propeller centre of mass is assumed to be located at x_m and y_m in body frame.

Primary structural deformations are determined to be the inclination of balance frame's Y_b and Z_b axes. The diagram below defines the deformations as two angles φ and γ .

The derivation will consider $\alpha_p = 0$ as the baseline case, where, for $\varphi = \gamma = 0$, X_b axis is parallel to the opposite freestream direction. From the baseline case, the frame first rotates

angle γ around the Z_i axis to become intermediate frame $OX_I Y_I Z_I$. Then the frame further rotates an angle φ around the X_I axis to reach body frame $OX_b Y_b Z_b$. Finally, the body axis rotates around its Y_b axis for different incidence angles α_p .

In ground-fixed frame, the motor-propeller assembly gravity force G_p lies opposite to Y_i axis.

$$\vec{F}_0^i = [0 \quad -G_p \quad 0]^T$$

To obtain the force components in the body axis, the force in the ground-fixed frame is multiplied by three rotation matrices in order: 1) γ around Z ; 2) φ around X and 3) $-\alpha_p$ around Y . The resultant static force error can be found below.

$$\begin{aligned} \vec{F}_0^b &= \begin{bmatrix} \cos \alpha_p & 0 & -\sin \alpha_p \\ 0 & 1 & 0 \\ \sin \alpha_p & 0 & \cos \alpha_p \end{bmatrix} \begin{bmatrix} 1 & 0 & 0 \\ 0 & \cos \varphi & -\sin \varphi \\ 0 & \sin \varphi & \cos \varphi \end{bmatrix} \begin{bmatrix} \cos \gamma & -\sin \gamma & 0 \\ \sin \gamma & \cos \gamma & 0 \\ 0 & 0 & 1 \end{bmatrix} \begin{bmatrix} 0 \\ -G_p \\ 0 \end{bmatrix} \\ &= \begin{bmatrix} \cos \alpha_p \sin \gamma + \sin \alpha_p \sin \varphi \cos \gamma \\ -\cos \varphi \cos \gamma \\ \sin \alpha_p \sin \gamma - \cos \alpha_p \sin \varphi \cos \gamma \end{bmatrix} G_p \end{aligned}$$

To obtain the static moment error, the force error in body frame is multiplied by respective moment arm x_m and z_m .

$$\begin{aligned} \vec{M}_0^b &= \begin{bmatrix} 0 & 0 & y_m \\ 0 & 0 & -x_m \\ -y_m & x_m & 0 \end{bmatrix} \vec{F}_0^b \\ &= \begin{bmatrix} y_m (\sin \alpha_p \sin \gamma - \cos \alpha_p \sin \varphi \cos \gamma) \\ x_m (\cos \alpha_p \sin \varphi \cos \gamma - \sin \alpha_p \sin \gamma) \\ -x_m \cos \varphi \cos \gamma - y_m (\cos \alpha_p \sin \gamma + \sin \alpha_p \sin \varphi \cos \gamma) \end{bmatrix} G_p \end{aligned}$$

Thus, neglecting the superscript b for body frame, the static mass error can be modelled as below.

$$\begin{bmatrix} \vec{F}_0 \\ \vec{M}_0 \end{bmatrix} = \begin{bmatrix} \cos \alpha_p \sin \gamma + \sin \alpha_p \sin \varphi \cos \gamma \\ -\cos \varphi \cos \gamma \\ \sin \alpha_p \sin \gamma - \cos \alpha_p \sin \varphi \cos \gamma \\ y_m (\sin \alpha_p \sin \gamma - \cos \alpha_p \sin \varphi \cos \gamma) \\ x_m (\cos \alpha_p \sin \varphi \cos \gamma - \sin \alpha_p \sin \gamma) \\ -x_m \cos \varphi \cos \gamma - y_m (\cos \alpha_p \sin \gamma + \sin \alpha_p \sin \varphi \cos \gamma) \end{bmatrix} G_p$$

NACA Propeller Geometry

Relative Radius r'	Relative Chord c'	Pitch Angle [°]
0.112	0.299	52.099
0.149	0.299	51.429
0.186	0.299	50.570
0.223	0.299	49.521
0.260	0.299	48.284
0.297	0.299	46.857
0.334	0.299	45.241
0.371	0.299	43.436
0.408	0.299	41.441
0.445	0.299	39.258
0.482	0.299	37.041
0.519	0.299	35.028
0.556	0.299	33.198
0.593	0.299	31.531
0.630	0.299	30.008
0.667	0.299	28.614
0.704	0.299	27.334
0.741	0.299	26.155
0.778	0.299	25.068
0.815	0.299	24.062
0.852	0.299	23.130
0.889	0.299	22.264
0.926	0.299	21.457
0.963	0.299	20.704
1.000	0.299	20.000

Table B.1: NACA Propeller Geometry

NACA Proprotor Test Data

The freestream and proprotor tip speed ratio λ_∞ were regulated during the test according to table. 3.3.

$\alpha_p [^\circ]$	$\lambda_\infty = 0.06$				$\lambda_\infty = 0.14$			
	C_T	C_Q	C_N	C_n	C_T	C_Q	C_N	C_n
0	0.0233	0.0076	0.0000	0.0000	0.0186	0.0059	0.0000	0.0000
15	0.0234	0.0077	0.0072	0.0005	0.0187	0.0060	0.0016	0.0009
30	0.0236	0.0078	0.0015	0.0010	0.0204	0.0066	0.0033	0.0019
45	0.0239	0.0079	0.0022	0.0015	0.0222	0.0073	0.0052	0.0028
60	0.0244	0.0081	0.0028	0.0019	0.0244	0.0080	0.0063	0.0036
75	0.0250	0.0082	0.0033	0.0021	0.0274	0.0089	0.0068	0.0040
90	0.0257	0.0083	0.0035	0.0023	0.0315	0.0101	0.0067	0.0041

Table C.1: NACA Proprotor Test Data

$\alpha_p [^\circ]$	$\lambda_\infty = 0.22$				$\lambda_\infty = 0.32$			
	C_T	C_Q	C_N	C_n	C_T	C_Q	C_N	C_n
0	0.0139	0.0051	0.0000	0.0000	0.0052	0.0037	0.0000	0.0000
15	0.0147	0.0054	0.0013	0.0011	0.0073	0.0042	0.0025	0.0018
30	0.0167	0.0060	0.0038	0.0025	0.0117	0.0053	0.0052	0.0037
45	0.0198	0.0071	0.0064	0.0039	0.0168	0.0069	0.0087	0.0058
60	0.0244	0.0086	0.0080	0.0048	0.0236	0.0091	0.0118	0.0076
75	0.0293	0.0100	0.0096	0.0056	0.0309	0.0112	0.0141	0.0089
90	0.0364	0.0120	0.0090	0.0058	0.0386	0.0136	0.0129	0.0093

Table C.2: NACA Proprotor Test Data (continued)

Wake Surveys with Flap

Wake surveys with $\pm 15^\circ$ flap deflections are depicted in Fig. D.1 and Fig. D.2 for propeller rotation speed at $5770rpm$.

Wake surveys with $\pm 15^\circ$ flap deflections are depicted in Fig. D.3 and Fig. D.4 for propeller rotation speed at $10000rpm$.

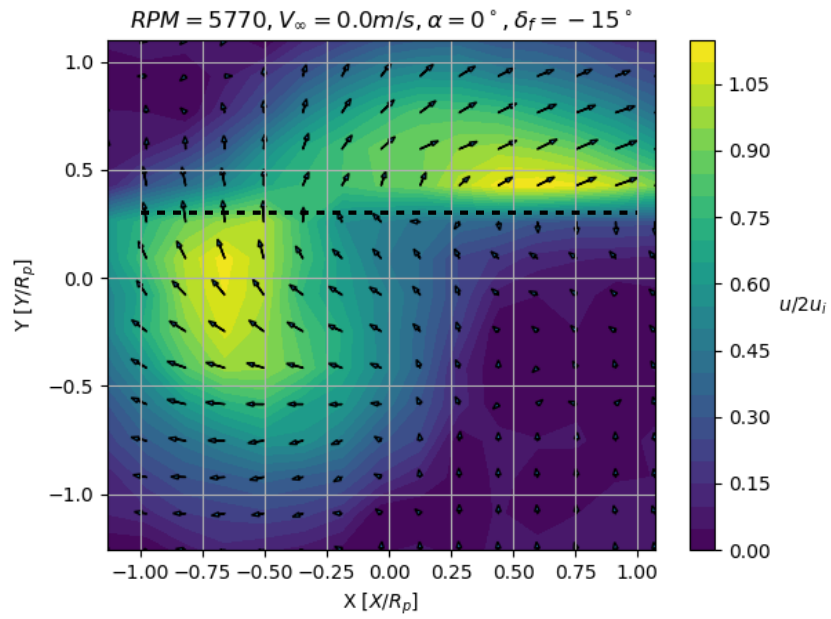


Figure D.1: -15° flap deflection

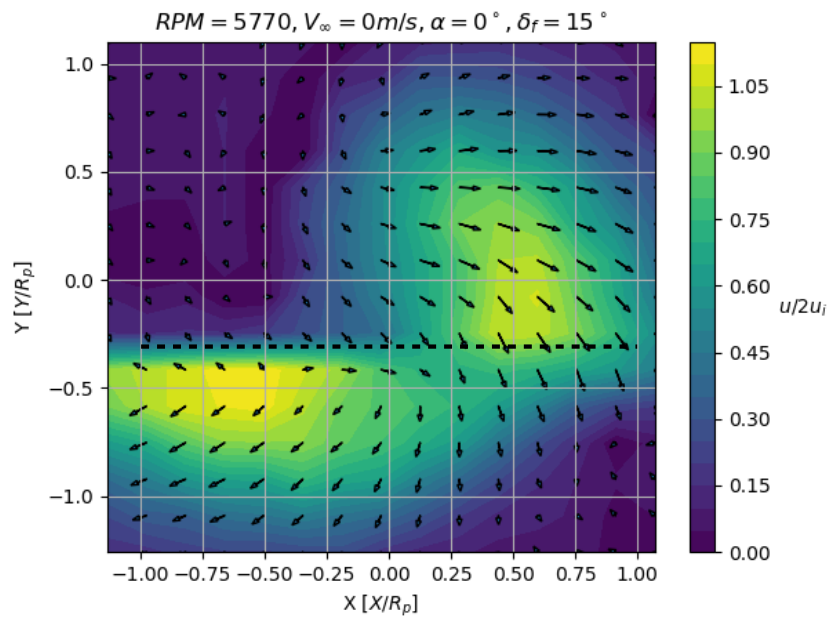


Figure D.2: 15° flap deflection

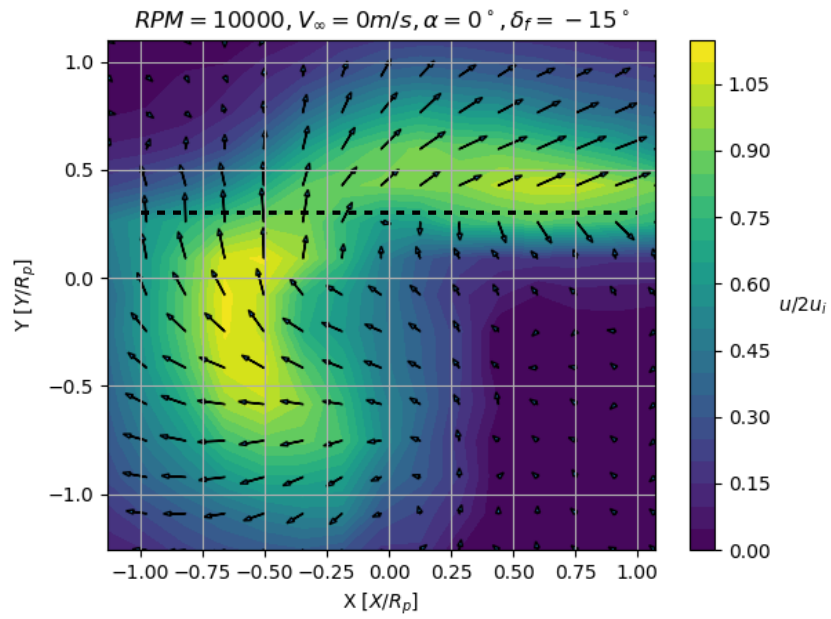


Figure D.3: -15° flap deflection

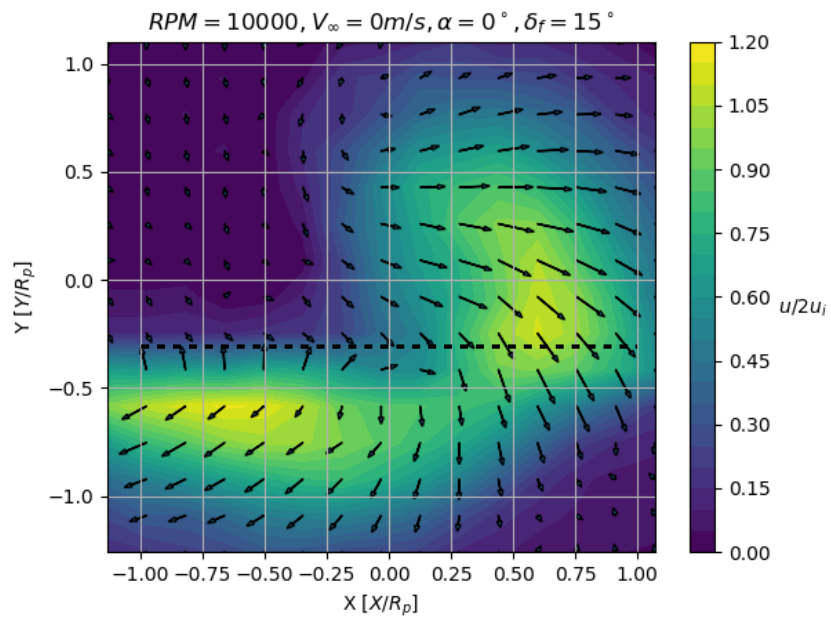


Figure D.4: 15° flap deflection

Relation between Propeller and Slipstream Parameters

In the derivation of deformed centreline equations, it has been observed that the centreline profile is associated with propeller working condition by two parameters : wake helix angle ϕ and rotor plane circulation Γ_0 .

The two parameters can be related to propeller thrust condition by the application of momentum theory. Consider the centreline velocity induced by the vortical system at propeller plane, from equation 4.16 where

$$v_{ia}(0) = -\frac{\Gamma_0 \cos \phi}{4\pi R}. \quad (\text{E.1})$$

From momentum theory [Lei06], the rotor plane induced velocity can be concluded, and is applicable for both static and forward flight condition, as

$$v'_{ia}(0) = -\frac{nD}{2} \left(\sqrt{\frac{8C_T}{\pi} + J^2} - J \right). \quad (\text{E.2})$$

By setting the two velocities equal, the rotor plane circulation can be solved:

$$\Gamma_0 = \frac{4\pi R^2 n}{\cos \phi} \left(\sqrt{\frac{8C_T}{\pi} + J^2} - J \right), \quad (\text{E.3})$$

or in non-dimensional form as used in the discussion before.

$$\begin{aligned} \bar{\Gamma}_0 &= \frac{\Gamma_0}{4\pi V_\infty R} \\ &= \frac{\sec \phi}{2} \left(\sqrt{\frac{8C_T}{\pi J^2} + 1} - 1 \right). \end{aligned} \quad (\text{E.4})$$

The wake helix angle can be found using velocity geometry relations:

$$\begin{aligned}
\tan\phi &= -\frac{V_\infty + v_{ia}}{\Omega R} \\
&= \frac{1}{2\pi} \left(\sqrt{\frac{8C_T}{\pi} + J^2} - J \right).
\end{aligned}
\tag{E.5}$$

Useful Integrations

$$\mathbf{F.1} \quad \int_{z_1}^{z_2} \frac{ds}{s(\sqrt{1+s^2}-s)}$$

After rationalization, the integral can be simplified,

$$\begin{aligned} & \int_{z_1}^{z_2} \frac{1/s ds}{\sqrt{1+s^2}-s} \\ &= \int_{z_1}^{z_2} 1 + \sqrt{1 + \frac{1}{s^2}} ds \\ &= z_2 - z_1 + \int_{z_1}^{z_2} \sqrt{1 + \frac{1}{s^2}} ds. \end{aligned} \tag{F.1}$$

For the integral $\int_{z_1}^{z_2} \sqrt{1 + \frac{1}{s^2}} ds$, make a change of variable $s = \tan \theta$, and let $\theta_1 = \tan^{-1} z_1$, $\theta_2 = \tan^{-1} z_2$. The integral is then solved by parts:

$$\begin{aligned} & \int_{z_1}^{z_2} \sqrt{1 + \frac{1}{s^2}} ds \\ &= \int_{\theta_1}^{\theta_2} \csc \theta \sec^2 \theta d\theta \\ &= \csc \theta \tan \theta \Big|_{\theta_1}^{\theta_2} + \int_{\theta_1}^{\theta_2} \csc \theta d\theta \\ &= \sqrt{1+z_2^2} - \sqrt{1+z_1^2} + \ln |\csc \theta - \cot \theta| \Big|_{\theta_1}^{\theta_2} \\ &= \zeta_2 - \zeta_1 + \ln \left| \frac{z_1}{z_2} \frac{1-\zeta_2}{1-\zeta_1} \right|, \end{aligned} \tag{F.2}$$

where $\zeta = \sqrt{1+z^2}$.

Thus the complete integral is solved as

$$\int_{z_1}^{z_2} \frac{1/s ds}{\sqrt{1+s^2}-s} = z_2 - z_1 + \zeta_2 - \zeta_1 + \ln \left| \frac{z_1}{z_2} \frac{1-\zeta_2}{1-\zeta_1} \right|. \tag{F.3}$$

$$\mathbf{F.2} \quad \int_{z_1}^{z_2} \frac{\sqrt{1+s^2} - s}{a\sqrt{1+s^2} - (a-1)s} ds$$

Rationalize the integral, and $a = 1 + \bar{\Gamma}_0 \cos\theta$ is assumed to be larger than unity for normal flight condition,

$$\begin{aligned} & \int_{z_1}^{z_2} \frac{\sqrt{1+s^2} - s}{a\sqrt{1+s^2} - (a-1)s} ds \\ &= \int_{z_1}^{z_2} \frac{s^2 - s\sqrt{1+s^2} + a}{(2a-1)s^2 + a^2} ds \\ &= \int_{z_1}^{z_2} \frac{s^2}{(2a-1)s^2 + a^2} ds - \int_{z_1}^{z_2} \frac{s\sqrt{1+s^2}}{(2a-1)s^2 + a^2} ds \\ &\quad + a \int_{z_1}^{z_2} \frac{ds}{(2a-1)s^2 + a^2} \\ &= I_1 - I_2 + aI_3. \end{aligned} \tag{F.4}$$

The first and third integrations are trivial:

$$\begin{aligned} I_1 &= \int_{z_1}^{z_2} \frac{s^2}{(2a-1)s^2 + a^2} ds \\ &= \frac{1}{2a-1} \left[s - \frac{a}{\sqrt{2a-1}} \tan^{-1} \left(s \frac{\sqrt{2a-1}}{a} \right) \right] \Big|_{z_1}^{z_2} \\ &= \frac{z_2 - z_1}{2a-1} - \frac{a(\psi_2 - \psi_1)}{(2a-1)^{3/2}}, \end{aligned} \tag{F.5}$$

where $\psi = \tan^{-1} \left(z \frac{\sqrt{2a-1}}{a} \right)$, and

$$\begin{aligned} I_3 &= \int_{z_1}^{z_2} \frac{ds}{(2a-1)s^2 + a^2} \\ &= \frac{\sqrt{2a-1}}{a(2a-1)} \tan^{-1} \left(s \frac{\sqrt{2a-1}}{a} \right) \Big|_{z_1}^{z_2} \\ &= \frac{\sqrt{2a-1}}{a} (\psi_2 - \psi_1). \end{aligned} \tag{F.6}$$

The second integral is solved using a change of variable $\zeta = \sqrt{1+s^2}$, and let $b = \sqrt{\frac{a^2}{2a-1}}$,

$$\begin{aligned}
I_2 &= \frac{1}{2a-1} \int_{z_1}^{z_2} \frac{s\sqrt{1+s^2}}{s^2+b^2} ds \\
&= \frac{1}{2a-1} \int_{\zeta_1}^{\zeta_2} \frac{\zeta^2}{\zeta^2+b^2-1} d\zeta \\
&= \frac{1}{2a-1} \left(\zeta - \sqrt{b^2-1} \tan^{-1} \frac{\zeta}{\sqrt{b^2-1}} \right) \Big|_{\zeta_1}^{\zeta_2} \\
&= \frac{\zeta_2 - \zeta_1}{2a-1} - \frac{(a-1)(\xi_2 - \xi_1)}{(2a-1)^{3/2}},
\end{aligned} \tag{F.7}$$

where $\xi = \tan^{-1} \frac{\sqrt{(2a-1)(1+z^2)}}{a-1}$.

Thus the integral is solved as

$$\begin{aligned}
&\int_{z_1}^{z_2} \frac{\sqrt{1+s^2} - s}{a\sqrt{1+s^2} - (a-1)s} ds \\
&= \frac{z_2 - z_1 - (\zeta_2 - \zeta_1)}{2a-1} \\
&\quad + \frac{a-1}{(2a-1)^{3/2}} (\psi_2 - \psi_1 + \xi_2 - \xi_1).
\end{aligned} \tag{F.8}$$

F.3
$$\int_{z_1}^{z_2} \frac{ds}{s [a\sqrt{1+s^2} - (a-1)s]}$$

Rationalize the integral, and $a = 1 + \bar{\Gamma}_0 \cos\theta$ is assumed to be larger than unity for normal flight condition:

$$\begin{aligned}
&\int_{z_1}^{z_2} \frac{ds}{s [a\sqrt{1+s^2} - (a-1)s]} ds \\
&= \int_{z_1}^{z_2} \frac{(a-1)s + a\sqrt{1+s^2}}{s[(2a-1)s^2 + a^2]} ds \\
&= \int_{z_1}^{z_2} \frac{a-1}{(2a-1)s^2 + a^2} ds + \int_{z_1}^{z_2} \frac{a\sqrt{1+s^2}}{s[(2a-1)s^2 + a^2]} ds \\
&= (a-1)I_3 + aI_4.
\end{aligned} \tag{F.9}$$

Integral I_3 is trivial.

Now only I_4 remains to be solved. Make a change of variable $\zeta = \sqrt{1+s^2}$,

$$\begin{aligned}
& \int_{z_1}^{z_2} \frac{\sqrt{1+s^2} ds}{s[(2a-1)s^2+a^2]} ds \\
&= \frac{1}{a^2} \int_{\zeta_1}^{\zeta_2} \frac{d\zeta}{\zeta^2-1} \\
& \quad + \frac{(a-1)^2}{a^2(2a-1)} \int_{\zeta_1}^{\zeta_2} \frac{d\zeta}{\zeta^2 + (a-1)^2/(2a-1)} \\
&= \frac{1}{2a^2} \ln \left| \frac{\zeta_2-1}{\zeta_1-1} \frac{\zeta_1+1}{\zeta_2+1} \right| + \frac{(a-1)(\xi_2-\xi_1)}{a^2\sqrt{2a-1}}. \tag{F.10}
\end{aligned}$$

Thus the complete integral is obtained as

$$\begin{aligned}
& \int_{z_1}^{z_2} \frac{ds}{s[a\sqrt{1+s^2} - (a-1)s]} \\
&= \frac{1}{2a} \ln \left| \frac{\zeta_2-1}{\zeta_1-1} \frac{\zeta_1+1}{\zeta_2+1} \right| \\
& \quad + \frac{(a-1)}{a\sqrt{2a-1}} (\psi_2 - \psi_1 + \xi_2 - \xi_1). \tag{F.11}
\end{aligned}$$

Optimal Aircraft Designs

G.1 Hybrid Airplane

```
1 {
2   "plane": {
3     "name": "MyAirplane",
4     "CGx": 0.03785491815500484,
5     "CGy": 0.008028812278611061,
6     "CGz": 0.007983241994859757
7   },
8   "reference": {
9     "area": 0.3845626510700489,
10    "longitudinal_length": 0.19610269020848461,
11    "lateral_length": 1.961026902084846
12  },
13  "condition": {
14    "units": "SI"
15  },
16  "wings": {
17    "Main_Wing": {
18      "name": "Main_Wing",
19      "ID": 1,
20      "is_main": 1,
21      "side": "both",
22      "connect": {
23        "ID": 0,
24        "location": "tip",
25        "dx": 0,
26        "dy": 0,
27        "dz": 0,
28        "yoffset": 0
29      },
30      "span": 0.980513451042423,
31      "sweep": 0,
32      "dihedral": 5,
33      "mounting_angle": 0,
```

```

34     "washout": 0,
35     "root_chord": 0.2813109906242587,
36     "tip_chord": 0.11089438979271055,
37     "rho_mat": 66.07,
38     "t_c": 0.12,
39     "airfoils": {
40         "S1223": {
41             "properties": {
42                 "type": "linear",
43                 "alpha_L0": -0.1674,
44                 "CL_alpha": 6.82,
45                 "Cm_L0": -0.2908,
46                 "Cm_alpha": 0.1408,
47                 "CD0": 0.0352,
48                 "CD0_L": -0.0316,
49                 "CD0_L2": 0.0144,
50                 "CL_max": 1.4
51             }
52         }
53     },
54     "grid": 40,
55     "control": {
56         "has_control_surface": true,
57         "span_root": 0.5,
58         "span_tip": 1,
59         "chord_root": 0.2,
60         "chord_tip": 0.2,
61         "is_sealed": 1,
62         "mix": {
63             "elevator": 0,
64             "rudder": 0,
65             "aileron": 1,
66             "flap": 0
67         }
68     },
69     "sameAsRoot": true
70 },
71 "Horz_Tail": {
72     "name": "Horz_Tail",
73     "ID": 2,
74     "is_main": 0,
75     "side": "both",
76     "connect": {
77         "ID": 0,

```

```

78     "location": "tip",
79     "dx": -0.686359415729696,
80     "dy": 0,
81     "dz": 0,
82     "yoffset": 0
83 },
84 "span": 0.2563088780241104,
85 "sweep": 0,
86 "dihedral": 0,
87 "mounting_angle": -2,
88 "washout": 0,
89 "root_chord": 0.10252355120964415,
90 "tip_chord": 0.10252355120964415,
91 "rho_mat": 66.07,
92 "t_c": 0.12,
93 "airfoils": {
94     "NACA0012": {
95         "properties": {
96             "type": "linear",
97             "alpha_L0": 0,
98             "CL_alpha": 7.8,
99             "Cm_L0": 0,
100            "Cm_alpha": -0.1847,
101            "CD0": 0.0088,
102            "CD0_L": 0.0,
103            "CD0_L2": 0.0084,
104            "CL_max": 1.1
105        }
106    }
107 },
108 "grid": 40,
109 "control": {
110     "has_control_surface": true,
111     "span_root": 0,
112     "span_tip": 1,
113     "chord_root": 0.2,
114     "chord_tip": 0.2,
115     "is_sealed": 1,
116     "mix": {
117         "elevator": 1,
118         "rudder": 0,
119         "aileron": 0,
120         "flap": 0
121     }

```

```

122     },
123     "sameAsRoot": true
124 },
125 "Vert_Tail": {
126     "name": "Vert_Tail",
127     "ID": 3,
128     "is_main": 0,
129     "side": "right",
130     "connect": {
131         "ID": 0,
132         "location": "tip",
133         "dx": -0.686359415729696,
134         "dy": 0,
135         "dz": -0.01524,
136         "yoffset": 0
137     },
138     "span": 0.2143410794231939,
139     "sweep": 0,
140     "dihedral": 90,
141     "mounting_angle": 0,
142     "washout": 0,
143     "root_chord": 0.10252355120964415,
144     "tip_chord": 0.10252355120964415,
145     "rho_mat": 66.07,
146     "t_c": 0.12,
147     "airfoils": {
148         "NACA0012": {
149             "properties": {
150                 "type": "linear",
151                 "alpha_L0": 0,
152                 "CL_alpha": 7.8,
153                 "Cm_L0": 0,
154                 "Cm_alpha": -0.1847,
155                 "CD0": 0.0088,
156                 "CD0_L": 0.0,
157                 "CD0_L2": 0.0084,
158                 "CL_max": 1.1
159             }
160         }
161     },
162     "grid": 40,
163     "control": {
164         "has_control_surface": true,
165         "span_root": 0,

```

```

166     "span_tip": 1,
167     "chord_root": 0.2,
168     "chord_tip": 0.2,
169     "is_sealed": 1,
170     "mix": {
171         "elevator": 0,
172         "rudder": -1,
173         "aileron": 0,
174         "flap": 0
175     }
176 },
177     "sameAsRoot": true
178 }
179 },
180 "propellers": {
181     "prop_cruise_drivetrain": {
182         "name": "Main_Prop",
183         "position": {
184             "dx": 0.4199380790866125,
185             "dy": 0,
186             "dz": 0
187         },
188         "orientation": {
189             "elevation_angle": 0,
190             "heading_angle": 0
191         },
192         "radial_nodes": 35,
193         "diameter": 0.6096,
194         "hub_diameter": 0.06096,
195         "num_of_blades": 3,
196         "rotation_direction": "CCW",
197         "pitch": {
198             "type": "ratio",
199             "value": 0.5
200         },
201         "chord": {
202             "type": "elliptical",
203             "root": 0.04572
204         },
205         "m_hub": 0.0283,
206         "airfoils": {
207             "NACA2412": {
208                 "properties": {
209                     "type": "linear",

```

```

210         "alpha_L0": -0.036899751,
211         "CL_alpha": 6.283185307,
212         "Cm_L0": -0.0527,
213         "Cm_alpha": -0.08,
214         "CD0": 0.0055,
215         "CD0_L": -0.0045,
216         "CD0_L2": 0.01,
217         "CL_max": 1.4
218     }
219 }
220 }
221 },
222 "prop_drivetrain_1": {
223     "name": "prop_cw",
224     "position": {
225         "dx": -0.2953852399413136,
226         "dy": 0.260629777849676,
227         "dz": 0
228     },
229     "orientation": {
230         "elevation_angle": 90,
231         "heading_angle": 0
232     },
233     "radial_nodes": 35,
234     "diameter": 0.3000000567360903,
235     "hub_diameter": 0.030000005673609033,
236     "num_of_blades": 3,
237     "rotation_direction": "CW",
238     "pitch": {
239         "type": "ratio",
240         "value": 0.5
241     },
242     "chord": {
243         "type": "elliptical",
244         "root": 0.04572
245     },
246     "m_hub": 0.0283,
247     "airfoils": {
248         "NACA2412": {
249             "properties": {
250                 "type": "linear",
251                 "alpha_L0": -0.036899751,
252                 "CL_alpha": 6.283185307,
253                 "Cm_L0": -0.0527,

```

```

254         "Cm_alpha": -0.08,
255         "CD0": 0.0055,
256         "CD0_L": -0.0045,
257         "CD0_L2": 0.01,
258         "CL_max": 1.4
259     }
260 }
261 }
262 },
263 "prop_drivetrain_2": {
264     "name": "prop_ccw",
265     "position": {
266         "dx": 0.2399380450449583,
267         "dy": 0.260629777849676,
268         "dz": 0
269     },
270     "orientation": {
271         "elevation_angle": 90,
272         "heading_angle": 0
273     },
274     "radial_nodes": 35,
275     "diameter": 0.3000000567360903,
276     "hub_diameter": 0.030000005673609033,
277     "num_of_blades": 3,
278     "rotation_direction": "CCW",
279     "pitch": {
280         "type": "ratio",
281         "value": 0.5
282     },
283     "chord": {
284         "type": "elliptical",
285         "root": 0.04572
286     },
287     "m_hub": 0.0283,
288     "airfoils": {
289         "NACA2412": {
290             "properties": {
291                 "type": "linear",
292                 "alpha_L0": -0.036899751,
293                 "CL_alpha": 6.283185307,
294                 "Cm_L0": -0.0527,
295                 "Cm_alpha": -0.08,
296                 "CD0": 0.0055,
297                 "CD0_L": -0.0045,

```

```

298         "CD0_L2": 0.01,
299         "CL_max": 1.4
300     }
301 }
302 }
303 },
304 "prop_drivetrain_3": {
305     "name": "prop_cw",
306     "position": {
307         "dx": 0.2399380450449583,
308         "dy": -0.260629777849676,
309         "dz": 0
310     },
311     "orientation": {
312         "elevation_angle": 90,
313         "heading_angle": 0
314     },
315     "radial_nodes": 35,
316     "diameter": 0.3000000567360903,
317     "hub_diameter": 0.030000005673609033,
318     "num_of_blades": 3,
319     "rotation_direction": "CW",
320     "pitch": {
321         "type": "ratio",
322         "value": 0.5
323     },
324     "chord": {
325         "type": "elliptical",
326         "root": 0.04572
327     },
328     "m_hub": 0.0283,
329     "airfoils": {
330         "NACA2412": {
331             "properties": {
332                 "type": "linear",
333                 "alpha_L0": -0.036899751,
334                 "CL_alpha": 6.283185307,
335                 "Cm_L0": -0.0527,
336                 "Cm_alpha": -0.08,
337                 "CD0": 0.0055,
338                 "CD0_L": -0.0045,
339                 "CD0_L2": 0.01,
340                 "CL_max": 1.4
341             }

```

```

342     }
343   }
344 },
345 "prop_drivetrain_4": {
346   "name": "prop_ccw",
347   "position": {
348     "dx": -0.2953852399413136,
349     "dy": -0.260629777849676,
350     "dz": 0
351   },
352   "orientation": {
353     "elevation_angle": 90,
354     "heading_angle": 0
355   },
356   "radial_nodes": 35,
357   "diameter": 0.3000000567360903,
358   "hub_diameter": 0.030000005673609033,
359   "num_of_blades": 3,
360   "rotation_direction": "CCW",
361   "pitch": {
362     "type": "ratio",
363     "value": 0.5
364   },
365   "chord": {
366     "type": "elliptical",
367     "root": 0.04572
368   },
369   "m_hub": 0.0283,
370   "airfoils": {
371     "NACA2412": {
372       "properties": {
373         "type": "linear",
374         "alpha_L0": -0.036899751,
375         "CL_alpha": 6.283185307,
376         "Cm_L0": -0.0527,
377         "Cm_alpha": -0.08,
378         "CD0": 0.0055,
379         "CD0_L": -0.0045,
380         "CD0_L2": 0.01,
381         "CL_max": 1.4
382       }
383     }
384   }
385 }

```

```
386 }
387 }
```

G.2 Quadcopter

```
1 {
2   "plane": {
3     "name": "MyAirplane",
4     "CGx": 0,
5     "CGy": 0,
6     "CGz": 0
7   },
8   "reference": {
9     "area": 0.1680050228830184,
10    "longitudinal_length": 0.23125237233853135,
11    "lateral_length": 0.23125237233853135
12  },
13  "condition": {
14    "units": "SI"
15  },
16  "propellers": {
17    "prop_drivetrain_1": {
18      "name": "prop_cw",
19      "position": {
20        "dx": -0.2890654654231642,
21        "dy": 0.2890654654231642,
22        "dz": 0
23      },
24      "orientation": {
25        "elevation_angle": 90,
26        "heading_angle": 0
27      },
28      "radial_nodes": 100,
29      "diameter": 0.4625047446770627,
30      "hub_diameter": 0.04625047446770627,
31      "num_of_blades": 3,
32      "rotation_direction": "CW",
33      "pitch": {
34        "type": "ratio",
35        "value": 0.5
36      },
37      "chord": {
38        "type": "elliptical",
```

```

39     "root": 0.04572
40 },
41 "m_hub": 0.0283,
42 "airfoils": {
43     "NACA2412": {
44         "properties": {
45             "type": "linear",
46             "alpha_L0": -0.036899751,
47             "CL_alpha": 6.283185307,
48             "Cm_L0": -0.0527,
49             "Cm_alpha": -0.08,
50             "CD0": 0.0055,
51             "CD0_L": -0.0045,
52             "CD0_L2": 0.01,
53             "CL_max": 1.4
54         }
55     }
56 }
57 },
58 "prop_drivetrain_2": {
59     "name": "prop_ccw",
60     "position": {
61         "dx": 0.2890654654231642,
62         "dy": 0.2890654654231642,
63         "dz": 0
64     },
65     "orientation": {
66         "elevation_angle": 90,
67         "heading_angle": 0
68     },
69     "radial_nodes": 100,
70     "diameter": 0.4625047446770627,
71     "hub_diameter": 0.04625047446770627,
72     "num_of_blades": 3,
73     "rotation_direction": "CCW",
74     "pitch": {
75         "type": "ratio",
76         "value": 0.5
77     },
78     "chord": {
79         "type": "elliptical",
80         "root": 0.04572
81     },
82     "m_hub": 0.0283,

```

```

83     "airfoils": {
84         "NACA2412": {
85             "properties": {
86                 "type": "linear",
87                 "alpha_L0": -0.036899751,
88                 "CL_alpha": 6.283185307,
89                 "Cm_L0": -0.0527,
90                 "Cm_alpha": -0.08,
91                 "CD0": 0.0055,
92                 "CD0_L": -0.0045,
93                 "CD0_L2": 0.01,
94                 "CL_max": 1.4
95             }
96         }
97     },
98     "prop_drivetrain_3": {
99         "name": "prop_cw",
100        "position": {
101            "dx": 0.2890654654231642,
102            "dy": -0.2890654654231642,
103            "dz": 0
104        },
105        "orientation": {
106            "elevation_angle": 90,
107            "heading_angle": 0
108        },
109        "radial_nodes": 100,
110        "diameter": 0.4625047446770627,
111        "hub_diameter": 0.04625047446770627,
112        "num_of_blades": 3,
113        "rotation_direction": "CW",
114        "pitch": {
115            "type": "ratio",
116            "value": 0.5
117        },
118        "chord": {
119            "type": "elliptical",
120            "root": 0.04572
121        },
122        "m_hub": 0.0283,
123        "airfoils": {
124            "NACA2412": {
125                "properties": {

```

```

127         "type": "linear",
128         "alpha_L0": -0.036899751,
129         "CL_alpha": 6.283185307,
130         "Cm_L0": -0.0527,
131         "Cm_alpha": -0.08,
132         "CD0": 0.0055,
133         "CD0_L": -0.0045,
134         "CD0_L2": 0.01,
135         "CL_max": 1.4
136     }
137 }
138 }
139 },
140 "prop_drivetrain_4": {
141     "name": "prop_ccw",
142     "position": {
143         "dx": -0.2890654654231642,
144         "dy": -0.2890654654231642,
145         "dz": 0
146     },
147     "orientation": {
148         "elevation_angle": 90,
149         "heading_angle": 0
150     },
151     "radial_nodes": 100,
152     "diameter": 0.4625047446770627,
153     "hub_diameter": 0.04625047446770627,
154     "num_of_blades": 3,
155     "rotation_direction": "CCW",
156     "pitch": {
157         "type": "ratio",
158         "value": 0.5
159     },
160     "chord": {
161         "type": "elliptical",
162         "root": 0.04572
163     },
164     "m_hub": 0.0283,
165     "airfoils": {
166         "NACA2412": {
167             "properties": {
168                 "type": "linear",
169                 "alpha_L0": -0.036899751,
170                 "CL_alpha": 6.283185307,

```

```
171         "Cm_L0": -0.0527,  
172         "Cm_alpha": -0.08,  
173         "CD0": 0.0055,  
174         "CD0_L": -0.0045,  
175         "CD0_L2": 0.01,  
176         "CL_max": 1.4  
177     }  
178 }  
179 }  
180 }  
181 }  
182 }
```

Bibliography

- [AGS18] Pedro F. Albuquerque, Pedro V. Gamboa, and Miguel A. Silvestre. “Mission-Based Multidisciplinary Aircraft Design Optimization Methodology Tailored for Adaptive Technologies.” In: *Journal of aircraft* 55.2 (2018) (cit. on p. 108).
- [AKDS14] Gavin Kumar Ananda Krishnan, Robert W Deters, and Michael S Selig. “Propeller-Induced Flow Effects on Wings of Varying Aspect Ratio at Low Reynolds Numbers.” In: *32nd AIAA Applied Aerodynamics Conference*. 2014, p. 2152 (cit. on p. 55).
- [Apc] *APC Propeller Performance Data*. <https://www.apcprop.com/technical-information/performance-data/>, [Online; accessed 21-May-2019] (cit. on p. 60).
- [BHJ16] Dmitry Bershinsky, Steve Haviland, and Eric N Johnson. “Electric multirotor UAV propulsion system sizing for performance prediction and design optimization.” In: *57th AIAA/ASCE/AHS/ASC Structures, Structural Dynamics, and Materials Conference*. 2016, p. 0581 (cit. on p. 114).
- [Bia+16] Alessandro Bianchini et al. “An Experimental and Numerical Assessment of Airfoil Polars for Use in Darrieus Wind Turbines—Part II: Post-stall Data Extrapolation Methods.” In: *Journal of Engineering for Gas Turbines and Power* 138.3 (2016), p. 032603 (cit. on p. 100).
- [Bic+20] Marcin Biczyski et al. “Multirotor Sizing Methodology with Flight Time Estimation.” In: *Journal of Advanced Transportation* (2020) (cit. on p. 110).
- [BMH12] Murat Bronz, Jean-Marc Moschetta, and Gautier Hattenberger. “Multi-Point Optimisation of a Propulsion Set as Applied to a Multi-Tasking MAV.” In: *International Micro Aerial Vehicle Conference and Competition* (2012) (cit. on pp. 110, 111).
- [Bra74] A.R.S Bramwell. *Some Remarks on the Induced Velocity Field of a Lifting Rotor and on Glauert’s Formula*. Current Papers 1301. Aeronautical Research Council, 1974 (cit. on pp. 23, 46).
- [Bro+17] Murat Bronz et al. “Development of A Fixed-Wing mini UAV with Transitioning Flight Capability.” In: Toulouse, France: 35th AIAA Applied Aerodynamics Conference, AIAA AVIATION Forum, 2017 (cit. on p. 16).
- [DAS15] Robert W Deters, Gavin K Ananda, and Michael S Selig. “Slipstream measurements of small-scale propellers at low Reynolds numbers.” In: *33rd AIAA Applied Aerodynamics Conference*. 2015, p. 2265 (cit. on p. 55).
- [Die+15] Jeffrey M Diebold et al. “Experimental study of splitter plates for use with semispan wing models.” In: *53rd AIAA aerospace sciences meeting*. 2015, p. 1227 (cit. on p. 78).
- [DY65] John De Young. “Propeller at high incidence.” In: *Journal of Aircraft* 2.3 (1965), pp. 241–250 (cit. on pp. 22, 27–30, 46, 48).

- [EJ+94] Cramer EJ et al. “Problem formulation for multidisciplinary optimization.” In: *SIAM Journal on Optimization* 4 (1994) (cit. on p. 125).
- [Epe17] Kitso Epema. “Wing Optimisation for Tractor Propeller Configurations: Validation and Application of Low-Order Numerical Models Adapted to Include Propeller-Induced Velocities.” In: (2017) (cit. on pp. 55, 75).
- [Gat17] Mauro Gatti. “Complete preliminary design methodology for electric multirotor.” In: *Journal of Aerospace Engineering* 30.5 (2017), p. 04017046 (cit. on p. 114).
- [GD19] Rajan Gill and Raffaello D’Andrea. “Computationally Efficient Force and Moment Models for Propellers in UAV Forward Flight Applications.” In: *Drones* 3(4).77 (2019) (cit. on p. 23).
- [GJTA94] Garl L Gentry Jr, MA Takallu, and Zachary T Applin. “Aerodynamic characteristics of a propeller-powered high-lift semispan wing.” In: (1994) (cit. on p. 75).
- [Gla19] H Glauert. “The stability derivatives of an airscrew.” In: *British Aeronautical Research Council, Technical Report* 642 (1919) (cit. on p. 22).
- [GM52] Alfred Gessow and Garry C Myers. *Aerodynamics of the Helicopter*. Macmillan New York, 1952 (cit. on pp. 29, 34).
- [Goa18] Joshua Taylor Goates. “Development of an Improved Low-Order Model for Propeller-Wing Interactions.” In: (2018) (cit. on pp. 35, 97, 98, 102, 110).
- [Gou+17] Nicolas Gourdain et al. “Analysis of the turbulent wake generated by a micro air vehicle hovering near the ground with a lattice boltzmann method.” In: *Journal of the American Helicopter Society* 62.4 (2017), pp. 1–12 (cit. on p. 38).
- [Gra+19] Justin S. Gray et al. “OpenMDAO: An open-source framework for multidisciplinary design, analysis, and optimization.” In: *Structural and Multidisciplinary Optimization* 59.4 (2019), pp. 1075–1104 (cit. on pp. 111, 121).
- [Har08] Franklin D Harris. *Rotor performance at high advance ratio: theory versus test*. Tech. rep. NASA/CR—2008–215370. Moffett Field, CA, United States: National Aeronautics and Space Administration. Ames Research Center., 2008 (cit. on p. 37).
- [Har18] R. G Harris. “Forces on propeller due to sideslip.” In: *British Aeronautical Research Council, Technical Report* 427 (1918) (cit. on p. 22).
- [Hoe01] S.F. Hoerner. *Fluid-dynamic drag: practical information on aerodynamic drag and hydrodynamic resistance*. Hoerner Fluid Dynamics, 2001 (cit. on pp. 42, 100, 118).
- [Ita+11] Maxime Itasse et al. “Equilibrium transition study for a hybrid MAV.” In: *International Journal of Micro Air Vehicles* 3.4 (2011), pp. 229–245 (cit. on p. 54).
- [Jo+19] Yeongmin Jo et al. “Prediction of noise from low Reynolds number rotors with different number of blades using a non-linear vortex lattice method.” In: Delft, The Netherlands: 25th AIAA/CEAS Aeroacoustics Conference, 2019, p. 2615 (cit. on p. 38).
- [Joh12] Wayne Johnson. *Helicopter theory*. Courier Corporation, 2012 (cit. on pp. 23, 34, 36, 100).

- [Joh15] Wayne Johnson. *NASA Design and Analysis of Rotorcraft*. Tech. rep. NASA/TP—2015–218751. Moffett Field, CA, United States: National Aeronautics and Space Administration. Ames Research Center., 2015 (cit. on p. 37).
- [KD56] Richard E Kuhn and John W Draper. “Investigation of the aerodynamic characteristics of a model wing-propeller combination and of the wing and propeller separately at angles of attack up to 90 degrees.” In: *NACA-TR-1263* (1956) (cit. on p. 74).
- [LDM14] Leandro Ribero Lustosa, François Defaÿ, and Jean-Marc Moschetta. “Development of the flight model of a tilt-body MAV.” In: Toulouse, France: International Micro Air Vehicle Conference and Competition, 2014 (cit. on pp. 16, 54, 76).
- [Lei06] Gordon J Leishman. *Principles of helicopter aerodynamics with CD extra*. Cambridge university press, 2006 (cit. on pp. 22, 23, 34, 59, 100, 147).
- [Len+19a] Yuchen Leng et al. “Aerodynamic Modelling of Propeller Forces and Moments at High Angle of Incidence.” In: San Diego, United States: AIAA Applied Aerodynamics Conference, AIAA SciTech Forum, 2019 (cit. on pp. 22, 38).
- [Len+19b] Yuchen Leng et al. “Experimental Analysis of Propeller Forces and Moments at High Angle of Incidence.” In: *AIAA Scitech 2019 Forum*. 2019, p. 1331 (cit. on p. 28).
- [Len+20] Yuchen Leng et al. “Experimental Analysis of a Blown-Wing Configuration during Transition Flight.” In: *AIAA Scitech 2020 Forum*. 2020, p. 1983 (cit. on p. 110).
- [LM12] Andrew B. Lambe and Joaquim R. R. A. Martins. “Extensions to the Design Structure Matrix for the Description of Multidisciplinary Design, Analysis, and Optimization Processes.” In: *9th World Congress on Structural and Multidisciplinary Optimization* (2012) (cit. on pp. 121, 125).
- [McC94] B.W. McCormick. *Aerodynamics, Aeronautics, and Flight Mechanics*. Wiley, 1994 (cit. on pp. 54, 60, 68, 70).
- [Pap+18] Athanasios Papageorgiou et al. “Multidisciplinary Design Optimization of Aerial Vehicles: A Review of Recent Advancements.” In: *International Journal of Aerospace Engineering* 2018 (2018), p. 21 (cit. on pp. 108, 109).
- [PH88] David A Peters and Ninh HaQuang. “Dynamic inflow for practical applications.” In: *Journal of American Helicopter Society* 33 (1988), pp. 64–68 (cit. on pp. 22, 28).
- [Phi04] Warren F Phillips. *Mechanics of flight*. John Wiley & Sons, 2004 (cit. on pp. 24, 34–36, 42, 98, 101).
- [Pro] *RASA propeller catalogue*. <http://3fhobbyservice.jetshop.se/propellrar/rasa-c-247-1.aspx>. Accessed: 2020-10-30 (cit. on p. 114).
- [PSL18] Matthieu Parenteau, Kurt Sermeus, and Eric Laurendeau. “VLM Coupled with 2.5 D RANS Sectional Data for High-Lift Design.” In: *2018 AIAA Aerospace Sciences Meeting*. 2018, p. 1049 (cit. on p. 97).

- [PW91] M Pollack and F Warburton. “A simulation study of tiltrotor vertical takeoff procedures using conventional and variable diameter rotor systems.” In: (1991) (cit. on p. 80).
- [Qua] *Quantum System Tron F90+ Product Page*. <https://www.quantum-systems.com/project/tron-f90/>. Accessed: 2020-11-28. 2020 (cit. on pp. 127, 128).
- [Rib45a] Herbert S Ribner. *Formulas for propellers in yaw and charts of the side-force derivative*. Tech. rep. NACA-TR-819. Langley Field, VA, United States: National Advisory Committee for Aeronautic. Langley Aeronautical Lab., 1945 (cit. on pp. 22, 30, 31, 34).
- [Rib45b] Herbert S Ribner. *Propellers in yaw*. Tech. rep. NACA-TR-820. Langley Field, VA, United States: National Advisory Committee for Aeronautic. Langley Aeronautical Lab., 1945 (cit. on pp. 22, 30, 31, 35).
- [Rum42] LB Rumph. “Propeller forces due to yaw and their effect on airplane stability.” In: *Journal of the Aeronautical Sciences* 9.12 (1942), pp. 465–470 (cit. on p. 34).
- [RWS94] Bruce A. Reichert, Bruce J. Wendt, and United States. *A new algorithm for five-hole probe calibration, data reduction, and uncertainty analysis*. English. National Aeronautics and Space Administration ; National Technical Information Service, 1994, p. 1 v. (Cit. on p. 57).
- [SK81] R E Sheldahl and P C Klimas. “Aerodynamic characteristics of seven symmetrical airfoil sections through 180-degree angle of attack for use in aerodynamic analysis of vertical axis wind turbines.” In: (Mar. 1981) (cit. on p. 100).
- [The+14] Bart Theys et al. “Wind tunnel testing of a VTOL MAV propeller in tilted operating mode.” In: *2014 International Conference on Unmanned Aircraft Systems, ICUAS 2014 - Conference Proceedings*. May 2014, pp. 1064–1072 (cit. on pp. 41, 42).
- [The+17] Bart Theys et al. “Experimental and Numerical Study of Micro-Aerial-Vehicle Propeller Performance in Oblique Flow.” In: *Journal of Aircraft* 54.3 (2017), pp. 1076–1084 (cit. on pp. 23, 43–46).
- [Vel04] LLM Veldhuis. “Review of propeller-wing aerodynamic interference.” In: *24th International Congress of the Aeronautical Sciences*. Vol. 6. 1. 2004 (cit. on pp. 55, 75).
- [VM59] R. Von Mises. *Theory of Flight*. Dover Books on Aeronautical Engineering Series. Dover Publications, 1959 (cit. on pp. 26, 27).
- [Vto] *EVTOL Aircraft Directory*. <http://evtol.news/aircraft>, accessed: December, 3, 2019. Electric VTOL News by the Vertical Flight Society (cit. on p. 20).
- [WLS89] Dave P Witkowski, Alex KH Lee, and John P Sullivan. “Aerodynamic interaction between propellers and wings.” In: *Journal of Aircraft* 26.9 (1989), pp. 829–836 (cit. on pp. 55, 63).
- [Xfl] *XFLR5 Project Page*. <http://www.xflr5.tech/xflr5.htm>. Accessed: 2019-12-02 (cit. on p. 80).

- [YR60] Paul F Yaggy and Vernon L Rogallo. *A wind-tunnel investigation of three propellers through an angle-of-attack range from 0 deg to 85 deg*. Tech. rep. NACA-TN-D-318. Moffett Field, CA, United States: NASA Ames Research Center, 1960 (cit. on p. 42).

Résumé — Les progrès de la technologie de propulsion électrique dans les véhicules aériens à petite échelle ont introduit de nouvelles possibilités de l'utilisation accrue de vol en autonome. En permettant le décollage et l'atterrissage verticaux, les véhicules aériens sans pilote (UAV) pourraient voir plus d'applications dans les cahier de charge compliquées avec moins d'intervention humaine. Cependant, cela a introduit des conditions de vol inhabituelles pour les aéronefs à voilure fixe ou les aérogiro. Des attitudes de vol inhabituelles, des configurations d'aéronefs innovantes ainsi que des systèmes nouvellement ajoutés nécessitent un examen approfondi des hypothèses conventionnelles dans la conception des aéronefs et des nouvelles méthodologies lorsque ces hypothèses ne sont plus valables.

Cette étude doctorale s'est concentrée sur les problèmes aérodynamiques rencontrés par les drones convertibles généraux. Les performances de l'hélice à un angle d'incidence élevé ont été examinées et un modèle efficace en termes de temps de calcul a été proposé pour affiner l'analyse des performances dans des conditions extrêmes. L'interaction entre le sillage de l'hélice et la voilure a été étudiée pour comprendre son effet d'augmentation de portance. Un modèle numérique de lignes portantes s'est avéré capable d'estimer les performances de vol d'une combinaison hélice-voilure.

Les modèles développés ont été soigneusement vérifiés par trois campagnes d'essai en soufflerie. Des techniques tel que mesure de la charge et sondage du sillage ont été utilisées pour porter un jugement quantifiable sur la précision des modèles.

La dernière partie de l'étude actuelle était consacrée à faciliter la conception préliminaire des drones convertibles à longue endurance. Ces nouveaux outils d'analyse aérodynamique ont été assemblés dans un algorithme d'optimisation développé à partir de l'environnement OpenMDAO. Combinée à d'autres modèles d'ordre réduit, cette nouvelle méthodologie a pris en compte des cahiers de charge spécifiques pour dimensionner la configuration optimale d'un drone convertible souhaité. Des conceptions innovantes telles que l'avion hybride pourraient être modélisées et l'algorithme a permis une comparaison directe entre différentes configurations sur le même cahiers de charge.

Mots clés : Drone convertible, véhicule aérien sans pilote, hélice, interaction hélice-voilure, optimisation.

Abstract — The advance in electric propulsion technology in small-scale aerial vehicle has introduced new capability to expand autonomous flight. By enabling vertical take-off and landing, unmanned aerial vehicle (UAV) could see more applications in complicated flight mission with less human intervention. However this introduced unusual flight condition for either conventional fixed wing aircraft or rotorcrafts. Unusual flight attitudes, innovative aircraft configurations as well as newly added systems require a thorough review of conventional hypothesis in aircraft design and new methodologies where these hypothesis are no longer valid.

The doctoral study focused on aerodynamic problems confronted by general convertible UAV. Propeller performance at high incidence angle was reviewed and a computationally efficient model was proposed to refine performance analysis at off-design conditions. The interaction between propeller slipstream and lifting surface was studied to understand its lift augmentation effect. A revised numerical lifting line model was found to be capable to estimate flight performance of wing-propeller combination.

The developed models have been carefully verified through windtunnel experiments. Load measurement and flow survey techniques have been used to make quantifiable judgement on model accuracy.

Final part of the current study was dedicated to facilitate long endurance convertible UAV preliminary design. These new aerodynamic analysis tools were connected in an optimisation algorithm developed from OpenMDAO environment. Combined with other reduced-order models, this new methodology accounted for specific mission profiles to calculate optimal size for desired convertible UAV configuration. Innovative designs such as hybrid airplane could be modelled and the algorithm have permitted direct comparison between different configurations over a similar mission specifications.

Keywords: Convertible aircraft, unmanned aerial vehicle, propeller, propeller-wing interaction, optimisation.

Institut Supérieur de l'Aéronautique et de l'Espace, 10 Avenue Édouard-Belin
Toulouse